


5-2017

# Reduction in Recombination Current Density in Boron Doped Silicon Using Atomic Hydrogen

Matthew Garrett Young  
*University of Arkansas, Fayetteville*

Follow this and additional works at: <http://scholarworks.uark.edu/etd>

 Part of the [Electronic Devices and Semiconductor Manufacturing Commons](#), and the [Power and Energy Commons](#)

---

## Recommended Citation

Young, Matthew Garrett, "Reduction in Recombination Current Density in Boron Doped Silicon Using Atomic Hydrogen" (2017).  
*Theses and Dissertations*. 1995.  
<http://scholarworks.uark.edu/etd/1995>

This Dissertation is brought to you for free and open access by ScholarWorks@UARK. It has been accepted for inclusion in Theses and Dissertations by an authorized administrator of ScholarWorks@UARK. For more information, please contact [scholar@uark.edu](mailto:scholar@uark.edu), [ccmiddle@uark.edu](mailto:ccmiddle@uark.edu).

Reduction in Recombination Current Density in Boron Doped Silicon Using Atomic Hydrogen

A dissertation submitted in partial fulfillment  
of the requirements for the degree of  
Doctor of Philosophy in Engineering with a Concentration in Electrical Engineering

by

Matthew Garrett Young  
Arkansas Tech University  
Bachelor of Science in Electrical Engineering 2009  
University of Arkansas  
Master of Science in Microelectronics-Photonics 2012

May 2017  
University of Arkansas

This dissertation is approved for recommendation to the Graduate Council

---

Dr. Hameed A. Naseem  
Dissertation Director

---

Dr. William Oliver III  
Committee Member

---

Dr. Simon S. Ang  
Committee Member

---

Dr. Shui-Qing (Fisher) Yu  
Committee Member

---

Dr. Douglas Hutchings  
Committee Member

## **Abstract**

The solar industry has grown immensely in recent years and has reached a point where solar energy has now become inexpensive enough that it is starting to emerge as a mainstream electrical generation source. However, recent economic analysis has suggested that for solar to become a truly wide spread source of electricity, the costs still need to plummet by a factor of 8x. This demands new and innovative concepts to help lower such cost. In pursuit of this goal, this dissertation examines the use of atomic hydrogen to lessen the recombination current density in the boron doped region of n-type silicon solar cells. This required the development of a boron diffusion process that maintained the bulk lifetime of n-type silicon such that the recombination current density could be extracted by photoconductance spectroscopy. It is demonstrated that by hydrogenating boron diffusions, the majority carrier concentration can be controlled. By using symmetrically diffused test structures with quinhydrone-methanol surface passivation the recombination current density of a hydrogenated boron profile is shown to be less than that of a standard boron profile, by as much as 30%. This is then applied to a modified industrial silicon solar cell process to demonstrate an efficiency enhancement of 0.4%.

©2017 by Matthew Garrett Young  
All Rights Reserved

## **Acknowledgments**

While working to produce this dissertation, I came to the realization that the modern day Ph.D., in many ways, reflects the ability of the student to network with individuals to get work done. A large percentage of the problems studied now are complicated enough, that one persons' expertise is not enough to fully arrive at a solution. Because of this, there were an overwhelming number of people that offered to help me complete experiments, held discussions about theory, and just were great friends that let me vent on occasion. In an attempt to not spare space, I would like to acknowledge the efforts of the following individuals for helping get to where I am at today.

To my wife, Jessica, and son, Liam, I appreciate every single little thing you have done for me. Through thick and thin you absolutely drove me to stick with it. I know it was not easy on our family going through this whole process, but I am forever indebted to you for allowing me to pursue it. Jessica, I love you. I can honestly say I know what true love is because of you.

To my parents and my siblings, because whether or not I knew it then, I learned so, so much from all of you growing up. Some of these lessons just hit home now. I love you all.

To my in-laws, the Conry family. You all are absolutely the most generous and all around best in-laws. Thank you for everything you did while I was working on this Ph.D.

My dissertation director, Dr. Hameed Naseem, always pushed me to do better and better. I know there were times when I wasn't willing to accept such pressure, but I know it was only for my betterment. Thank you sir! In addition, I appreciate your willingness to let me follow my own passions in my research.

Dr. Fisher Yu opened my eyes to the world of semiconductor characterization and serves as a great example how how to run a research lab, thank you for these lessons. Dr. Oliver, thank you for agreeing to serve as my dissertation co-director. To my friends Kevin and Tosh Schoelz, your companionship, whether it be physics conversations, or delicious Indian food, was amazing. Thank you all so much. Kevin, I especially owe you for teaching me so many things.

Larry Cousar and Hafeez Mohammed, I thank you for your companionship and assistance with experiments. Larry, extra special thanks for introducing me to mountain biking. To Dou-

glas and Kassie Hutchings, all of the things you do and did to help keep Picasolar upright so as to provide an environment conducive to finishing this dissertation, your efforts were much appreciated. I thank Terry Tremwel for having the vision and belief that a younger generation can change the world for the better. Seth I thank you for being a good friend in rough times, and for introducing me to music that I would not have ever listened to.

To members of the HiDEC staff, especially Dr. Ang, Mike Steger and Errol Porter, I owe much to your efforts to maintain the cleanroom and provide technical expertise when equipment was down. A special thanks to Dr. Manasreh for allowing use of his lab, especially for the ECV characterization. In addition, I met many people at conferences such as PVSC, I thank Keith McIntosh and Malcolm Abbott for their efforts in creating PV Lighthouse. I would also like to give thanks to the staff at UCEP at GIT for assisting in creation of some samples so that this dissertation could happen. Also would like to thank Sergiu Pop of Yingli Green Energy Americas.

Very special thanks go out to the staff of the Electrical Engineering department at the University of Arkansas. Connie Howard, Tracey Long, Sharon Brasko and Daniel Klein rock! I would also like to thank the staff at the graduate school at the University of Arkansas. They worked with me up to the last minutes on my dissertation and were both patient and kind! Thank you all so much!

“It is not the critic who counts; not the man who points out how the strong man stumbles, or where the doer of deeds could have done them better. The credit belongs to the man who is actually in the arena, whose face is marred by dust and sweat and blood; who strives valiantly; who errs, who comes short again and again, because there is no effort without error and shortcoming; but who does actually strive to do the deeds; who knows great enthusiasms, the great devotions; who spends himself in a worthy cause; who at the best knows in the end the triumph of high achievement, and who at the worst, if he fails, at least fails while daring greatly, so that his place shall never be with those cold and timid souls who neither know victory nor defeat.” – Theodore Roosevelt 1910

# Contents

<b>1</b>	<b>Introduction</b>	<b>1</b>
1.1	Silicon Solar Cells - State of the Art . . . . .	1
1.2	Selective Emitter Technology . . . . .	5
1.3	The Hydrogen Selective Emitter . . . . .	8
1.4	Dissertation Overview . . . . .	10
<b>2</b>	<b>An Overview of Solar Cell Device Operation</b>	<b>11</b>
2.1	Introduction . . . . .	11
2.2	The Circuit Model of a Silicon Solar Cell . . . . .	11
2.3	Output of a Silicon Solar Cell . . . . .	13
2.4	Absorption of Light and Generation of Charge Carriers . . . . .	15
2.5	Recombination . . . . .	22
2.5.1	Radiative (Band-to-Band) Recombination . . . . .	24
2.5.2	Auger Recombination . . . . .	25
2.5.3	Shockley-Read-Hall Recombination . . . . .	26
2.5.4	Surface Recombination . . . . .	26
2.6	Recombination Current . . . . .	27
2.7	A Recombination Current Model of a Solar Cell . . . . .	30
2.8	Summary . . . . .	32
<b>3</b>	<b>Methods of Characterization and Data Analysis</b>	<b>33</b>
3.1	Photoconductance Lifetime Spectroscopy . . . . .	33
3.1.1	Extraction of Bulk Lifetime and Surface Recombination . . . . .	37
3.1.2	Measurement of Emitter Saturation Current Density . . . . .	41
3.1.3	Calibration of the WCT-120 . . . . .	47
3.2	The Four Point Probe Method . . . . .	48
3.3	Electrochemical Capacitance Voltage Profiling . . . . .	50
3.4	Spreading Resistance Profiling . . . . .	53
3.5	Light and Dark JV Characterization . . . . .	54
3.6	IQE/EQE . . . . .	56
3.7	Summary . . . . .	58
<b>4</b>	<b>Quinhydrone-Methanol Surface Passivation of Bulk n-type Silicon</b>	<b>59</b>
4.1	Quinhydrone-Methanol Passivation . . . . .	59
4.2	Bulk Lifetime Measurements and Surface Recombination Velocity . . . . .	60
4.2.1	Saw Damage Removal . . . . .	61
4.2.2	Containment . . . . .	64
4.2.3	Lifetime Data and Discussion . . . . .	66
4.2.4	Stability of Quinhydrone-Methanol Passivation . . . . .	69
4.3	Summary . . . . .	70
<b>5</b>	<b>Boron Diffusions from BN Solid Sources</b>	<b>72</b>
5.1	Background . . . . .	72
5.2	Boron Diffusion from a Boron Nitride Source Wafer . . . . .	74
5.3	Experimental Methods . . . . .	76
5.4	Two Methods of Removing the BRL . . . . .	79
5.5	Measurement of Boron Diffusions and Extraction of $J_{0e}$ . . . . .	83

5.6	Summary . . . . .	92
<b>6</b>	<b>Hydrogenation of Boron and Reduction in Recombination Current</b>	<b>94</b>
6.1	Experimental Methods . . . . .	94
6.2	Experiment to Control Sheet Resistance . . . . .	97
6.3	Initial $J_{0e}$ Measurements . . . . .	99
6.4	Hydrogenation Results on Symmetrical Diffusions . . . . .	105
6.5	Summary . . . . .	114
<b>7</b>	<b>Device Concept and Fabrication</b>	<b>115</b>
7.1	Fabrication Overview of Silicon Solar Cells . . . . .	115
7.2	Analysis of Hydrogen Selective Emitter On Industrial-Like Solar Cells . . . . .	116
	7.2.1 JV Analysis . . . . .	119
	7.2.2 EQE . . . . .	120
7.3	Summary . . . . .	122
<b>8</b>	<b>Conclusions and Future Work</b>	<b>123</b>
	<b>Bibliography</b>	<b>125</b>



## List of Figures

1.1	Cross-sectional description of an Al-BSF cell. The back Al contact is fired and partially diffused to create the back p+ region of the cell. . . . .	2
1.2	Actual market share of n-type cells versus predicted market share. . . . .	4
1.3	One type of a modern n-type cell architecture with regions of the device labeled. Note that the BSF is a phosphorous diffused region, and is not created with alloying like the AL-BSF. ARC = Antireflection Coating . . . . .	4
1.4	Data from [1] that shows examples of a high efficiency and industrial emitter profiles. . . . .	6
1.5	Process flows for solar cell manufacturing which incorporates an industrially relevant SE technology. Extra steps are highlighted in red and extra controls are highlighted in blue. . . . .	7
1.6	Illustration of HSE method on a n-type solar cell. . . . .	9
2.1	The common single diode model for describing solar cell operation. . . . .	11
2.2	JV curve for a solar cell modeled by the circuit model of Figure 2.1 with $J_{ph} = 38 \text{ mA/cm}^2$ , $J_0 = 1 \times 10^{-13} \text{ A/cm}^2$ , $R_{sh} = 10,000 \Omega - \text{cm}^2$ , and $R_{ser} = 1 \Omega - \text{cm}^2$ . . . . .	14
2.3	Solar spectrum radiation for wavelengths of interest to silicon solar cells. The vertical black line denotes the bandgap of Si. The total amount of current density that any silicon solar cell can obtain is no greater than $46 \text{ mA/cm}^2$ . . . . .	16
2.4	Diagram indicating possible transmission, reflection or absorption pathways in silicon. . . . .	17
2.5	Absorption coefficient (blue) and absorption depth (red) of silicon. . . . .	18
2.6	Diagram indicating the effect of texture and a back reflector on the optical management of a solar cell. . . . .	19
2.7	Schematic of the excitation of an electron in the valence band due to an absorption event. The red arrow indicates thermalization of the electron to the conduction band edge. . . . .	19

2.8	Relevant time scales involved with absorption, thermalization, and recombination processes in silicon against excess carrier density. Box plots indicate different time scales. . . . .	20
2.9	Diagram showing the different possible recombination mechanisms in silicon. . .	23
2.10	Plot of the effective lifetime of a 180 $\mu m$ thick n-type wafer with $N_D = 1 \times 10^{-16} cm^{-3}$ . . . . .	28
2.11	Plot of the lifetime of a 180 $\mu m$ thick wafer with $N_D = 1 \times 10^{-16} cm^{-3}$ . . . . .	29
2.12	Cross sectional model for a n-type solar cell with various regions labeled by recombination current density. . . . .	31
3.1	Photograph showing the Sinton Instruments WCT-120 Photoconductance Lifetime measurement tool. . . . .	34
3.2	Graphic depicting the bulk of a silicon wafer and its two surfaces from which the effective lifetime can be found. . . . .	38
3.3	Plot of diffusion length against lifetime from equation 3.12, assuming a fixed value of $D = 12 cm^2/sec$ for minority holes in n-type silicon. . . . .	39
3.4	Lifetime versus minority carrier density for a n-type Si wafer showing how the bulk lifetime (effective) without surface recombination is made up of each recombination component. . . . .	41
3.5	Graphic showing the test structure used to extract $J_{0e}$ measurements. The arrow denotes the boundaries for the mathematical analysis of the structure. . . .	42
3.6	Inverse lifetime plot showing the linear output from a diffused sample as measured by the WCT-120. The slope is used to calculate the $J_{0e}$ . . . . .	46
3.7	Image showing the current and voltage probes used in for a four point probe measurement . . . . .	48
3.8	Circuit schematic explaining why a four point method is preferred over a two point probe method . . . . .	49
3.9	Image showing a sealing ring containing electrolyte in contact with a diffused layer on top of a wafer bulk. The system can be modeled with a standard circuit. .	51

3.10	A conceptual band structure diagram showing how the positive ions in the electrolyte, deplete the semiconductor. The capacitance of this depletion area of width $W_d$ is measured for doping extraction. . . . .	52
3.11	Graphical illustration of Pulsed Anodization concept. The blue horizontal arrows represent phase for silicon oxide growth. The red horizontal arrows represent a phase where the grown oxide is etched away. . . . .	53
3.12	(Left) Diagram showing how a sample is beveled and two probes are placed on the bevel for measurement. The dashed lines represents the path taken by the probes to measure the spreading resistance. (Right) A diagram illustrating the resistances present in one probe. . . . .	54
3.13	Block diagram overview of a JV measurement system complete with solar simulator, chiller, vacuum pump, and SMU for sourcing and measuring current and voltage. . . . .	55
3.14	Block diagram showing relevant components of a commercial IQE/EQE system. . . . .	57
4.1	Illustration of bulk silicon with saw damage acting as a high SRV layer on either side fo the wafer. . . . .	61
4.2	Thickness of a silicon wafer sample versus time showing linear etch rate of 10:1:2 HNA solution. . . . .	63
4.3	Lifetime measured on same sample with no processing, after a Piranha clean process, and finally after etch in 90°C 25% TMAH. . . . .	64
4.4	Comparison of transient photoconductance output between two samples having been passivated in QM but with two different containment methods. . . . .	65
4.5	Comparison of transient photoconductance output between FZ and Cz silicon passivated with QM. . . . .	68
4.6	Stability of QM passivation over a short time period. . . . .	70
5.1	Image showing how boron nitride source wafers (white) are loaded into a quartz boat with silicon wafers. . . . .	75

5.2	This image shows how Nitrogen gas forms a column of nitrogen around the sources and wafers. This allows for the diffusion of the B <sub>2</sub> O <sub>3</sub> from the source to the wafer surface. . . . .	76
5.3	Thermal profile of diffusion recipes showing temperature variation with time. . .	78
5.4	(a) Thermal profile of LTO recipe with (b) measured $\Delta R_{sh}$ versus oxidation time. . . . .	80
5.5	Parallel resistor model that explains measured $R_{sh}$ values using FPP with a BRL in place. . . . .	81
5.6	Percent $R_{sh}$ change plot against etch time for chemical removal of the BRL. . .	82
5.7	Boron diffusion profile as measured by ECV along with an ERFC fit to the data.	84
5.8	EDNA 2 calculations showing $J_{0e}$ plotted against effective SRV for the profile shown in Figure 5.7. . . . .	86
5.9	Measured $J_{0e}$ for B diffusions in G35XY FZ material. . . . .	88
5.10	Measured $J_{0e}$ for B diffusions in P0A9 material from an outside lab. . . . .	89
5.11	Comparison between boron diffusion profile created locally versus one that is from an industrial process. . . . .	90
5.12	EDNA 2 calculation of boron diffusion profiles shown in Figure 5.11. Colors are coordinated between the plots. . . . .	91
6.1	Series of images showing the hydrogenation apparatus used in this work to expose boron diffused samples to hydrogenation. . . . .	96
6.2	From left to right: The step involved in creating a symmetrical diffusion having undergone double sided hydrogenation. . . . .	97
6.3	Response surface showing relationship between temperature and pressure against sheet resistance percentage change. . . . .	99
6.4	Degradation of $J_{0e}$ with increase hydrogenation time. . . . .	100
6.5	SIMS analysis of two samples, a control, and a hydrogenated sample. . . . .	101
6.6	Enlarged view SIMS analysis of two samples, a control, and a hydrogenated sample. . . . .	102

6.7	SIMS analysis of two samples, a control, and a hydrogenated sample. . . . .	103
6.8	SIMS analysis of two samples, a control, and a hydrogenated sample. . . . .	104
6.9	Impact of hydrogenation process on industrial boron diffusions. . . . .	105
6.10	EDNA2 simulations of diffusions shown in Figure 6.9. . . . .	106
6.11	Measured $J_{0e}$ of 14 control samples and hydrogenated samples on FZ silicon (G35XY). Averages for each sample population are shown by horizontal dashed bars. . . . .	108
6.12	Measured $R_{sh}$ of 14 control samples and hydrogenated samples on FZ silicon (G35XY). Averages for the control sample population are shown by horizontal dashed bars. . . . .	109
6.13	Measured $J_{0e}$ of 14 control samples and hydrogenated samples. Averages for each sample population are shown by horizontal dashed bars. . . . .	110
6.14	Measured $R_{sh}$ of 14 control samples and hydrogenated samples. Averages for the control sample population are shown by horizontal dashed bars. . . . .	111
6.15	Measured $R_{sh}$ of 16 control samples and hydrogenated samples. Averages for each sample population are shown by horizontal dashed bars. . . . .	112
6.16	Emitter etchback study on a hydrogenated emitter versus a non-hydrogenated emitter. . . . .	113
7.1	Image that shows steps in creating HSE enhanced cells with modified silicon solar cell fabrication process. . . . .	116
7.2	(Left) Histogram analysis for $N = 24$ total cells that had undergone the cell fabrication process of Figure 7.1. (Right) Population, $N = 5$ , of control cells. . .	118
7.3	Light JV curves collected on full size cells with just thermal oxide passivation (OoB), right after the hydrogenation process (Post H), and following SiNx de- position and dielectric charging (Post Charge). . . . .	119
7.4	The highest efficiency hydrogenated cell versus the highest efficiency control cell. Though not visible because of the scale of the graph, the $V_{oc}$ of the H cell is 2 mV greater than that of the Non-H cell. . . . .	120

7.5 EQE plots of small oxide cells that were passivated with thermal oxide, put through the hydrogenation process, and then charged with negative charges. The red highlighting indicates the increase in short wavelength response obtained from the selective emitter structure. . . . . 121

## List of Tables

5.1	Nominal characteristics of wafer material used to study boron diffusions. . . . .	77
5.2	Standard cleaning process that most samples go through before a diffusion process . . . . .	77
6.1	Factors Used in Experimental Design for Sheet Resistance Testing . . . . .	98
7.1	Tabulation of 24 experiments conducted for 4 factor experimental design to test hydrogenation of industrial like silicon solar cells. . . . .	117
7.2	Tabular summary of maximum, median, and minimum values obtained from histogram analysis of data in Table 7.1. . . . .	117

# Chapter 1

## Introduction

This dissertation shows that atomic hydrogen can be used to lower the recombination current density of boron doped silicon which can boost the efficiency of an n-type silicon solar cell.

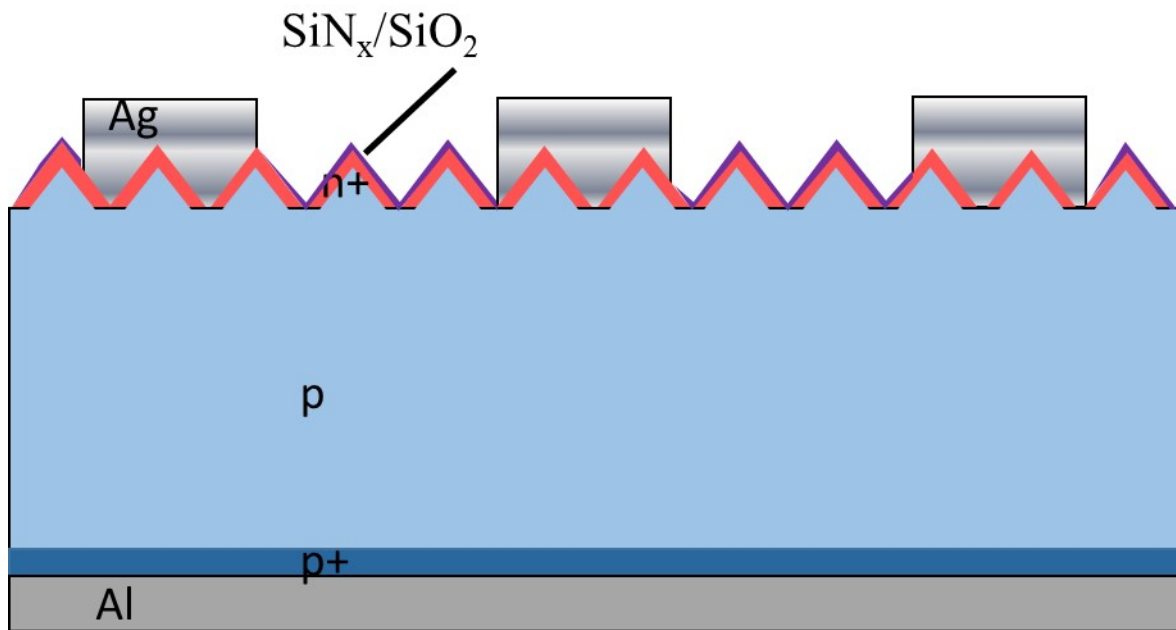
### 1.1 Silicon Solar Cells - State of the Art

Silicon solar cells are the most predominant type of solar technology and represent over 90 percent market share in industry. This dominance is due to the silicon material itself because of its studied nature brought on by the integrated circuit industry. The ultimate goal of the application of solar research is to devise materials and methods that allow for a reduction of the  $\$/W$  metric, and to greater extent the levelized cost of electricity (LCOE). The cost per watt ( $\$/W$ ) metric refers to the amount of capital monetary investment needed to generate a watt of a power. As of writing this dissertation, there are now industrial silicon solar cells of 19% efficiency being produced at a  $\$/W$  of less than \$0.50 [2]. There are two known laboratory methods to minimize the  $\$/W$ , either introduce materials or methods that are less expensive than current ones (reducing  $\$$ ) or increase the efficiency of the device (increase  $W$ ). The bulk of the work in this dissertation focuses on the latter point.

Most modern types of silicon solar cells available on the market are known as p-type aluminum back surface field (Al-BSF) solar cells. The name comes from the fact that the bulk of the cell is fabricated from p-type silicon (doped with boron most typically). The backside of the cell is alloyed with Al to create both a back contact and a BSF structure in one processing step. A cross sectional description of such a cell is given in Figure 1.1.

Al-BSF cell architectures cannot achieve efficiencies higher than 20% due to three technology limitations. These limitations include recombination at the back surface which lowers cell output voltage, a lack of diffuse reflectance at the back surface [3] which reduces longer wavelength light collection and therefore reduces current output, and p-type bulk material is known to suffer from a phenomenon known as light induced degradation (LID). LID is linked to a reaction between oxygen and boron in the silicon lattice [4] and increases recombination





## Al-BSF Cell

Figure 1.1: Cross-sectional description of an Al-BSF cell. The back Al contact is fired and partially diffused to create the back p+ region of the cell.

in the device over time, which reduces cell output efficiency. To overcome the former limitations, processes to redesign the backside have been generated. Such processes have produced structures known as passivated emitter rear contact (PERC) cells [5]. Such cells overcome the limitations of the Al-BSF cell by minimizing contact points at the backside and by applying passivation. The move to PERC architectures does not come without added cost to the manufacturing process.

Regarding LID, more modern approaches have been focusing on eliminating this property, but none are known to be implemented in industry [6]. In fact, such approaches might cause contact issues, which further compromise the solar cell. To combat the inadequacies of p-type material, individuals have sought to create n-type solar cells. N-type silicon is known to better withstand metallic impurities that might otherwise cause electronic loss [7]. In addition, n-type cells are not known to suffer from LID. It has been speculated for sometime now that n-type cells will become the dominant silicon solar cell technology [2]. The actual percent market share of n-type silicon compared with historical forecasts of the market share of n-type silicon is given in Figure 1.2. The two curves, Prediction 1 and Prediction 2, show how analysts over projected the market share of solar cell architectures [8, 9]. The blue curve shows the actual market share of solar cell architectures based on n-type silicon [2]. The reason for this over estimation of how quickly n-type solar cells would saturate the market has to do with technological limitations of the bulk n-type silicon.

All of the benefits of n-type silicon over p-type silicon more than make the case why it should be the dominant technology. In fact, the highest efficiency silicon solar cells to date have been made from n-type silicon [10][11]. N-type technology does not come without its obstacles which has slowed its dominance. For one, a n-type cell cannot support an Al-BSF structure on the backside as shown in Figure 1.3. This means extra processing steps, by way of a phosphorous diffusion, are necessary to create a BSF in a n-type cell, which adds to cost.

Another barrier to entry for n-type, is that the boron diffusion is required to form the front side emitter region. Boron (B) moves more slowly through the silicon lattice compared to Phosphorous (P), which means that B diffusion processes are slower. Slower diffusion process-

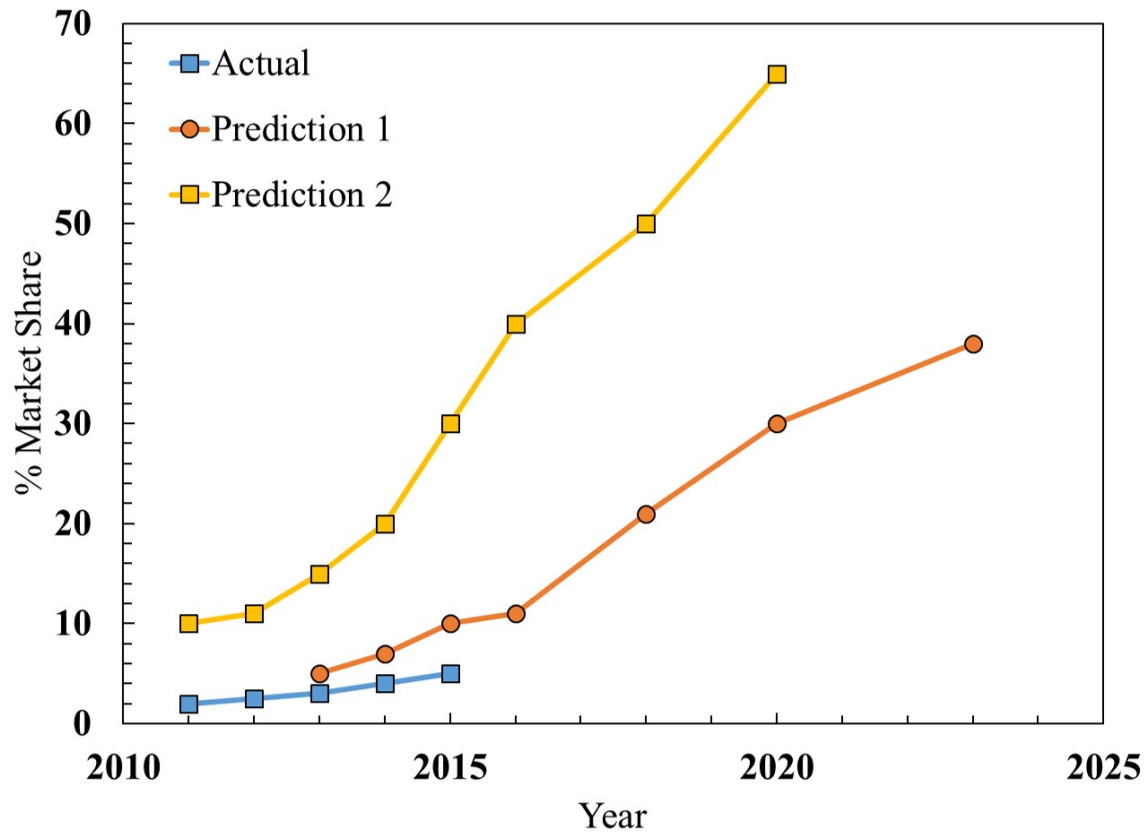


Figure 1.2: Actual market share of n-type cells versus predicted market share.

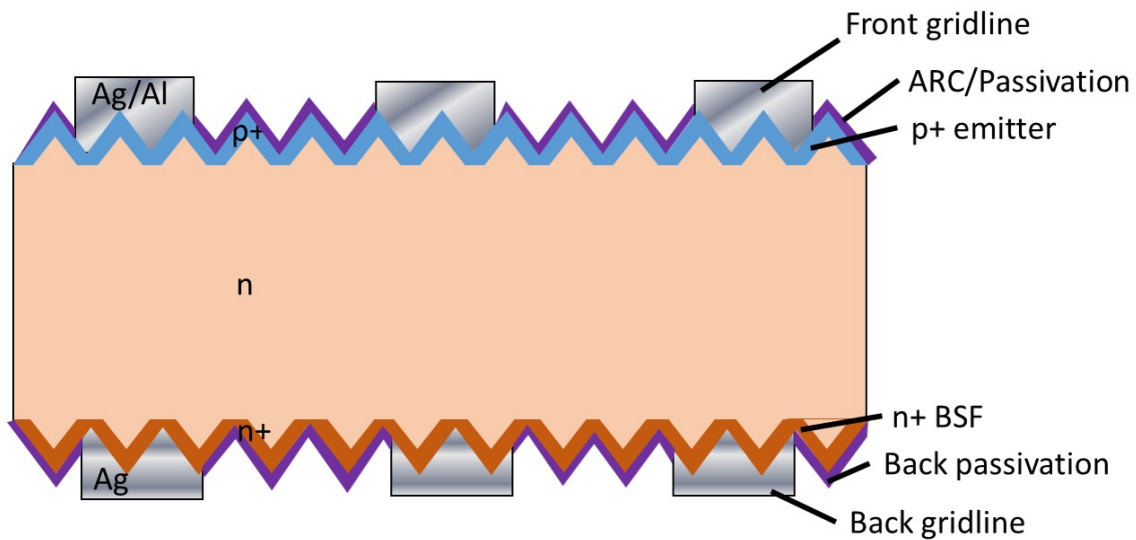


Figure 1.3: One type of a modern n-type cell architecture with regions of the device labeled. Note that the BSF is a phosphorous diffused region, and is not created with alloying like the AL-BSF. ARC = Antireflection Coating

ing lowers cell manufacturing throughput, which increases cell manufacturing cost.

This dissertation examines how atomic hydrogen can be used to reduce recombination in the boron doped p+ emitter region of a n-type silicon solar cell. By reducing recombination in this region, the cell efficiency increases. A gain in cell efficiency can make up for or at least displace slower manufacturing throughput (as is the case for the B diffusion of n-type solar cells).

The work in this dissertation provides the scientific backing behind the implementation of the Hydrogen Selective Emitter (HSE) technology for n-type silicon solar cells. HSE has been being commercialized by Picasolar, Inc. since 2013. Picasolar has received multiple Department of Energy Sunshot Incubator awards to commercialize the HSE technology. In addition, many solar industry players are interested in such a technology. Therefore, the work in this dissertation is of practical value for the solar industry in the near future.

As of writing this dissertation, work on the HSE technology is not complete. However, the work in this dissertation provides the experimental foundation that shows the technical viability of the HSE technology.

## **1.2 Selective Emitter Technology**

The focus of this dissertation is on the front p+ emitter region of a n-type solar cell. This is because for modern n-type solar cells with high bulk lifetimes and well passivated surfaces, the front emitter and back BSF place limits on the maximum cell efficiency [12].

Typical p+ emitter regions in n-type silicon solar cells are known as homogeneous emitters. This is because the same emitter is found all across the front surface of the cell. This is the standard practice in common industrial cells as it is the least expensive option. This emitter region must be designed to satisfy efficient collection of carriers by light absorption, low-loss lateral transport of carriers to the gridlines, and a maximum output voltage by optimum doping concentration [13]. For a homogeneous emitter this is all accomplished through careful optimization of the diffusion process that forms the emitter. The emitter profile as a result of the diffusion process looks like those in Figure 1.4 which comes from Benick et. al. [1]. The

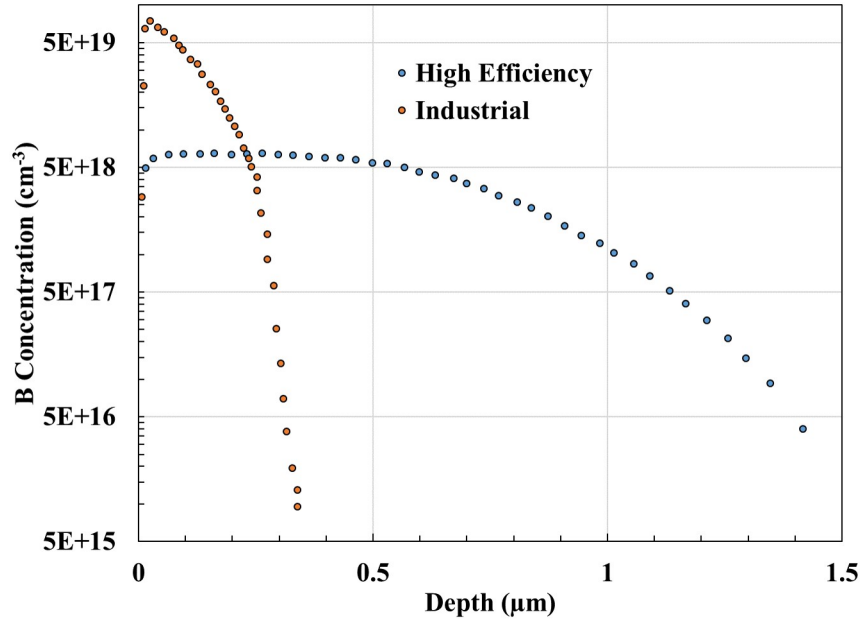


Figure 1.4: Data from [1] that shows examples of a high efficiency and industrial emitter profiles.

emitter profiles (the two plots in Figure 1.4) are created by measuring how the boron doping concentration in the silicon varies with depth. Each data point represents the measured boron concentration at a given depth into the silicon (the n region of Figure 1.3). The industrial emitter profile is typical of how the boron concentration would vary with depth for the cell architecture shown in Figure 1.3 (the region denoted by p+). The high efficiency emitter has a boron concentration that extends further into the n-type silicon with a lower surface concentration, whereas the industrial emitter is more shallow with a higher boron surface concentration. The solar cell efficiency can vary quite dramatically depending on the how the concentration of the boron varies with depth near the surface. In fact, Benick et. al. fabricated two different cells each of which uses one of the profiles in Figure 1.4. For the high efficiency profile, the efficiency of the best cell was 23.4% whereas for the industrial profile the best efficiency was 21.8% [1].

Benick et. al.'s work illustrates the sensitivity of the cell output to a change in the emitter profile. However, the high efficiency profile is more resistive, and requires more gridlines on the front of the cell. In addition, it requires multiple high temperature manufacturing steps

### Industrial Selective Emitter Processes

Etch-Back SE	Doping Paste SE	Laser Doped SE
<ul style="list-style-type: none"> <li>• Alkaline Texture</li> <li>• POCl<sub>3</sub> Emitter Diffusion</li> <li>• Inkjet Masking</li> <li>• Edge Isolation</li> <li>• Emitter Etch-Back</li> <li>• Etch Depth Feed Back</li> <li>• Mask Stripping</li> <li>• PSG-Removal</li> <li>• PECVD SiNx:H ARC</li> <li>• Grid Alignment</li> <li>• Screen Print/Fire</li> </ul>	<ul style="list-style-type: none"> <li>• Alkaline Texture</li> <li>• Print Doping Paste</li> <li>• Bake Paste</li> <li>• POCl<sub>3</sub> Emitter Diffusion</li> <li>• Edge Isolation</li> <li>• PSG-Removal</li> <li>• PECVD SiNx:H ARC</li> <li>• Grid Alignment</li> <li>• Screen Print/Fire</li> </ul>	<ul style="list-style-type: none"> <li>• Alkaline Texture</li> <li>• SiO<sub>2</sub> Deposition or Growth</li> <li>• Laser Abalation of SiO<sub>2</sub></li> <li>• POCl<sub>3</sub> Emitter Diffusion</li> <li>• Etch Laser Damage</li> <li>• Edge Isolation</li> <li>• PSG-Removal</li> <li>• PECVD SiNx:H ARC</li> <li>• Grid Alignment</li> <li>• Screen Print/Fire</li> </ul>

Figure 1.5: Process flows for solar cell manufacturing which incorporates an industrially relevant SE technology. Extra steps are highlighted in red and extra controls are highlighted in blue.

to create, which in turn, all act to increase manufacturing cost. This reduces manufacturing viability in an industrial setting.

A way to have the “best of both worlds” (in regards to the profiles of Figure 1.4) would be to somehow incorporate both profiles into the solar cell design. The less resistive profile is more ideal for making contact to the gridlines and the profile with lesser doping concentration is more useful in areas between metal contacts. Methods of optimizing the profile under the metal contact and those not under the metal are known as selective emitter (SE) methods. That is, the doping concentration is selectively controlled in the emitter region. As outlined by Rahman, SE methods should 1.) require a minimum of additional processing steps, 2.) possibility of integration into a manufacturing line, 3.) no yield loss, 4.) a boost in cell efficiency by at least 0.2% absolute [13].

Such SE methods that have been developed that have been shown to have manufacturing viability include the etch-back SE [13], the laser doped SE [14], and SE based upon doping pastes [15]. Figure 1.5 summarizes three of the main SE methods used in industry, with the additional manufacturing steps highlighted [16].

One disadvantage of many of these SE technologies is the required number of extra processing steps or control steps. In particular, all of these methods require extra controls to align the screen printed metal grid to the top of the cell. These extra control and alignment proce-

dures are a necessary element to most SE processes because in a SE there are regions where the emitter doping profile are optimized for metal contact. Since gridlines are applied as one of the last steps in the cell manufacturing process it is necessary then to align the gridlines to the patterned regions of higher doping in order to form the SE. The extra controls and processing steps lead to extra costs, which has inhibited the adoption of SE technology in industry.

### 1.3 The Hydrogen Selective Emitter

A way of overcoming the detrimental features of the common industrial SE methods given in Figure 1.5 is with a method known as the Hydrogen Selective Emitter (HSE). The key idea behind this method is shown in Figure 1.6. The cell architecture from Figure 1.5 is shown in Figure 1.6. Pictured is the process of exposing the front surface of the cell to atomic hydrogen. The atomic hydrogen is blocked by the metal gridlines on top of the solar cell whereas in regions not covered by a metal gridline the atomic hydrogen enters into the boron doped emitter profile.

Atomic hydrogen is used to inactivate boron dopants in the silicon lattice [17]. As a result, the electrical activity of the boron atom is quenched, which effectively lessens the boron concentration of the profile. Because the process occurs after a solar cell is fully fabricated the gridlines at the front of the cell mask the atomic hydrogen and prevent deactivation. If the cell is manufactured with an emitter profile having heavier concentration than the industry standard, atomic hydrogen can be used to inactivate the boron in the heavier doped profile, making it more ideal as an emitter not contacted by metal.

There are two obstacles to implementation of the HSE process. The first obstacle is the diffusion of atomic hydrogen through the silicon nitride anti-reflection coating and oxide passivation layer that is on the front of industrial solar cells. The second, and separate obstacle, is showing that the inactivation of atomic hydrogen actually improves the electronic quality of the emitter layer. The focus of this dissertation is on the second obstacle wherein the methods here show that the recombination current density of the p+ emitter region can be reduced,

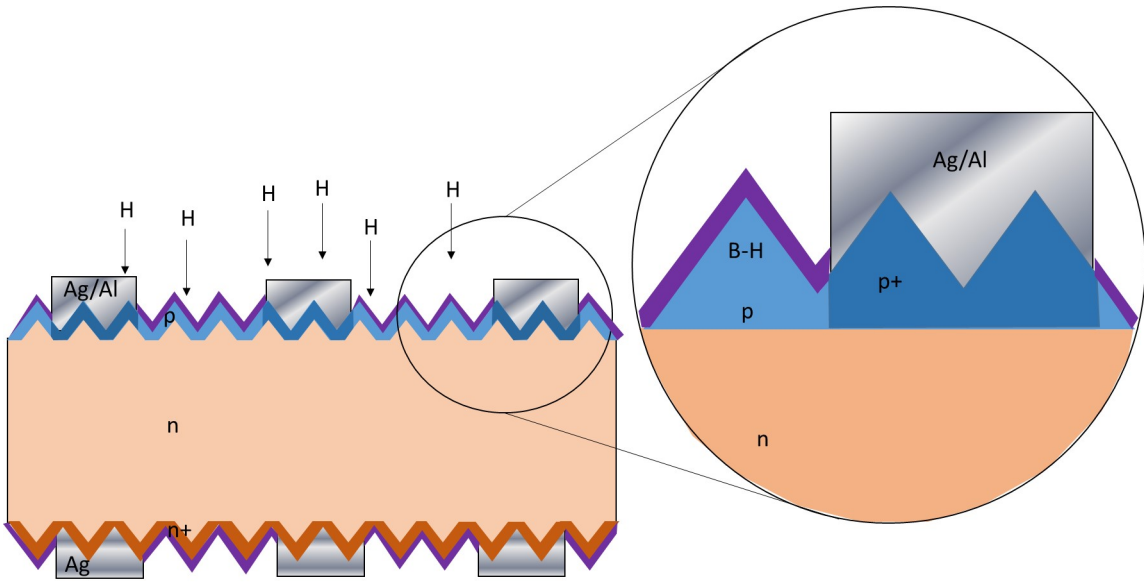


Figure 1.6: Illustration of HSE method on a n-type solar cell.

which results in an overall efficiency gain for the cell.



## 1.4 Dissertation Overview

This dissertation describes a series of studies that lead up to understanding how atomic hydrogen can improve the front surface of n-type silicon solar cells. Chapter 2 of this dissertation discusses an overview of silicon solar cell theory, with emphasis on generation and recombination processes. It defines the recombination current density of a boron emitter,  $J_{0e}$ . Chapter 3 gives a high level overview of the characterization techniques that were used. It describes how the recombination current density of the emitter region is measured using photoconductance spectroscopy. Such a method, standard in the PV industry, was a core technique to show that atomic hydrogen can minimize a fundamental device parameter. Chapter 4 describes the establishment of a method to measure the bulk lifetime of silicon samples using a liquid passivation solution, quinhydrone-methanol (QM) and compares the measured lifetime values to the literature to vet the process on bulk silicon. Because the boron diffusion process creates the emitter doping profile of a solar cell, Chapter 5 gives an overview of the work that was necessary to develop a boron diffusion process. Boron nitride solid sources had to be utilized due to infrastructure constraints and two different methods of boron rich layer removal are compared. QM is then applied as surface passivation to the boron diffusions to measure  $J_{0e}$ . Chapter 6 details the experiments used to show atomic hydrogen lowers the value of the fundamental device parameter,  $J_{0e}$ . The methods discussed in chapters 4-6 are applied to devices and device measurements are analyzed in Chapter 7. Finally, Chapter 8 concludes the dissertation, and provides future avenues of research work.

## Chapter 2

### An Overview of Solar Cell Device Operation

#### 2.1 Introduction

The purpose of a solar cell is to take radiative energy from the sun (or another light source) and convert it into an electrical current. Various material systems are used to create solar cells, however the most predominant are solar cells made from crystalline silicon. The basic operation of almost all solar cells is the same. When exposed to light, atomic processes internal to the silicon generate charge carriers, which immediately begin to recombine. The key to engineering the best solar cell is to design a cell such that the charge carriers are forced outside the device, to produce current, before they recombine. The ultimate goal of solar cell design is to maximize internal generation processes and minimize recombination processes.

#### 2.2 The Circuit Model of a Silicon Solar Cell

The operation of a silicon solar cell can be understood by examining the well known single diode circuit model of the solar cell. A circuit schematic for such a model is shown in Figure 2.1. The model features four circuit components including the light generated current density  $J_{ph}$  modeled as an ideal current source, the diode representing the p+/n junction of the solar cell, a resistor,  $R_{sh}$  that models loss to shunt resistances, and the losses series resistance,  $R_{ser}$ .

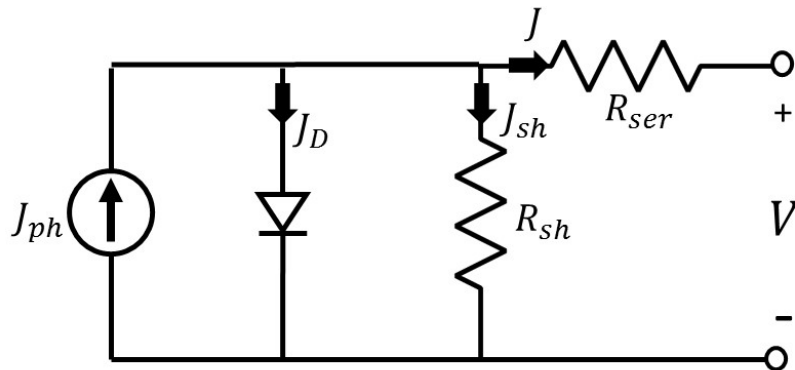


Figure 2.1: The common single diode model for describing solar cell operation.

Kirchoff's current law can be used to sum the current densities so that,

$$J = J_{ph} - J_D - J_{sh} \quad (2.1)$$

with  $J_D$  being the current density lost due to recombination in the diode, and  $J_{sh}$  being the current density representing losses to the shunt resistances in the cell, and the current density  $J$  being the output current of the cell. The current density,  $J_D$ , is specified by,

$$J_D = J_0(e^{((V+JR_{ser})/kT)} - 1) \quad (2.2)$$

where  $J_0$  represents the saturation current density,  $V$  represents the output voltage of the cell,  $JR_{ser}$  is the voltage drop across the resistor,  $R_{ser}$ ,  $k$  is Boltzmann's constant, and  $T$  is temperature of the cell in Kelvin.  $J_0$  is also known as the recombination current density, as it arises in a solar cell due to internal recombination processes. The total voltage term in the exponential is given by  $V + JR_{ser}$  as this is the voltage drop found across the diode given in Figure 2.1. It is also easy to see from the circuit diagram of Figure 2.1 that  $J_{sh}$  can be found utilizing Ohm's law so that,

$$J_{sh} = (V + JR_{ser})/R_{sh} \quad (2.3)$$

By combining the terms  $J_{ph}$ ,  $J_D$ , and  $J_{sh}$  the total output current,  $J$  can be defined as,

$$J = J_{ph} - J_0(e^{((V+JR_{ser})/kT)} - 1) - (V + JR_{ser})/R_{sh} \quad (2.4)$$

where the solar cell J-V behavior can be defined by the four model parameters  $J_{ph}$ ,  $J_0$ ,  $R_{ser}$ , and  $R_{sh}$ . When the model parameters specified are defined, equation 2.4 allows for the characteristic J-V output of a solar cell to be calculated and plotted. Figure 2.2 shows the plot of equation 2.4 with  $J$  plotted against  $V$  for arbitrarily defined model parameters where  $J_{ph}$  is 38 mA/cm<sup>2</sup>,  $J_0$  is  $1 \times 10^{-13}$  A/cm<sup>2</sup>,  $R_{sh}$  is 10,000  $\Omega - cm^2$ , and  $R_{ser}$  is 1  $\Omega - cm^2$ . The purpose here is not to fit data, but rather, just introduce the reader to a number of the key parameters that characterize the solar cell output and lead to the efficiency of a cell. Therefore, arbitrary

values are chosen and meaning is applied to these parameters in the text that follows.

### 2.3 Output of a Silicon Solar Cell

Figure 2.2 shows the JV plot of a solar cell according to the circuit model introduced in this previous section. A number of important output parameters are labeled in Figure 2.2, including the open circuit voltage,  $V_{oc}$ , the short circuit current density,  $J_{sc}$ , the maximum power point voltage  $V_{mp}$ , the maximum power point current density,  $J_{mp}$ , and the fill factor, FF.

The short circuit current density is the current that flows through the solar cell when its output terminals are shorted together. As can be seen in Figure 2.2, there is no voltage at the short circuit condition. If the terminals of the circuit model in Figure 2.1 were shorted, then so long as the series resistance of the cell remains small enough,  $J_{ph} = J_{sc}$ .  $J_{sc}$  is the maximum current density that can be delivered to a load.

If the terminals of the solar cell are left open, or not connected to a load, then a voltage will develop at the output terminals, known as open circuit voltage,  $V_{oc}$ . This voltage, represents the maximum voltage value that can be obtained from a cell. At the open circuit condition, the current output is non-existent, therefore a relationship can be obtained for the open circuit voltage. This relationship is,

$$V_{oc} = (kT/q) \ln((J_{ph}/J_0) + 1) \quad (2.5)$$

where  $k$ ,  $T$ ,  $J_{ph}$ , and  $J_0$  have their previously defined meanings, and  $q$  is the elementary electron charge of  $1.6 \times 10^{-19}$  C. To derive this relationship, it is necessary that the shunt resistance be sufficiently high so that the term  $V/R_{sh}$  can be neglected. This assumption is viable as modern industrial and laboratory solar cells have  $R_{sh} > 1000 \Omega \cdot cm^2$ .

Any combination of voltage and current density values along the curve between  $J_{sc}$  and  $V_{oc}$  represents power that can be delivered to a load. The maximum power point occurs on the curve where the value of  $V * J$  is found to be the highest. These two points are named the maximum power point voltage and current,  $V_{mp}$  and  $J_{mp}$  respectively. The ratio of  $V_{mp}J_{mp}$  to  $V_{oc}J_{sc}$  is known as the fill factor, or FF. This ratio represents a practical form of the FF

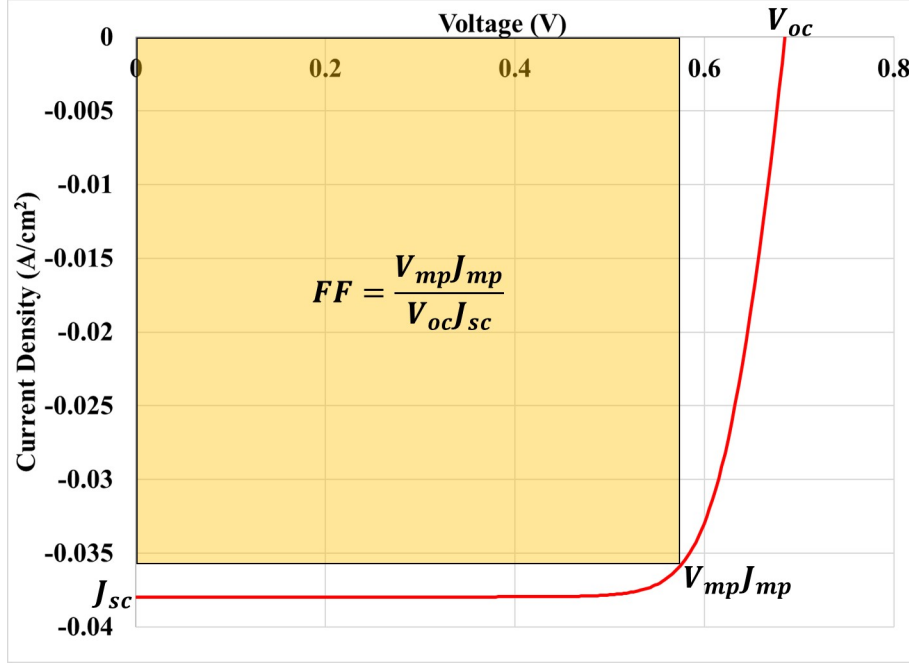


Figure 2.2: JV curve for a solar cell modeled by the circuit model of Figure 2.1 with  $J_{ph} = 38$  mA/cm<sup>2</sup>,  $J_0 = 1 \times 10^{-13}$  A/cm<sup>2</sup>,  $R_{sh} = 10,000 \Omega - cm^2$ , and  $R_{ser} = 1 \Omega - cm^2$ .

that takes into account many of the non-ideal losses that occur in a cell, such as the series resistance and shunt resistance. However, for cells with very low series resistance and very high shunt resistants (e.g. the highest performing cells), the FF maximum is set empirically by [18],

$$FF = (v_{oc} - \ln(v_{oc} + 0.72)) / (v_{oc} + 1) \quad (2.6)$$

where  $v_{oc}$  represents a normalized open circuit voltage and is given by,

$$v_{oc} = (q/kT)V_{oc} \quad (2.7)$$

To obtain maximum values of FF, it is necessary to maximize the open circuit voltage.

The overall efficiency of a solar cell can be defined as,

$$\eta = P_{out} / P_{in} \quad (2.8)$$

where  $P_{out}$  represents the output power of the cell and  $P_{in}$  represents the input power of the cell. From the above discussion, at maximum powerpoint,

$$\eta = P_{out}/P_{in} = J_{mp}V_{mp}/P_{in} = (V_{oc}J_{sc}FF)/P_{in} \quad (2.9)$$

The  $P_{in}$  for a solar cell is determined by the incident flux of photons from a given light source, where as  $P_{out}$  is determined from  $V_{oc}$ ,  $J_{sc}$ , and the  $FF$ . For maximum cell efficiency the  $V_{oc}$ ,  $J_{sc}$ , and  $FF$  must all be maximized. This is accomplished by maximizing the generation of electron-hole pairs within a solar cell and minimizing recombination processes. Both of these topics are now explored.

## 2.4 Absorption of Light and Generation of Charge Carriers

The sun emits electromagnetic radiation at a number of wavelengths ranging from 250 to 4000 nm as shown in Figure 2.3. Two curves are shown here, one is called the Air Mass 0 (AM0) curve and the other is called the AM 1.5 Global (G) curve. The data for the two curves comes from the SMARTS, or Simple Model of the Atmospheric Radiative Transfer of Sunlight, program[19, 20]. The spectra in Figure 2.3 represent international standards which give the spectral irradiance produced by the sun at the outer atmosphere, AM0, and that which is used for terrestrial applications, AM1.5G. The area beneath the AM1.5G curve has been highlighted yellow. If the total irradiance is integrated over all wavelengths, then one can arrive at a total integrated current density that a flat plate solar collector could produce assuming one photon creates one charge within the solar collector. For the entire spectrum available at earths surface (AM1.5G), a device could collect as much as 73 mA/cm<sup>2</sup> of current density.

It is the job of a solar cell to convert as much of the spectrum as it can to a usable electrical current. For a silicon solar cell, it can collect that portion of the spectra up to where the vertical bar is shown in Figure 2.1, about 1100 nm. The reason for this is because Si is a semiconductor material that has a bandgap that limits the amount of light that can be collected and converted to an electrical current. The total maximum amount of current that any Si solar cell can produce, on earth, is no greater than 46 mA/cm<sup>2</sup>.

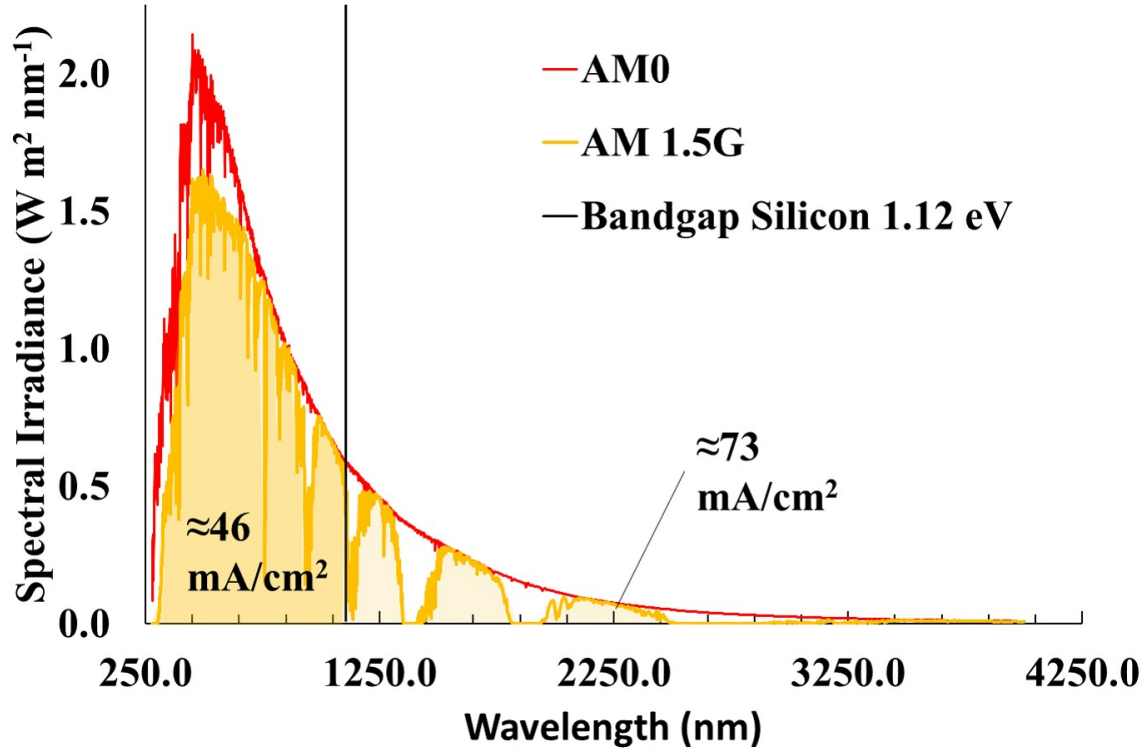


Figure 2.3: Solar spectrum radiation for wavelengths of interest to silicon solar cells. The vertical black line denotes the bandgap of Si. The total amount of current density that any silicon solar cell can obtain is no greater than  $46 \text{ mA/cm}^2$ .

Careful optical management is necessary for a Si solar cell to collect a total of  $46 \text{ mA/cm}^2$  of the solar radiation available. As shown in Figure 2.4, the radiation incident on a Si material might be reflected, absorbed or transmitted.

In fact, owing to its index of refraction, for a planar Si surface, 33% of the radiation incident on the surface will be reflected. The remaining 67% passes through the Si material where it is either absorbed, or reaches the back surface undergoing a secondary reflection and possible transmission through the material. Reflections from the front surface are mitigated in modern solar cells with the implementation of front surface texture and anti-reflection coatings. Such techniques are designed to reduce reflection most optimally around wavelengths of 500 nm, as this coincides with the peak of incident power. Regarding transmission, modern Si solar cells are around  $180 \mu\text{m}$  thick, and are trending thinner[2]. The fraction of light that can be transmitted through the entire thickness of Si is heavily dependent upon its absorp-

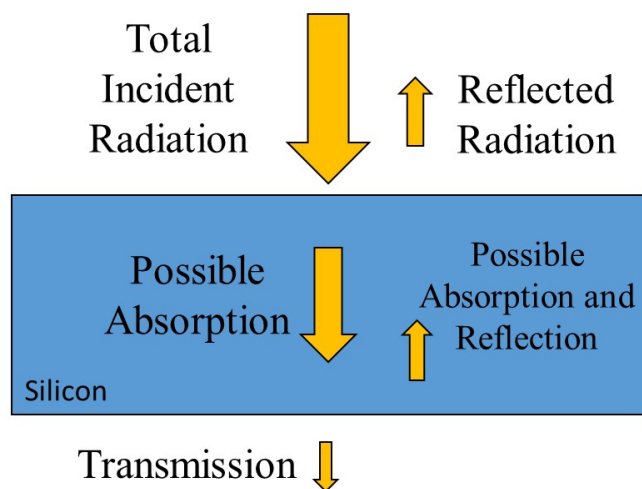


Figure 2.4: Diagram indicating possible transmission, reflection or absorption pathways in silicon.

tion coefficient as shown Figure 2.5 (the data comes from [21, 22]). The absorption coefficient of Si (blue) plotted with the absorption depth (red) for wavelengths of radiation ranging from 300-1150 nm. The absorption depth is the mathematical inverse of the absorption coefficient plotted here in units of thickness that are meaningful for Si solar cells. The absorption depth effectively shows how deep a given wavelength of light penetrates the Si. For wavelengths of light, 800 nm or less, the radiation penetrates no deeper than  $10\ \mu\text{m}$  into the material, but for wavelengths at 1000-1100 nm, most of this light can pass through a modern Si solar cell of  $180\ \mu\text{m}$  thickness, if it is not absorbed in the material itself. The absorption coefficient is shown to decrease significantly toward zero around the bandgap of Si, 1100 nm.

The importance of the data in Figure 2.5 is that Si solar cells must be designed to prevent radiation from 1000 to 1100 nm from transmitting through the material. Absorption inside the material plays a role in this, but careful design of the backside is also important to mitigate optical losses. It is useful to have the back surface entirely coated with a reflector suitable for reflecting longer wavelengths of radiation. Modern cells incorporate this by applying metal to the entire backside of the device. A cross sectional view of a modern device architecture is given in Figure 2.6 and shows those features that maximize the light collection capability of the Si solar cell.



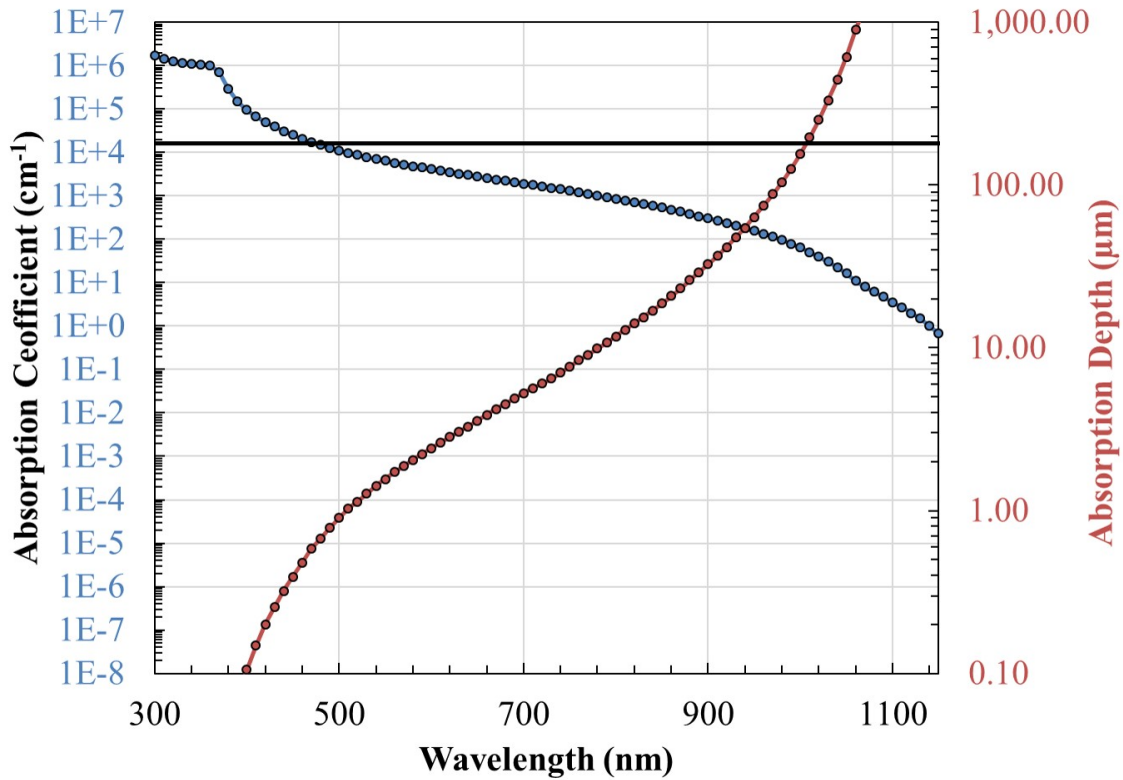


Figure 2.5: Absorption coefficient (blue) and absorption depth (red) of silicon.

The optical management of modern cells has been engineered to maximize the amount of light captured from the spectrum shown in Figure 2.3. In fact, most modern Si solar cells capture light effectively between 400 to 1000 nm due to this optical engineering. As illustrated in Figure 2.6, features that maximize the collected light include pyramidal front surface texturing, an AR coating and a metal back reflector (usually doubling as a back conductor). With modern cell architectures it is more important to turn the attention of the design for a cell toward the internal electronic processes that occur within the Si material. This is done by minimizing the internal recombination processes.

Absorption in semiconductors occurs when light having energy in excess of the bandgap passes through the Si. This is true for all of the radiation emitted from the sun up to about 1100 nm in wavelength. The energy of the radiation, most often in the form of a photon, gives its energy to that of an electron inside the material. Conceptually, this is shown in Figure 2.7,

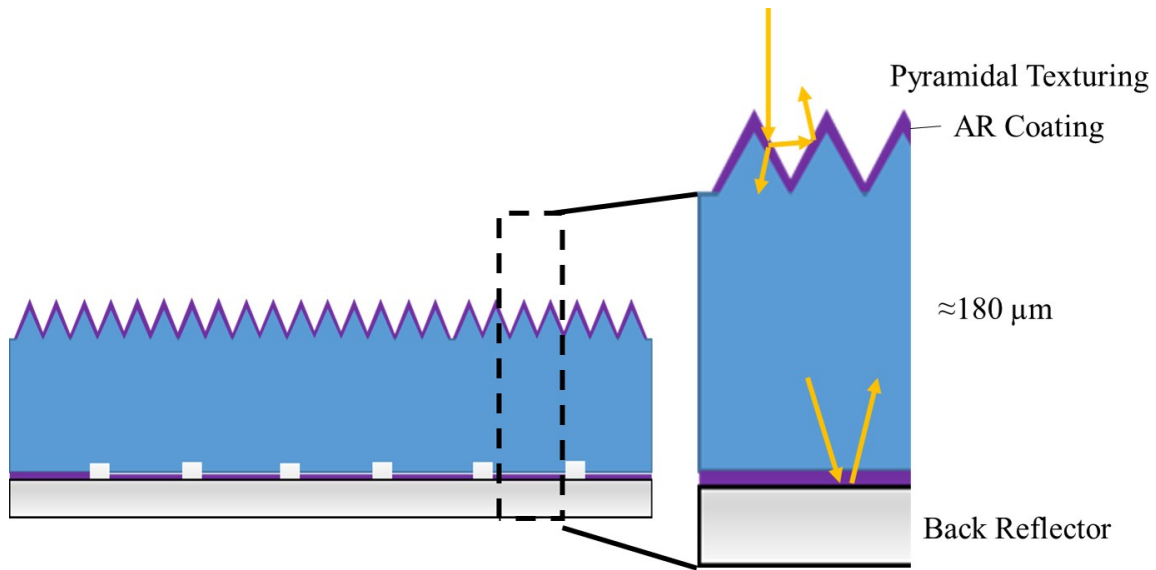


Figure 2.6: Diagram indicating the effect of texture and a back reflector on the optical management of a solar cell.

which shows the energy of a photon (yellow arrow) exciting an electron (yellow circle) to a state that is above the energy level of the conduction band,  $E_c$ . The electron leaves behind an empty state in the valence band (empty circle in Figure 2.7), which is a hole.

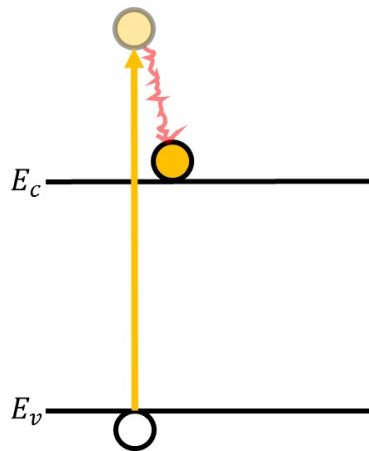


Figure 2.7: Schematic of the excitation of an electron in the valence band due to an absorption event. The red arrow indicates thermalization of the electron to the conduction band edge.

The difference in energy between the conduction band and the valence band is known as the bandgap. This is an energy bandgap that represents a range of energy values where states for electrons are not allowed. The valence band represents those electrons that are held to an

atom and do not have enough energy to become free of the bonds holding it in place. When light passes through the semiconductor, it gives its energy to an electron in the valence band, exciting it, often, to a value greater than the bandgap, 1.1 eV in Si. This electron then thermalizes and decays back down to an energy level known as the conduction band, shown as the red arrow in Figure 2.7. This band represents the energy levels for which electrons can freely conduct or move about in the Si material. The thermalization process represents scattering and the loss of energy in the form of phonons, or lattice vibrations, to the material.

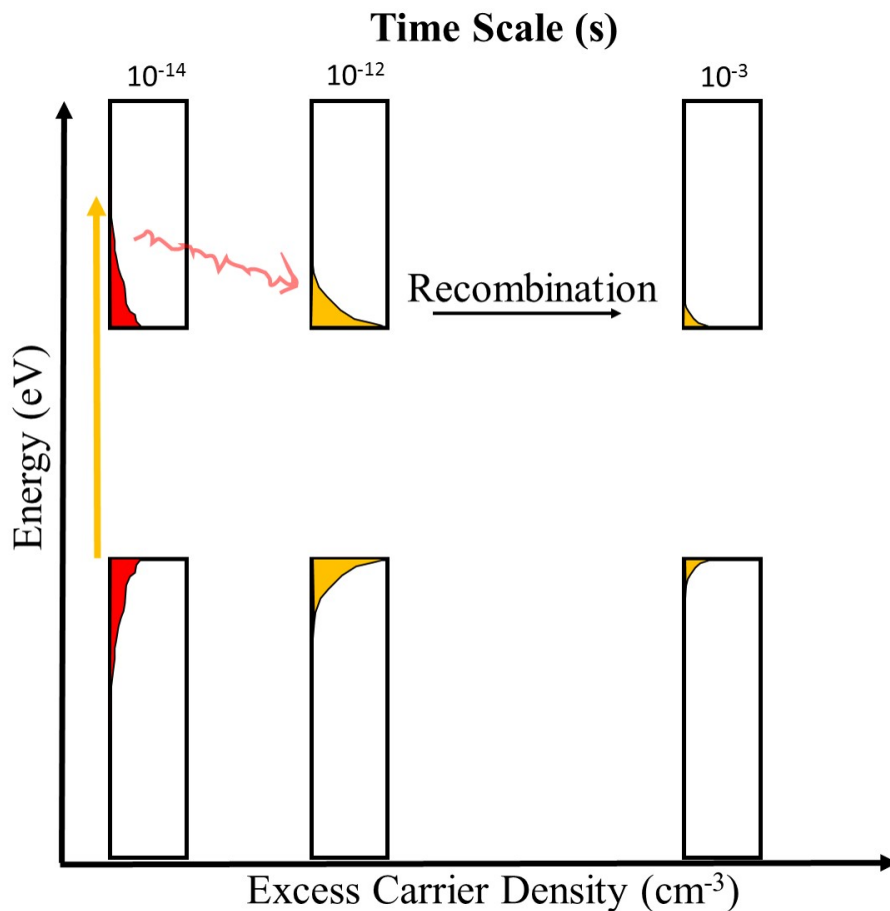


Figure 2.8: Relevant time scales involved with absorption, thermalization, and recombination processes in silicon against excess carrier density. Box plots indicate different time scales.

Figure 2.8 shows a plot of the energy levels present in a semiconductor, such as Si, against the excess carrier density that is produced as a result of the radiation, or absorption processes [23]. The gap between the lower and upper sets of boxes represents the bandgap of the mate-

rial. The yellow arrow indicates an absorption process. After the thermalization process occurring on the time scale of  $10^{-12}$  seconds, the distributions spread out reaching a point of thermal and chemical equilibrium within their respective bands. These electrons and holes can survive until they recombine, which in very pure Si can take as long as 10 to 100 ms of time. The average Si material used in modern solar cells may have lifetimes on the order of 0.5-4 ms.

To create solar cells with the highest efficiency it is necessary to maximize the time before recombination occurs within the device. This time, known as the carrier lifetime, is dependent upon the carrier density, both the equilibrium density (that obtained without exposure to illumination), and the excess density created due to illumination and excitation of electrons to the conduction band. Generally, the lifetime can be defined as,

$$\tau = \frac{\Delta n}{U}(\text{p-type Si}) \quad (2.10)$$

$$\tau = \frac{\Delta p}{U}(\text{n-type Si}) \quad (2.11)$$

where  $\tau$  is the total recombination lifetime, and  $U$  represents the net recombination rate. The carrier lifetime refers to the minority carrier lifetime. The minority carrier can either be an electron (p-type Si) or a hole (n-type Si), in which case equations 2.10 or 2.11 describe the recombination lifetime. The quantities  $\Delta n$  and  $\Delta p$  represent the excess density of electrons and holes,

$$\Delta n = n - n_0 \quad (2.12)$$

$$\Delta p = p - p_0 \quad (2.13)$$

where  $n$  and  $p$  is the total number of electrons and holes, respectively, generated due to illumination and  $n_0$  and  $p_0$  represents the equilibrium densities of electrons and holes. The equilibrium concentrations arise from conditions within the semiconductor when it is not illuminated, that is when it is in the dark. The equilibrium densities can be obtained by integrating

their distribution over the number of allowed states in the conduction and valence band. Such an integration yields,

$$n_0 = N_c \exp((E_F - E_C)/kT) \quad (2.14)$$

$$p_0 = N_v \exp((E_V - E_F)/kT) \quad (2.15)$$

where  $N_c$  and  $N_v$  are the allowable densities of states in the conduction and valence band, respectively. The quantity  $E_F$  is the Fermi-energy level,  $E_C$  is the energy level of the conduction band, and  $E_V$  is the energy level of the valence band.  $k$  represents Boltzmann's constant, and  $T$  is the absolute temperature of the material. In an ideal Si material without any surfaces and no lattice defects, every electron that is thermally excited (there is no illumination in this case) leaves behind a hole in the valence band, so that  $n_0 = p_0 = n_i$  where  $n_i$  is known as the intrinsic carrier concentration. Multiplying the  $n_0$  and  $p_0$  together yields,

$$n_0 p_0 = n_i^2 = N_c N_v \exp(-E_g/kT) \quad (2.16)$$

where  $n_0 p_0$  is known as the equilibrium pn product and  $E_g$  is the bandgap of the material.

## 2.5 Recombination

The main recombination mechanisms in silicon are radiative recombination, shockley-read-hall (SRH) recombination, and Auger recombination. A depiction of the process that describes each of these mechanisms is given in Figure 2.9. Each of these mechanisms will be discussed in detail in the following subsections, however, we introduce the idea of recombination here by starting with the most straightforward way to consider it.

Recombination refers to the rate at which electrons and holes recombine to form electron hole pairs according to the following reaction equation,



where  $e^-$  represents a negatively charged electron,  $h^+$  represents a positively charged hole,

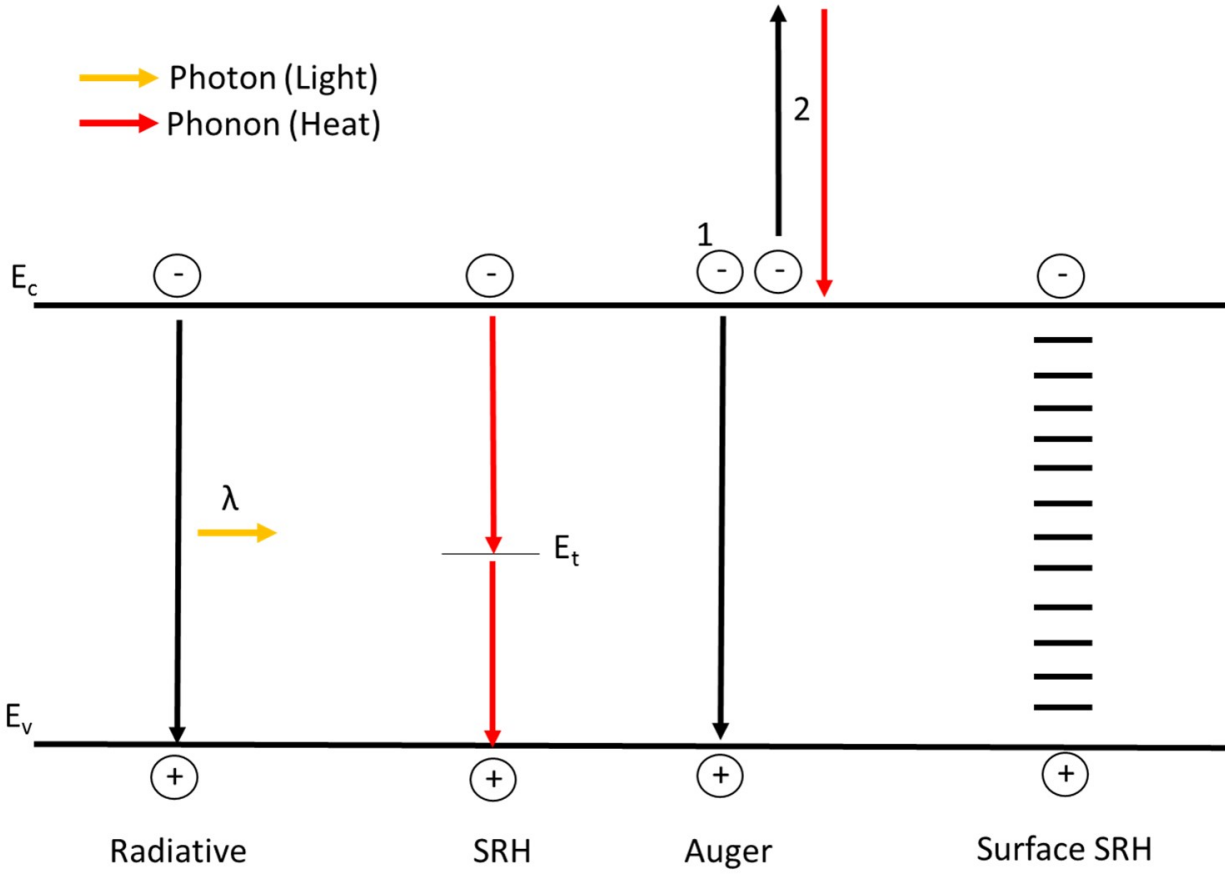


Figure 2.9: Diagram showing the different possible recombination mechanisms in silicon.

and  $h\nu$  refers to the energy, in the form of a photon, generated by the recombination of the electron and hole. Following the equation of the chemical reaction, an equation describing the reaction rate can be obtained,

$$R = R_0np \tag{2.18}$$

where,  $R$  is the recombination rate,  $n$  represents the density of electrons, and  $p$  represents the density of holes.  $R_0$  is given as the proportionality constant that determines the rate of the reaction. This type of equation describes the simple transition of an electron in the conduction band to a hole in the valence band. It most accurately describes the concept of band-to-band recombination. Many experiments have been undertaken, especially in the area of silicon photovoltaics, to form empirical models of the various recombination mechanisms. A brief review of each of these mechanisms follows.

Before discussing each recombination mechanism it is important to define an intrinsic recombination process versus an extrinsic recombination process. Intrinsic recombination processes, are those processes that are inherent to a material. That is, they are not created due to the manufacture of the material. No matter how chemically pure a piece of Si is, intrinsic recombination will still be present. Radiative recombination and Auger recombination are intrinsic processes. Extrinsic recombination refers to those recombination mechanisms that occur due to defects induced by creation of the material. Shockley-Read-Hall (SRH) recombination is an extrinsic recombination process.

### 2.5.1 Radiative (Band-to-Band) Recombination

Radiative recombination occurs when an electron in a conduction band minimum recombines with a hole in a valence band maximum. An analytic equation that describes radiative recombination is given by[18],

$$U_{rad} = B_{rad}(pn - n_{i_{eff}}^2) \quad (2.19)$$

where  $B_{rad}$  is the radiative recombination coefficient and is experimentally determined,  $n$  is the population of electrons,  $p$  is the population of holes, and  $n_{i_{eff}}$  is the effective intrinsic carrier concentration. Radiative recombination typically has a small impact in silicon devices owing to silicons indirect bandgap and because of the fact that other recombination processes are more dominant [24]. However, if a silicon sample is very pure, then the radiative recombination will have a significant impact. More recently, the temperature dependence of radiative recombination was explored using spectral photoluminescence with temperature resolution capability of 10K right around room temperature [25]. This work lead to an updated empirical expression for  $B_{rad}$ ,

$$B_{rad} = 10^{(-176.98+2.688T-0.018T^2+6.57 \times 10^{-5}T^3-1.21 \times 10^{-7}T^4+8.99 \times 10^{-11}T^5)} \quad (2.20)$$

Radiative recombination is considered an intrinsic recombination process and is a limitation to obtaining the highest possible efficiencies for a silicon solar cell [26].

### 2.5.2 Auger Recombination

Auger recombination is named after the physicist that discovered the phenomenon. In this case, an electron may give its energy to another electron in the process of recombining with a hole. This excited electron is driven above the conduction band edge and thermalizes back down to the band edge. The same process can be hole driven, where a hole recombines with an electron giving the energy to a hole. The processes are referred to eeh and ehh recombination. Auger recombination represents one of the largest loss mechanisms in solar cells, especially in those regions that are heavily doped. This is because there is an increased probability of Auger recombination in those regions having more charge carriers. An analytical form that approximates Auger recombination is given by [18],

$$U_{aug} = (C_n n + C_p p)(pn - n_{i_{eff}}^2) \quad (2.21)$$

Where  $p, n$ , and  $n_{i_{eff}}$  have their usual meanings and  $C_n$  and  $C_p$  represent the Auger coefficients for electrons and holes respectively. The most modern parameterization of Auger recombination is given as an intrinsic lifetime term,  $\tau_{intr}$  [27], with,

$$\tau_{intr} = \Delta n / ((np - n_{i_{eff}}^2)(2.55 \times 10^{-31} g_{eeh} n_0 + 8.5 \times 10^{-32} g_{ehh} p_0 + 3.0 \times 10^{-29} \Delta n^{0.92})) \quad (2.22)$$

where  $g_{ehh}$  and  $g_{eeh}$  are expressed as,

$$g_{eeh}(n_0) = 1 + 13(1 - \tanh((n_0/N_{0,eeh})^{0.66})) \quad (2.23)$$

$$g_{ehh}(p_0) = 1 + 7.5(1 - \tanh((p_0/N_{0,ehh})^{0.65})) \quad (2.24)$$

$$N_{0,eeh} = 3.3 \times 10^{17} \quad (2.25)$$

$$N_{0,ehh} = 7.0 \times 10^{17} \quad (2.26)$$

where the subscript  $eeh$  refers to an electron-electron-hole Auger process,  $ehh$  refers to a electron-hole-hole Auger process,  $\Delta n$  is the excess density of electrons, and  $g_{eeh}$  and  $g_{ehh}$  are known as



enhancement factors.

Auger is the other type of intrinsic recombination in crystalline silicon. In limiting efficiency calculations, Auger and Radiative recombination are treated together to express the minimum possible recombination [26].

### 2.5.3 Shockley-Read-Hall Recombination

SRH recombination is referred to as an extrinsic recombination mechanism as it is the only recombination mechanism that can be controlled by an optimal design. The phenomenon of SRH recombination involves an impurity center in the crystal lattice that places a localized energy level in the bandgap of a semiconductor. This energy level, or trap level, minimizes the required energy for electrons or holes to recombine. The usual form for such recombination is mathematically described by,

$$U_{srh} = (pn - n_{i_{eff}}^2) / (\tau_{n0}(p - p_1) + \tau_{p0}(n - n_1)) \quad (2.27)$$

Again,  $p, n$ , and  $n_{i_{eff}}$ , have their usual meaning. New variables introduced here include the electron and hole SRH lifetime,  $\tau_{n0}$  and  $\tau_{p0}$  and  $p_1$  and  $n_1$ . The SRH lifetime represents the lifetime of electrons or holes in the presences of a trap state.  $p_1$  and  $n_1$  give the distribution of the trap level based upon the given energy of the trap following,

$$n_1 = N_c e^{(E_t - E_c)/kT} \quad (2.28)$$

$$p_1 = N_v e^{(E_v - E_t)/kT} \quad (2.29)$$

where  $N_c$  and  $N_v$  represent the density of states in the conduction and valence bands and  $E_t$  is the energy of the trap level.

### 2.5.4 Surface Recombination

Surface recombination is taken to be a special case of SRH recombination. The truncation of the crystal lattice creates dangling bonds that act as recombination sites. In an energy band

view, these sites represent discrete levels in the band gap that facilitate recombination. The mathematical description of surface recombination follows,

$$U_{surf} = S_{e0}S_{h0}(np - n_{eff}^2)/(S_{e0}(n + n_1) + S_{h0}(p + p_1)) \quad (2.30)$$

Here, the  $S_{e0}$  and  $S_{p0}$  terms represent effective surface recombination velocities in units of cm/sec. This can best be explained by envisioning that the term represents the real velocity of the carriers as they approach a viable recombination site at the surface (either a dangling bond, or another state that has been generated).

## 2.6 Recombination Current

It is useful to cast the above recombination mechanisms into a formulation known as the recombination current density. To introduce this topic, the method of Cuevas is followed by examining the case of a near intrinsic silicon wafer having only Auger and Radiative recombination [28]. This discussion is based upon experimental work performed by Richter et. al. [27]. In that work, crystalline silicon wafers were prepared at two different labs using two different techniques to formulate a parameterization of the intrinsic lifetime of a silicon wafer. The parameterization relates the effective lifetime of the wafer to the excess number of carriers produced throughout the volume of the wafer due to illumination. For a given wafer thickness and doping density, a plot of the effective lifetime versus the excess carrier density can be produced. This parameterization is applied to 180  $\mu m$  thick wafer and a doping density of  $N_D = 1 \times 10^{-16} cm^{-3}$  to produce the curve shown in Figure 2.10. The blue data points represent the effective lifetime calculated at a particular excess carrier density. The effective lifetime is composed of two components in this case, the Auger lifetime component (given by the long dashes) and the Radiative lifetime component (given by the short dashes). For this example, the effective lifetime is completely determined by the Auger component.

The parameterization used to create the plot of Figure 2.10 was determined from wafers with high levels of surface passivation. This means that surface recombination can be neglected in Figure 2.10. Moreover, because of the high quality of the wafers, the assumption can be

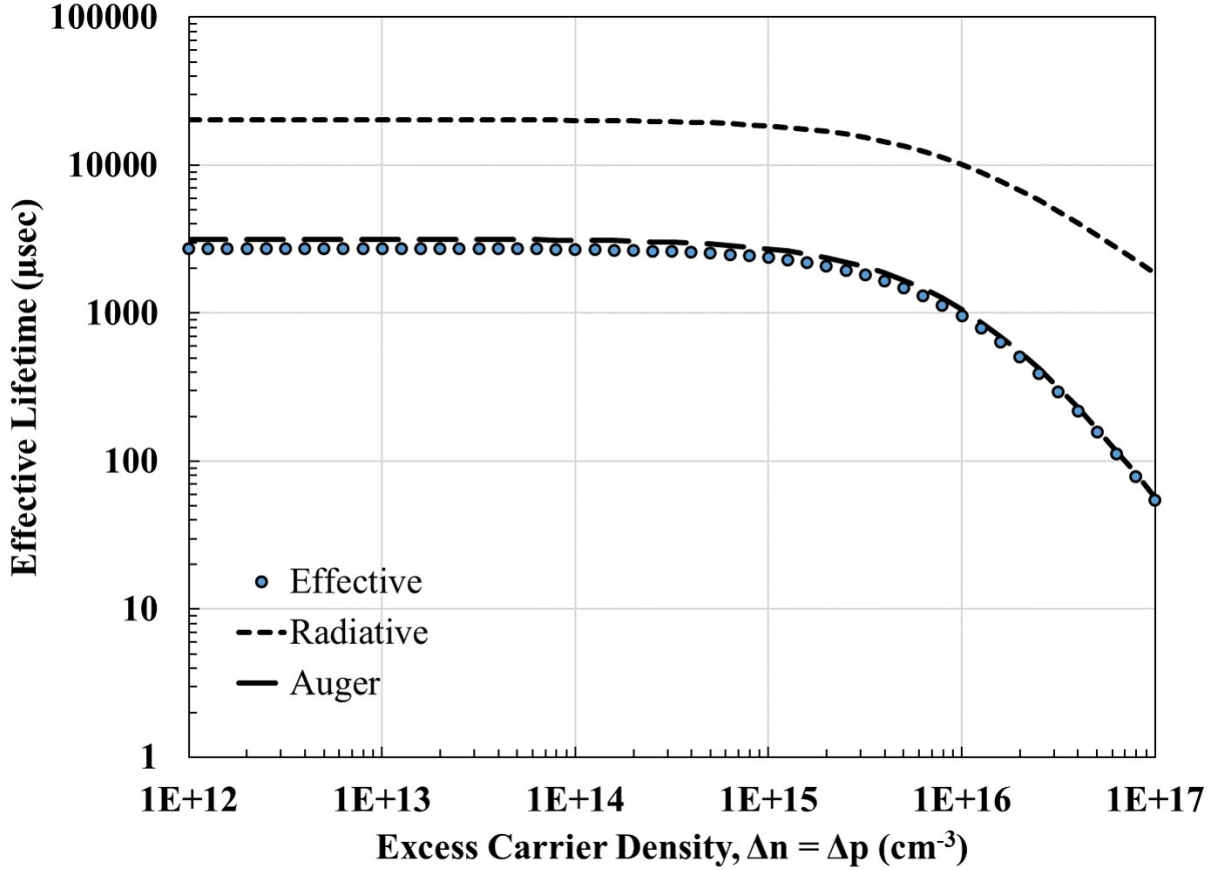


Figure 2.10: Plot of the effective lifetime of a  $180 \mu\text{m}$  thick n-type wafer with  $N_D = 1 \times 10^{-16} \text{cm}^{-3}$ .

made that the recombination is uniform throughout the bulk of the material. In this way, the cumulative recombination rate can include the thickness of the wafer such that,

$$R_{cum} = \frac{(\Delta p)W}{\tau_{eff}} \quad (2.31)$$

where  $R_{cum}$  represents the cumulative recombination rate throughout the wafer in units of  $\text{cm}^{-2}\text{s}^{-1}$ ,  $\Delta p$  is the excess number of holes generated in the n-type wafer due to illumination,  $W$  is wafer thickness in cm, and finally  $\tau_{eff}$  is the effective lifetime of the wafer.  $\tau_{eff}$  represents the carrier recombination lifetime of all the recombination mechanisms added together, thus producing a total effective lifetime. In general, the effective lifetime in any given region of a cell is made up of components each representing the recombination lifetime associated with a given mechanism,

$$\frac{1}{\tau_{eff}} = \frac{1}{\tau_{SRH}} + \frac{1}{\tau_{Rad}} + \frac{1}{\tau_{Aug}} + \frac{1}{\tau_{surf}} \quad (2.32)$$

but in this discussion regarding a wafer with only intrinsic recombination processes we have,

$$\frac{1}{\tau_{eff}} = \frac{1}{\tau_{Rad}} + \frac{1}{\tau_{Aug}} \quad (2.33)$$

For the case of band-to-band recombination, the recombination rate is proportional to the product of the electron and hole concentrations. To show this,  $R_{cum}$  from equation 2.30 is calculated from the effective lifetime data shown in Figure 2.10 and then plotted (in Figure 2.11) against the term  $pn/n_i^2$ , which is known as the normalized pn product.

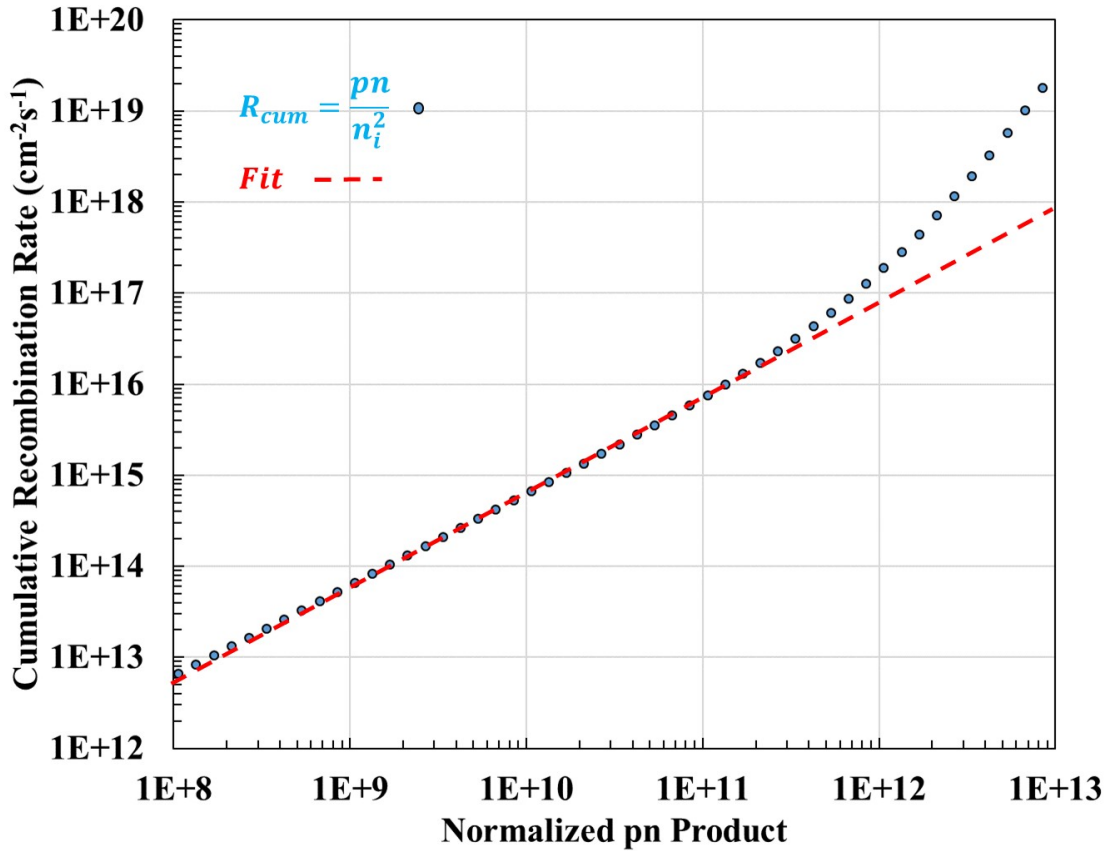


Figure 2.11: Plot of the lifetime of a 180  $\mu m$  thick wafer with  $N_D = 1 \times 10^{-16} cm^{-3}$ .

As can be seen Figure 2.11 the plot with the blue data points represents the cumulative recombination rate. Because  $n_i$ , from Eq. 2.33, is a constant value (at a particular temperature,

assumed here to be 300K), the cumulative recombination rate is proportional to the product of the concentration of the electrons and holes. This is with the exception of the recombination rate at higher values of the  $pn$  product, corresponding to high concentrations of, in this case, holes. The equation of the fit line,

$$R_{cum} = \frac{R_0 pn}{n_i^2} \quad (2.34)$$

shows that over a wide range of carrier densities, the recombination can be fit by a factor  $R_0$ . For the data shown in Figure 2.11, a good fit is found for  $R_0 = 7.39 \times 10^4 \text{cm}^{-2}\text{s}^{-1}$ . When  $R_0$  is multiplied by the electron charge,  $q$ , units of  $\frac{\text{C}}{\text{s}\cdot\text{cm}^2}$  are obtained. This can be interpreted as a current density,  $J_0$ , whose value in this case is  $1.18 \times 10^{-14} \text{A}/\text{cm}^2$ . The recombination in a region of the device can then be treated as a current density, which for the given case, is for an entire wafer with well passivated surfaces.

## 2.7 A Recombination Current Model of a Solar Cell

In this section, a cross sectional model of a n-type silicon solar cell is created. The purpose here is to show that the various regions of a solar cell device each have their own recombination current density.

Figure 2.12 shows a cross sectional diagram of a modern n-type silicon solar cell with various regions of the device labeled with different recombination current densities.

The term  $J_{0em}$  refers to the recombination that occurs as a result of the metal interfacing with the heavily doped region at the front of the cell known as the emitter. For an n-type cell, such as that shown, the emitter region is doped with boron and so it is a p+ emitter.  $J_{0e}$  refers to the recombination occurring within the bulk of the emitter region and at its surface.  $J_{0b}$  is the recombination associated with the base or bulk of the solar cell, here doped with phosphorous making it n-type.  $J_{0bsf}$  refers to the back surface field region of the solar cell, doped n+ with phosphorous, and like the emitter region, this term represents the recombination occurring within the bulk of the BSF and at its surface. Finally, the term  $J_{0bsfm}$  represents recombination occurring where metal makes contact to the the solar cell surface.

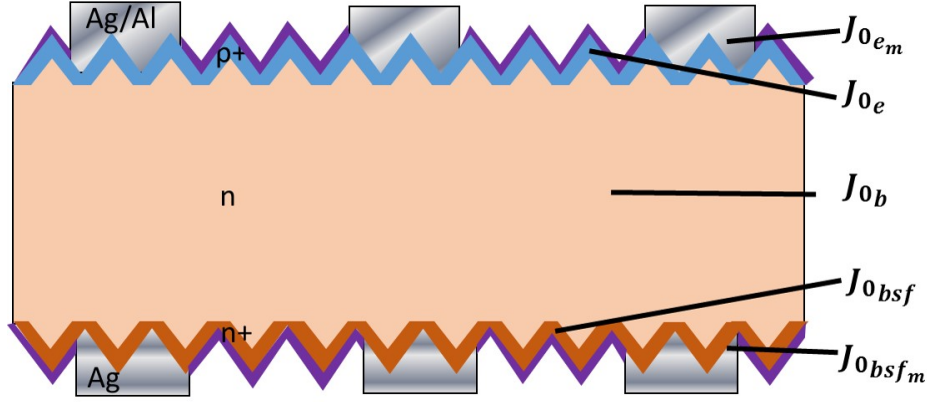


Figure 2.12: Cross sectional model for a n-type solar cell with various regions labeled by recombination current density.

Mathematically, each of the  $J_0$  terms in Figure 2.12 can be summed together to create the total  $J_0$  of the device,

$$J_0 = fJ_{0em} + J_{0e} + J_{0b} + J_{0bsf} + fJ_{0bsfm} \quad (2.35)$$

The total  $J_0$  term is the same term that is used in equation 2.5 that places a limit on the  $V_{oc}$  of the solar cell. The  $f$  coefficients on the  $J_{0em}$  and  $J_{0bsfm}$  terms represents the fractional coverage of metal on the front and back of the device respectively. For instance, if the total grid coverage on the front of the device was 5% of the area, then  $f = 0.05$  and for a cell with a full area metal back contact  $f = 1$ . Equation 2.35 is a good approximation for most silicon solar cells under normal operating conditions, but there are exceptions where this model may not hold [28].

Each of the terms in equation 2.34 can be further broken down into radiative, surface, SRH, or Auger recombination components in the region described that recombination current density term. The term of most importance for the work in this dissertation is that of  $J_{0e}$ . In terms of the fundamental recombination components,  $J_{0e}$  can be expressed as,

$$J_{0e} = J_{0e_{rad}} + J_{0e_{SRH}} + J_{0e_{Aug}} + J_{0e_{surf}} \quad (2.36)$$

Emitters are heavily doped regions, and therefore a few of the terms in equation 2.35 can be neglected. These include  $J_{0erad}$  and  $J_{0eSRH}$ . This leaves two terms which have to be minimized to reduce overall  $J_{0e}$ . That is the Auger component of the recombination and the surface component. In this dissertation, the auger component is reduced by inactivation of the boron atoms in the emitter by atomic hydrogen and the surface component is reduced through excellent passivation provided by quinhydrone-methanol.

## 2.8 Summary

This section was concerned with introducing the reader to the operation of a silicon solar cell with regard to the the recombination current density. The efficiency of the cell is linked to  $J_0$  through the open circuit voltage. Lowering  $J_0$  results in an voltage boost and efficiency increase for the cell. It was shown that the components of concern in the emitter region are Auger recombination and the surface recombination component.

## Chapter 3

### Methods of Characterization and Data Analysis

Many characterization techniques were used in this dissertation. This chapter provides an overview of each of the inclusive methods so as to familiarize the reader with how results were obtained. These descriptions are not meant to be exhaustive, but are meant to provide a solid (at least conceptual) understanding of each method. Overviews of experimental methods are presented in the respective section where experimental results are contained.

#### 3.1 Photoconductance Lifetime Spectroscopy

Photoconductance Lifetime (PC- $\tau$ ) Spectroscopy is a method of illuminating a sample while either simultaneously measuring its photoconductance or measuring photoconductance as the generated light decays in the sample. The setup for such a measurement is shown in Figure 3.1, which shows the Sinton Instruments WCT-120 Photoconductance Lifetime measurement tool. The setup includes a platform on top of which a sample is placed. Inside this platform, proprietary electronics are contained that inductively measure the samples photoconductance via an eddy current sensor that is housed in the measurement platform. Above the platform and sample there is a flash lamp, capable of producing an intensity of light many times the sun's intensity on earth. This equipment, coupled with a CPU, allows for measurement of the effective lifetime, recombination current density of the emitter,  $J_{0e}$ , and the resistivity of the sample under test.

A bridge circuit inside the platform is connected to an inductive coil and RF generator. The generator operates at a frequency so as to ensure the full penetration of the resulting field formed from the energized coil into the wafer. A NIST traceable photodetector sits on top of the platform and serves the dual purpose of sensing when the lamp has flashed and also detecting the intensity of the light in units of suns. The bridge circuit measures a voltage produced by the inductive coil. This measured voltage changes in the presence of a sample above the coil, as the sheet conductivity of the sample can alter the voltage of the measurement coil. The instrument has three different modes of operation: the transient mode, the quasi-steady-



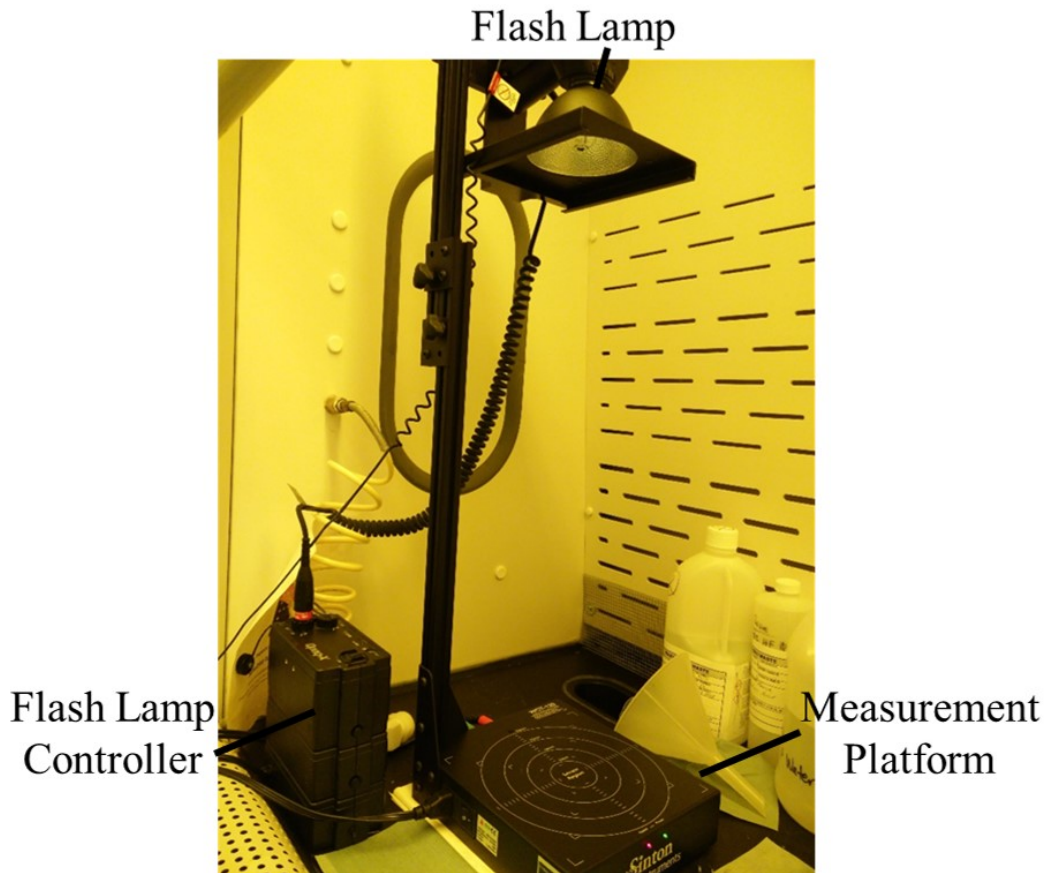


Figure 3.1: Photograph showing the Sinton Instruments WCT-120 Photoconductance Lifetime measurement tool.

state (QSS) mode, and the generalized mode. Each of these modes is selected as an option in the software that is used with the WCT-120. The different modes rely upon different flash lifetimes, that is, the amount of time that the flash of light from the lamp lasts. In the QSS mode, the decay of the light from the lamp should be at least 10 times slower than the carrier lifetime in the sample under test [29]. For the transient mode, a short light pulse is used that has a total duration of 100-200  $\mu\text{sec}$ . In this case, the system relies upon the generated carriers in the material lasting longer than the length of the flash. For a valid transient measurement, the lifetime of the carriers must be greater than 100  $\mu\text{sec}$ . The user is required to adjust the lamp flash settings manually, depending on which mode is used. The different modes correspond to different models that are applied to the measured coil voltage that allow extraction of key parameters. The most general version of the applied models is in the generalized

mode. To obtain the model from which the effective lifetime is obtained, the continuity equation for semiconductors is used [30]

$$\frac{\partial \Delta n}{\partial t} = G - U + \frac{1}{q} \nabla J. \quad (3.1)$$

In equation 3.1,  $\Delta n$  represents the number of excess minority carriers that are generated due to the illumination,  $G$  is the photogeneration from the flash lamp,  $U$  represents the recombination rate,  $q$  is the elementary charge, and  $J$  is the current density (electron in this case).

The light from the flash lamp of the WCT-120 is filtered through a IR-pass filter plate. This ensures that the light the sample under test is exposed to, uniformly illuminates the sample over its depth, ensuring uniform photogeneration. If it is assumed that the sample has perfect surface passivation, then the carrier density inside the material will be uniform over the sample depth. In this case, the last term in equation 3.1 can be removed, leaving,

$$\frac{\partial \Delta n}{\partial t} = G - U. \quad (3.2)$$

The well known relationship between carrier lifetime ( $\tau$ ), the excess carrier density, and the recombination rate[18],

$$U = \Delta n / \tau \quad (3.3)$$

can be inserted into Equation 3.1. This results in,

$$\frac{\partial \Delta n}{\partial t} = G - \frac{\Delta n}{\tau}. \quad (3.4)$$

which replacing  $\tau$  with  $\tau_{eff}$  and performing some algebraic manipulation results in,

$$\tau_{eff}(\Delta n) = \frac{\Delta n(t)}{G(t) - \frac{d\Delta n(t)}{dt}}. \quad (3.5)$$

Now depending on how long the flash from the lamp above the WCT-120 lasts, leads to either the QSS or transient mode of operation. If the total amount of photogeneration,  $G(t)$  is much

greater than the time rate of change of the excess carrier density ( $G(t) \gg \frac{\delta n}{dt}$ ), then equation 3.5 is simplified to,

$$\tau_{eff}(\Delta n) = \frac{\Delta n(t)}{G(t)} \quad (3.6)$$

which is the model used in the QSS mode. For the transient mode, the flash is much shorter and therefore the change in excess carrier density within in the sample is much larger than the photogeneration ( $G(t) \ll \frac{\delta n}{dt}$ ). This causes equation 3.5 to simplify to,

$$\tau_{eff}(\Delta n) = \frac{\Delta n(t)}{\frac{d\Delta n(t)}{dt}}. \quad (3.7)$$

which is valid for the transient mode of operation. The lifetime of the flash length is measured by the NIST traceable photoconductor in the WCT-120 measurement platform. The generation in the material is assumed to only change depending on the finish of the surface and thickness of the sample. An optical constant factor,  $f_{opt}$ , adjusts the amount of measured generation for use in the model. For the WCT-120, a value of  $f_{opt} = 1$  corresponds to a wafer that would create a current density of  $38 \text{ mA/cm}^2$ , whereas a sample with a highly reflected polished surface would be assigned an optical constant of 0.7. The transient mode of operation does not require measurement of the  $G(t)$ , and in this case, the photoconductor simply serves as a trigger to notify the software when the flash lamp has turned on.

The remaining factor to determine in equations 3.5, 3.6, or 3.7 to obtain the term  $\tau_{eff}$  is that of the excess carrier density  $\Delta n(t)$ . This is where the eddy current sensor and RF bridge circuit come into play. When the sample is illuminated, its photoconductivity,  $\sigma_L$  changes due to the generation of excess electron-hole pairs. The RF bridge circuit measures the sample during the duration of the decay of the lamp flash. This measured bridge voltage is fit with a quadratic function against the wafer conductivity, but for most measurement ranges of interest this output is linear and is approximated by,

$$\sigma_L = K_B V_B \quad (3.8)$$

where  $K_B$  is a constant of proportionality for a linear fit to the measured bridge voltage  $V_B$ . The photoconductance  $\sigma_L$  can be related to the wafer thickness, wafer mobility, and average minority carrier density according to [31],

$$\sigma_L = q(\mu_n + \mu_p)\Delta n_{av}W \quad (3.9)$$

The average carrier density  $\Delta n_{av}$  is calculated based upon the measured voltage, and the mobility values ( $\mu_n$  and  $\mu_p$ ) are assumed to be known based upon tabular values from the literature and  $W$  is the sample thickness (in cm). The effective lifetime of the wafer can then be calculated according to the equation,

$$\tau_{eff} = \frac{\sigma_L}{J_{ph}[\mu_n + \mu_p]W} \quad (3.10)$$

where  $J_{ph}$  is a current density representing the amount of generation in the sample, due to the term  $qG$ . The term  $qG$  is found when solving for  $\Delta n$  in equation 3.9 and then plugging it into equation 3.6. This solution is valid for the QSS mode of operation. For the transient mode of operation the average carrier density is calculated from the illuminated photoconductivity,  $\sigma_L$ , given in equation 3.9. This carrier density is then divided by its rate of change with time as given by equation 3.7.

### 3.1.1 Extraction of Bulk Lifetime and Surface Recombination

The carrier lifetime is one of the most, if not the most, important parameter for creating devices, specifically silicon solar cells. The carrier lifetime is sensitive to the temperature of processing conditions that the silicon samples are exposed to. To that end, it can be useful to characterize the bulk lifetime of wafers before and after a process. A key way to do this is using PC- $\tau$  measurements. For a bulk silicon wafer featuring no diffusions on either surface a simple model can be created to describe the total effective lifetime of the wafer. This model is,

$$\frac{1}{\tau_{eff}} = \frac{1}{\tau_{bulk}} + \frac{2S}{W}. \quad (3.11)$$

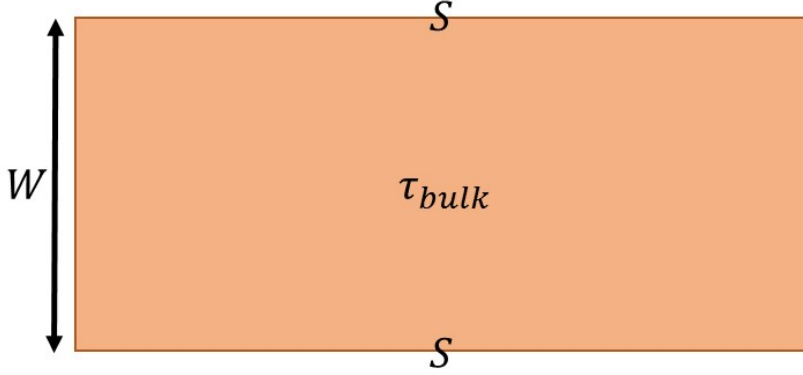


Figure 3.2: Graphic depicting the bulk of a silicon wafer and its two surfaces from which the effective lifetime can be found.

Equation 3.11 mathematically describes what is shown in Figure 3.2, a graphic of a silicon wafer having a lifetime described by its bulk properties and then a surface recombination velocity (SRV) term for each of its surfaces. The fact that the sample has two surfaces leads to the last term of equation 3.11. It is assumed, in this case, that the SRV of the front and back surfaces is equal. It is necessary to remove either  $\tau_{bulk}$  or  $S$  so that the measured  $\tau_{eff}$  gives us either the surface or bulk contribution. A standard measurement method is to assume that  $\tau_{bulk}$  is high, such that the term  $\frac{1}{\tau_{bulk}}$  can be neglected [32]. This method is valid when using wafers that are known to have high bulk lifetimes, such as FZ silicon. If the bulk lifetime is high, then the bulk term in equation 3.11 becomes negligible, and the measured effective lifetime is essentially equal front and back SRV. Obviously, the lower the actual bulk lifetime is in this method, more error will be introduced into the measurement of the surface lifetime. This also only works assuming that the diffusion length of the generated carriers exceeds that of the wafer thickness,  $W$ . If this condition is met, then carriers that are generated in the bulk of the silicon can diffuse toward the surface, and therefore, the recombination activity is sampled with the eddy current sensor. The diffusion length of the generated carriers in silicon can be calculated assuming a known diffusivity for the carriers and a known lifetime. The equation for calculating the diffusion length is [18],

$$L = \sqrt{D\tau}. \tag{3.12}$$

This equation can be applied to either electrons or holes as a minority carriers in either p-type or n-type silicon. Since the silicon used in this dissertation is all n-type, the focus here will be on the diffusion length of holes in the bulk of an n-type silicon wafer. A good estimate for the diffusivity of holes in silicon at 300 K is around  $12 \text{ cm}^2/\text{sec}$ . Taking this value for  $D$  in equation 3.12 a plot of diffusion length versus lifetime can be generated. Figure 3.3 shows a plot of the diffusion length against lifetime with a value of  $12 \text{ cm}^2/\text{sec}$  for hole diffusivity.

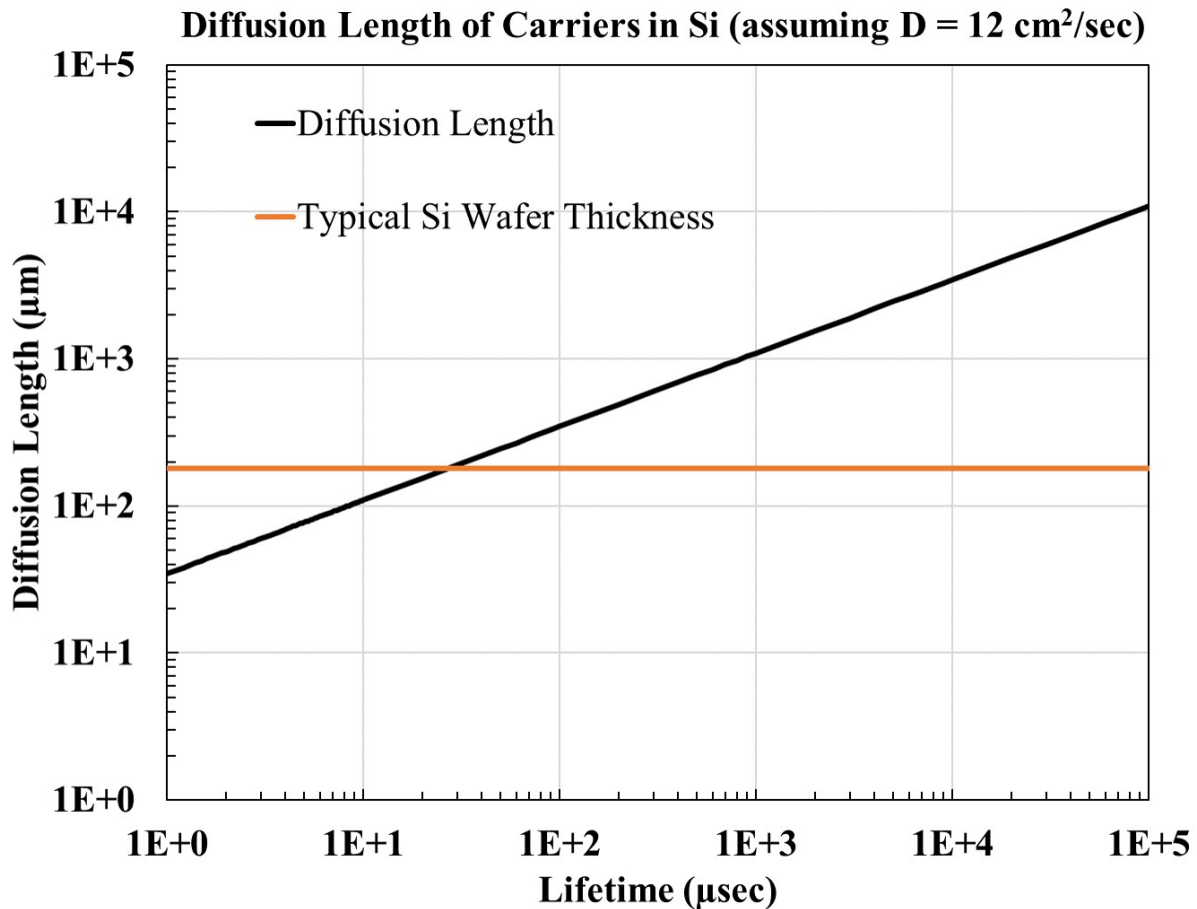


Figure 3.3: Plot of diffusion length against lifetime from equation 3.12, assuming a fixed value of  $D = 12 \text{ cm}^2/\text{sec}$  for minority holes in n-type silicon.

Figure 3.3 also shows a horizontal line that represents the thickness of an average industrial silicon wafer,  $180 \mu\text{m}$ . The intersection of the wafer thickness with the black line that represents diffusion length, gives the minimum lifetime that a wafer could possess in order for the generated carriers to diffuse and reach the surface. For a typical  $180 \mu\text{m}$  wafer, this is found to be around  $30 \mu\text{sec}$ , a quantity that is much less than the typical n-type wafer lifetime.

To extract the bulk lifetime, one must make the  $S$  term as small as possible so that it can be neglected. The preferred method of extraction  $\tau_{bulk}$  is by applying a dielectric coating that gives very low SRV enabling for extraction of  $\tau_{bulk}$ . This is accepted and practiced in solar research [32]. Common coatings include silicon dioxide (grown thermally) and silicon nitride (typically deposited using plasma enhanced chemical vapor deposition) [33]. Other methods use a liquid passivant such as hydrofluoric acid or (as in this dissertation) quinhydrone-methanol [34]. These liquid solutions do not provide a permanent solution to the issue of surface passivation. However, they can be used as diagnostic tools in evaluating the bulk lifetime of wafers. The bulk lifetime of the wafer can be broken into each of its recombination components such that,

$$\frac{1}{\tau_{bulk}} = \frac{1}{\tau_{rad}} + \frac{1}{\tau_{SRH}} + \frac{1}{\tau_{Aug}} \quad (3.13)$$

where  $\tau_{rad}$  refers to the lifetime due to radiative recombination,  $\tau_{SRH}$ , represents the lifetime due to SRH recombination, and  $\tau_{Aug}$  represents the lifetime due to Auger recombination. In general, a measurement of the bulk lifetime (assuming excellent surface passivation so  $S$  is very small if not zero) is a measure of each of these components. Figure 3.4 shows a plot of the effective lifetime of a n-type wafer that is doped with phosphorous and has a resistivity of  $4.58 \Omega - cm$ .

The lifetime versus minority carrier density plot shown in Figure 3.4, shows the effective lifetime (thick black line) with each of its components plotted. With perfect surface passivation in place ( $S = 0$ ), then this plot represents equation 3.13 where the effective lifetime is the same as the bulk lifetime. Notice how at lower carrier densities the lifetime is controlled by the SRH mechanism of recombination. At higher minority carrier densities the dominant mechanism becomes Auger recombination. The radiative recombination would only play an impact at lower carrier densities when SRH recombination is negligible. The plot was generated using the recombination calculator by PV Lighthouse [35]. When measuring the lifetime of a wafer with the WCT-120 lifetime tester, the effective lifetime plot in Figure 3.4, resembles what might be obtained from a measurement assuming the measured injection range was from  $1 \times 10^{12} \text{ cm}^{-3}$  to  $1 \times 10^{17} \text{ cm}^{-3}$ .

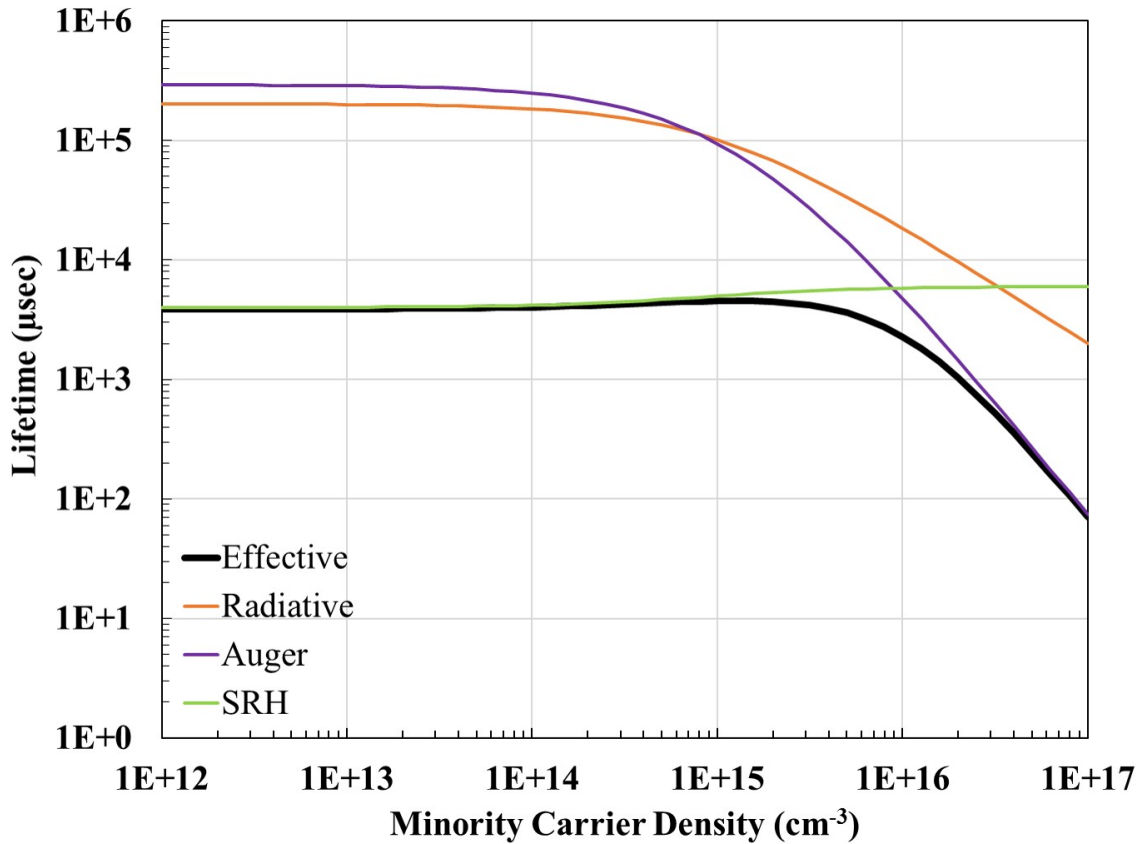


Figure 3.4: Lifetime versus minority carrier density for a n-type Si wafer showing how the bulk lifetime (effective) without surface recombination is made up of each recombination component.

### 3.1.2 Measurement of Emitter Saturation Current Density

If a bulk sample is prepared in such a way so as to introduce a diffusion, then the doping concentration throughout the sample is no longer uniform. This means that different recombination mechanisms are present in the diffused region and the wafer bulk. It is of value to quantify the level of recombination in the diffused regions where Auger processes are more dominant. For wafers with high bulk lifetime and sufficient surface passivation, Auger processes in the heavily doped areas will limit the  $V_{oc}$  and, thus, the efficiency [36]. Because of the importance of controlling recombination in the diffused regions, Kane and Swanson developed a method of measuring the recombination in 1985 [37].

A graphic describing the test structure used to determine the  $J_{0e}$ , or emitter saturation current density, is given in Figure 3.5, which shows a silicon sample having a high injection life-



time  $\tau_{hli}$  (where *hli* refers to high level injection) and two surfaces which have received diffusions, denoted by  $J_{0front}$  and  $J_{0back}$ . It should be noted that the terms  $J_{0front}$  and  $J_{0back}$  are representative of  $J_{0e}$ . In addition, the term  $\tau_{hli}$  describes the bulk lifetime of the wafer under high level injection conditions (which for an n-type wafer is satisfied by  $p \gg n_0$ , where  $p$  is the concentration of holes and  $n_0$  the concentration of electrons.)

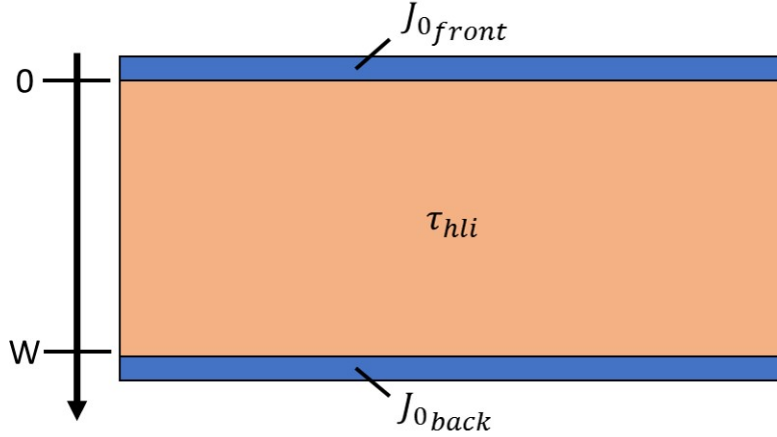


Figure 3.5: Graphic showing the test structure used to extract  $J_{0e}$  measurements. The arrow denotes the boundaries for the mathematical analysis of the structure.

By putting diffusions on both sides of a sample, the recombination current density ( $J_{0e}$ ) signal is doubled, thus increasing the signal to noise ratio of the measurement. To explain this characterization technique, the method of Kane and Swanson is followed [37]. In that paper, the authors assume that one wafer surface has no diffusion, but is passivated with an oxide having a surface recombination,  $s$ . In general though, the diffusions on both sides do not change how  $J_{0e}$  is extracted.

The sample is assumed to be measured under QSS conditions. In steady-state one can write that the spatially varying current density is equivalent to the net recombination less generation,

$$\frac{1}{q} \frac{dJ_e}{dx} = U - G \quad (3.14)$$

where  $q$  is the elementary charge ( $1.6 \times 10^{-19}$  C),  $J$  represents the current density of the generated minority carriers,  $U$  represents the net recombination rate in the wafer, and  $G$  rep-

resents a time dependent generation term. Equation 3.3. can be substituted in for  $U$  and  $G = dn/dt$  (representing a generation of carriers with time),

$$\frac{1}{q} \frac{dJ}{dx} = \frac{\Delta n}{\tau} - \frac{dn}{dt}. \quad (3.15)$$

Assuming that diffusion currents are the only currents that exist after generation has stopped, one can substitute  $J = qD \frac{dn}{dx}$  into equation 3.15 and up with,

$$\frac{dn}{dt} = \frac{\Delta n}{\tau} + D_{amb} \frac{d^2n}{dx^2} \quad (3.16)$$

According to Kane and Swanson boundary conditions can be applied at the bulk side of the  $J_0$  regions [37],

$$-J(W^-) = J_{0e} \frac{p(W^-)n(W^-) - n_i^2}{n_i^2} = -qD_{amb} \frac{dn}{dx} \Big|_{x=W^-}. \quad (3.17)$$

In equation 3.16, the current into the region marked by  $J(W^-)$  (the bulk side of  $J_{0back}$  in Figure 3.5), is equivalent to the ambipolar diffusivity of the carriers,  $D_{amb}$ , times the spatially varying carrier concentration  $\frac{dn}{dx}$  evaluated at bulk side of  $W$ . This is a diffusion current from the bulk into the diffused region. The term  $\frac{p(W^-)n(W^-) - n_i^2}{n_i^2}$ , represents the recombination,  $np$ , at the edge of the diffused region. This is similar to the derivation carried out in Chapter 2 following that of [28]. At the boundary where  $x = 0$  a similar condition can be derived (assuming the diffused regions to be symmetrical),

$$-J(0) = J_{0e} \frac{p(0)n(0) - n_i^2}{n_i^2} = -qD_{amb} \frac{dn}{dx} \Big|_{x=0}. \quad (3.18)$$

where all the terms have the same meaning as before, except that now generated carriers from the bulk are arriving at the  $x = 0$  interface. The bulk is assumed to be in high level injection meaning,  $p = n \gg n_i^2$ , such that,

$$-J(0) = J_{0e} \frac{n(0)^2}{n_i^2} \quad (3.19)$$

and

$$-J(W^-) = J_{0e} \frac{n(W^-)^2}{n_i^2}. \quad (3.20)$$

These boundary conditions are both non-linear with respect to the carrier concentration,  $n$ , and therefore a numerical solution is required. Kane and Swanson carried this out with the major conclusion being that when  $\sqrt{(D_{amb}\tau_{hli})} \gg W$ , then the carrier density becomes uniform after a few transit times across the wafer [37]. The diffused regions are very narrow and therefore any signal measured by an eddy current sensor in QSS mode (see previous sections), will be mostly from the base. The generation is in the bulk of the sample, but the carrier density becomes uniform throughout the sample with the respective recombination mechanisms in the bulk and diffused region of the sample under test. This allows for  $n(0) = n(W^-) = n_{avg}$ , which is the average carrier density sampled by the WCT-120. The total recombination is then written,

$$J_{rec} = -qW \frac{dn_{avg}}{dt} = qW \frac{n_{avg}}{\tau_{hli}} + 2J_{0e} \frac{n_{avg}^2}{n_i^2} \quad (3.21)$$

where  $q$  has its previous meaning,  $W$  is the sample thickness (less the diffused regions) as shown in Figure 3.5,  $n_{avg}$  is the sampled carrier density,  $\tau_{hli}$  is the lifetime of the bulk region under high injection. Again following Kane and Swanson, a solution to equation 3.21 is [37],

$$n_{avg}(t) = \frac{n_{avg}(0)e^{-t/\tau_{eff}}}{1 + c(1 - e^{-t/\tau_{eff}})} \quad (3.22)$$

with  $c$  being equal to,

$$c = \frac{J_{0e}\tau_{eff}n(0)_{avg}}{qWn_i^2} \quad (3.23)$$

and from equation 3.11,

$$\frac{1}{\tau_{eff}} = \frac{1}{\tau_{hli}} + \frac{s}{W}. \quad (3.24)$$

If the sample represented in Figure 3.5 has no diffusions such that  $J_{0e} = 0$ , then  $c = 0$ , and equation 3.22 reduces to,

$$n_{avg}(t) = n_{avg}(0)e^{-t/\tau_{eff}}. \quad (3.25)$$

However, in the case that  $J_{0e}$  is large (which should be the case since the bulk is in high level injection), then the reciprocal of the effective lifetime,  $\tau_{eff}$  can be plotted against the generated minority carrier density. The effective lifetime in this case will be,

$$\frac{1}{\tau_{eff}} = \frac{1}{\tau_{bulk}} + \frac{2J_{0e}n_{avg}}{qn_i^2W} \quad (3.26)$$

where  $\tau_{hli}$  in the previous equations has been replaced by  $\tau_{bulk}$  [29]. Following from equation 3.13,

$$\frac{1}{\tau_{eff}} = \frac{1}{\tau_{rad}} + \frac{1}{\tau_{SRH}} + \frac{1}{\tau_{Aug}} + \frac{2J_{0e}n_{avg}}{qn_i^2W} \quad (3.27)$$

It is reasonable to neglect the  $\tau_{rad}$  term as the radiative recombination term is very large in silicon (see Figure 3.4). Next, the auger recombination is subtracted out of the measured  $\tau_{eff}$ . Auger recombination is parameterized according to empirical models so that this is possible.

The term  $\frac{1}{\tau_{eff}} - \frac{1}{\tau_{Aug}}$  is then equal to,

$$\frac{1}{\tau_{eff}} - \frac{1}{\tau_{Aug}} = \frac{1}{\tau_{SRH}} + \frac{2J_{0e}n_{avg}}{qn_i^2W}. \quad (3.28)$$

Equation 3.28 is then plotted against the measured minority carrier density in the sample.

This produces a linear plot with the intercept being an estimate of the bulk lifetime in high level injection due to SRH recombination, and the slope of the line being related to  $J_{0e}$  and the material constants,  $q$ ,  $W$ , and  $n_i^2$  all maintaining their previous meanings. Figure 3.6 shows equation 3.28 plotted for a symmetrically diffused sample measured by the WCT-120 lifetime tester.

The slope of the fit line (black dots) in Figure 3.6 is found to be  $2 \times 10^{-13}$ , which when using

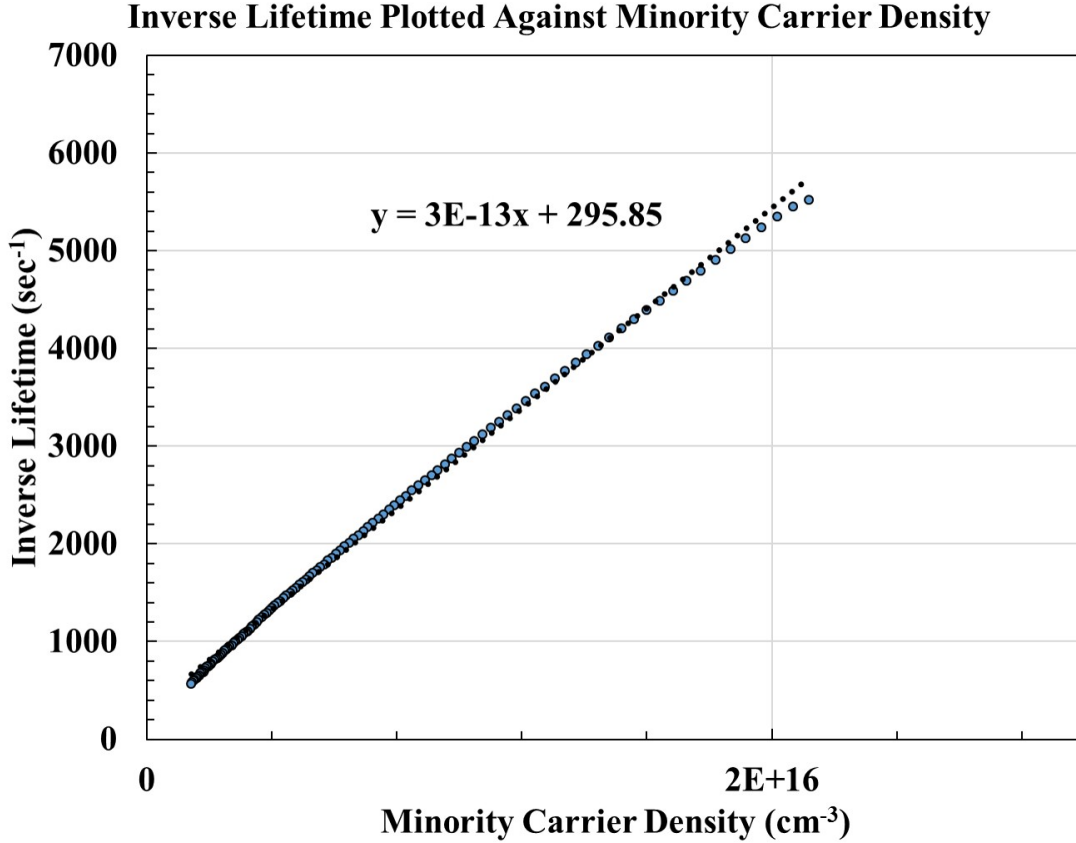


Figure 3.6: Inverse lifetime plot showing the linear output from a diffused sample as measured by the WCT-120. The slope is used to calculate the  $J_{0e}$ .

the equation,

$$slope = \frac{2J_{0e}}{qn_i^2W} \quad (3.29)$$

allows for determination of  $J_{0e}$ . The quantity  $n_{avg}$  in this case corresponds to the quantity  $N_{dop} + \Delta n$ , where  $N_{dop}$  is the doping density of the bulk of the sample being tested [29]. In this particular case, a wafer with a thickness of  $W = 0.0260$  cm and  $N_{dop}$  equal to  $1.3 \times 10^{14}$ , the calculated  $J_{0e} = 58.1$  fA/cm<sup>2</sup>. This calculation used a value of  $n_i = 9.65 \times 10^9$  cm<sup>-3</sup> as it has been determined by [38].

### 3.1.3 Calibration of the WCT-120

The measure of the photoconductance of a silicon sample under test is key to the operation of the WCT-120 lifetime tester. This is true whether a bulk lifetime is being sampled in the transient mode, or the if the QSS mode is used for extraction of  $J_{0e}$ . In order to extract an accurate photoconductance measurement, the tool requires calibration. Calibration is performed for both the photoconductor sensor and the RF sensor housed in the platform of the tool. The photoconductor for the WCT-120 is measured with a one-sun source and calibrated light sensor [29].

The RF sensor requires calibration in order to assure that the measured coil voltages are accurate for determining measured sheet resistances (photoconductances). In order to calibrate the RF sensor a set of NIST traceable calibration wafers are utilized. The wafers are 4" SEMI standard wafers possessing a range of sheet resistance values. The calibration procedure requires that at least 4 wafers are used. The wafer conductance is then plotted against the RF bridge voltage less the air voltage. From this plot, a quadratic fit is used to determined 3 calibration parameters, A, B, and C. The calibration curve can then be used to convert the measured voltages to the conductivity according to the equation [29],

$$\sigma = A(V - C)^2 + B(V - C) \quad (3.30)$$

where  $A$ ,  $B$ , and  $C$  are the aforementioned fit parameters,  $V$  is the measured voltage, and  $\sigma$  is the sampled conductivity. Changes in temperature can shift this calibration curve, due to changing properties of the coil. Therefore, the quantity  $V$  in equation 3.30 is the measured RF bridge voltage less an air voltage, the voltage of the coil with no sample in place. This normalizes the calibration curve to temperature shifts and makes data collection more robust. In addition, the measurement platform maintains 25°C as a temperature set point for making measurements.

For the work in this dissertation, the above calibration procedure had to be carried out with a plastic dish on the measurement platform. The reason for this is that a plastic dish ended up being the preferred method of containing the liquid quinhydrone-methanol, which was used

for surface passivation of the samples (to extract  $\tau_{bulk}$  and  $J_{0e}$ ). The plastic dish places a distance between where the sample would normally sit on the measurement platform. Therefore, it was deemed necessary to calibrate the RF bridge voltages with the plastic dish in place, so that the measured voltages took into account the extra distance. The procedure for calibrating with the dish in place was no different than the standard procedure, other than, the calibration wafers were placed in the dish and the procedure was carried out. This produced a different set of fit parameters, A, B, and C, that were then stored for use any time the plastic dish was used with a measurement.

### 3.2 The Four Point Probe Method

The Four Point Probe method uses four probes, two voltage probes and two current probes, to measure the sheet resistance of a semiconductor material. Figure 3.7 shows the setup used to measure the sheet resistance.

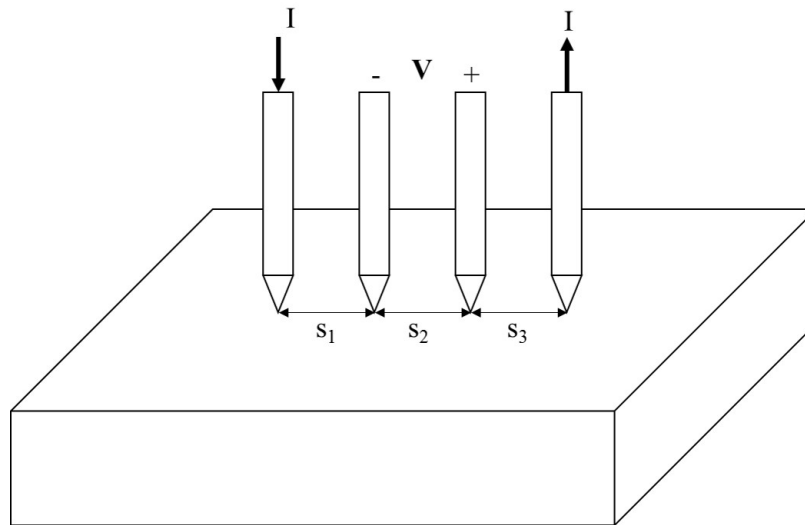


Figure 3.7: Image showing the current and voltage probes used in for a four point probe measurement

A good overview and derivation of the four point probe operation is outlined in [39]. The relevant equation that comes from the four point probe method derivation is:

$$\rho = 2\pi s FV/I \tag{3.31}$$

where  $s$  represents the spacing of the probes,  $F$  is a geometrical correction factor necessary for finite geometry, and the voltage and current are as measured. This equation works well for uniformly doped semiconductor samples. The value in using four probes is best explained by referring to the circuit schematic of Figure 3.8.

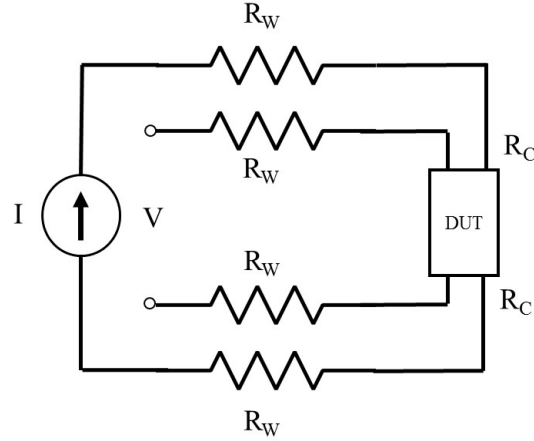


Figure 3.8: Circuit schematic explaining why a four point method is preferred over a two point probe method

Typically, a measurement might involve the use of just two probes, but the circuit schematic of Figure 3.8 shows 2 contacts from the current source as well as two from the voltage source. There are a total of four connections to the DUT (device under test). There are also four additional  $R_w$  or wire resistances. The voltage measurement features a very high impedance source, and therefore, the current in the voltage leads is negligible. This allows for the  $R_w$  and  $R_c$  values to be neglected and gives us a true measurement of the voltage of the DUT. The series current in the outer loop is all that is of interest and is not altered due to voltage drops. As mentioned, an adjustment is necessary to properly measure the sheet values of a non-uniform layer. An example of a non-uniform layer is that of a boron diffusion profile. For a uniformly doped semiconductor samples we obtain the sheet resistance from

$$R_{sh} = \frac{\rho}{t} \tag{3.32}$$

where  $\rho$  is equivalent to the sample resistivity and  $t$  is the sample thickness. The change in



this equation for non-uniformly doped regions comes from a change in the  $\rho$ .  $\rho$  now varies with the non-uniform doping profile resulting in,

$$R_{sh} = \frac{1}{\rho dx} \quad (3.33)$$

where  $t$  represents the thickness of the non-uniformly doped area and  $\rho$  is the resistivity at each slice of the sample  $dx$ . The sheet resistance is a useful specification for device designs, but does not quite help in describing the overall shape of a doping profile that would occur at the surface such as that that would be in a solar cell. For that methods capable of profiling the doping level with depth are necessary.

### 3.3 Electrochemical Capacitance Voltage Profiling

Electrochemical Capacitance Voltage (ECV) profiling is a method that uses a chemical electrolyte that simultaneously forms a junction with a semiconductor surface while also having the ability to etch away the semiconductor. The junction formed can be described using as a Schottky barrier and the standard application of depletion region analysis allows for the extraction of doping concentration via the measured capacitance value. This section describes how the ECV measurement is performed and how doping concentration versus depth information can be obtained. The discussion focuses on Si as this is pertinent to this dissertation. For an ECV measurement, modern tool sets equipped with pumps and a system of etch resistance tubes guide a liquid solution (electrolyte) to a silicon surface. Referring to Figure 3.9, the electrolyte is contained within a sealing ring that provides a leak proof, or nearly leak proof, seal against the silicon surface. The electrolyte contains ions and when a positive voltage is applied to the electrolyte, positive ions are attracted to the electrolyte/silicon interface. The buildup of holes at the surface is a familiar phenomenon as when a metal is placed in contact with the silicon. As seen in Figure 3.10, the positive ions at the electrolyte/silicon interface act to “deplete” or push away majority carrier holes in the p-type Si. The case of p-type silicon is discussed as it is most relevant to the boron doped silicon studied in this dissertation.

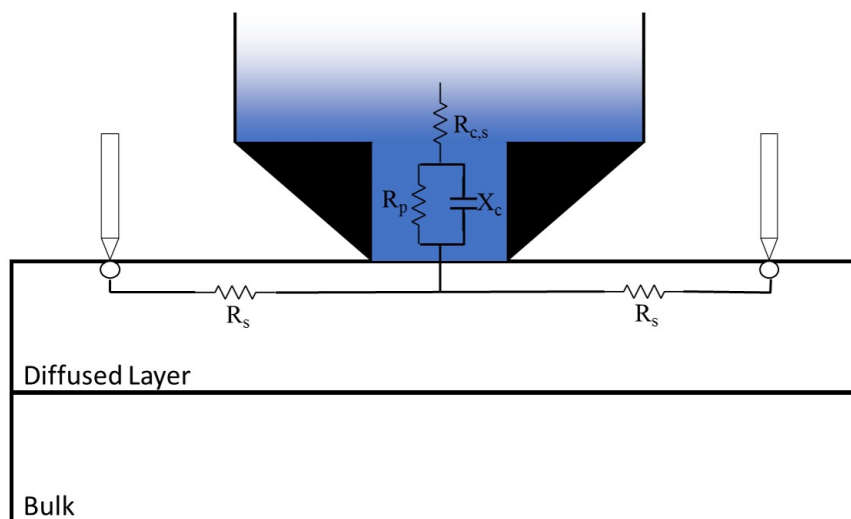


Figure 3.9: Image showing a sealing ring containing electrolyte in contact with a diffused layer on top of a wafer bulk. The system can be modeled with a standard circuit.

With the electrolyte in contact with the Si, it is useful to model the system using a circuit as shown in Figure 3.9. Though pictured is a parallel model, the circuit can be changed to a series model or a 3-term model. Additional resistances might be present as well, especially true of samples where a layer exists above the substrate. This is shown in Figure 3.9 as a diffused layer, with series resistance,  $R_s$ , leading to two metal contact probes. The metal probes allow contact to the semiconductor surface for extraction of current density (JV) and capacitance-voltage (CV) parameters.

Typically, a JV measurement is performed to verify the contact quality of the probes. The JV curve resembles a diode curve. It is from this curve that a suitable value for the etch voltage can be obtained. Following JV measurement, one then can collect a CV curve. The CV curve,  $1/C^2$  curve, and dissipation factor curve are all plotted. If the sample conforms to a Schottky diode, then plotted CV curves for each of the 3 mentioned circuit models will converge together. The  $1/C^2$  will be linear in the region of voltage where depletion is established. It is in this region that one selects a voltage to be used as the measurement voltage.

Silicon is a bit of an oddity when it comes to the ECV measurement. One reason for this is that the dissolution valency is not well defined [40]. The dissolution valency refers to the number of ions participating in the etch process. In addition, hydrogen bubbles can form and ob-

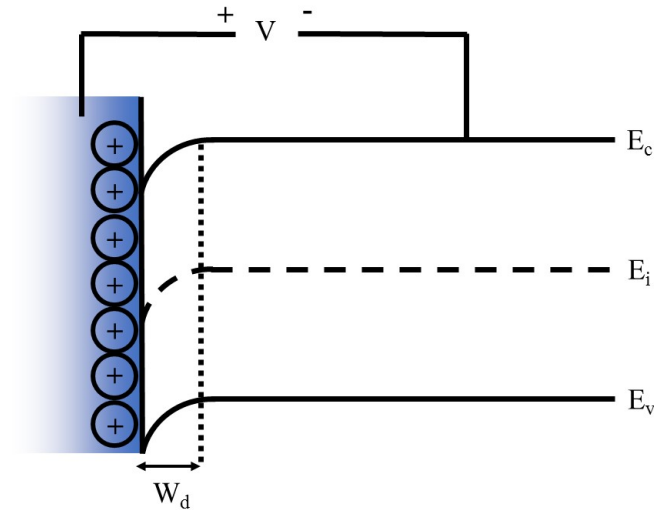


Figure 3.10: A conceptual band structure diagram showing how the positive ions in the electrolyte, deplete the semiconductor. The capacitance of this depletion area of with  $W_d$  is measured for doping extraction.

secure measurement. The hydrogen bubble problem is resolved by agitating the solution. Another interesting aspect about measuring silicon is that it requires a different etching mechanisms as compared to its direct band gap counterparts [41]. The method, known as pulse anodization, is shown in Figure 3.11. Essentially, a high etch current value is applied to the silicon that causes oxidation. The growth of the oxide exponentially reduces the current as the oxide thickness grows. After some pre-determined current or time limit, the current is turned off, and the electrolyte solution is allowed to circulate and remove the silicon oxide. This process can lead to etch times of about  $1 \mu m/\text{hour}$ . It also tends to cause an underestimate of profile depths which is resolved by post-processing the data.

ECV is useful in that it is a relatively fast and inexpensive way to obtain doping profiles, especially of boron doping, in silicon. There are disadvantages in that certain surface conditions can cause deviations from the ideal Schottky behavior, which sometimes compromises the CV data, and therefore makes profile extraction erroneous or impossible altogether. In addition, the measurement voltage is dependent upon the doping concentration in Si. This can place limits on the applicable resolution that can make measurement of lowly doped samples difficult.

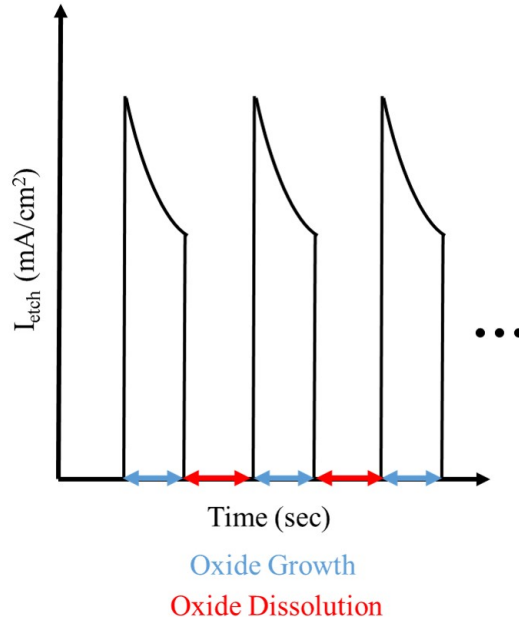


Figure 3.11: Graphical illustration of Pulsed Anodization concept. The blue horizontal arrows represent phase for silicon oxide growth. The red horizontal arrows represent a phase where the grown oxide is etched away.

### 3.4 Spreading Resistance Profiling

Spreading Resistance Profiling (SRP) is a method of obtaining dopant information versus depth from a sample by measuring the spreading resistance of two probes. The depth measurement is possible because the sample is beveled in a way so as to produce a steep angle from the surface as shown in Figure 3.12.

The spreading resistance term comes from the spreading of current from the probe tip as shown in Figure 3.12. The equation that governs measurement of the spreading resistance is,

$$R = 2R_p + 2R_c + 2R_{sp} \quad (3.34)$$

where  $R_p$  is the resistance of the probe,  $R_c$  is the contact resistance the probe makes against the sample, and  $R_{sp}$  is the spreading resistance. The multiplier of 2 comes from the fact that there are 2 probes. The  $R_{sp}$  has been determined by comparison to FPP measurements [42]

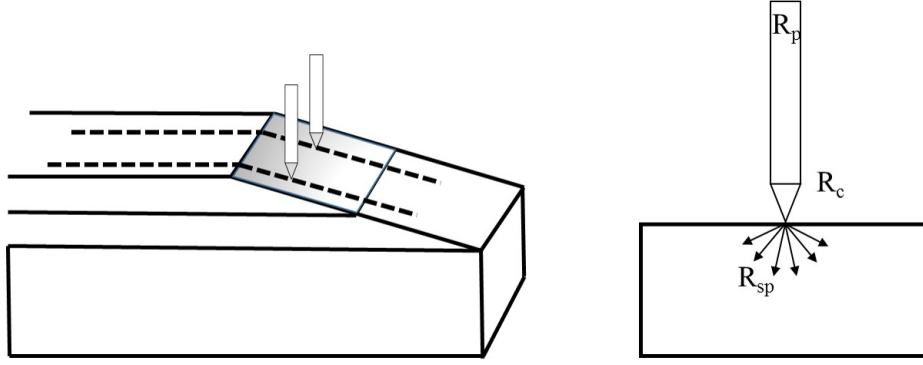


Figure 3.12: (Left) Diagram showing how a sample is beveled and two probes are placed on the bevel for measurement. The dashed lines represents the path taken by the probes to measure the spreading resistance. (Right) A diagram illustrating the resistances present in one probe.

which has resulted in,

$$R_{sp} = \frac{\rho}{4r} \quad (3.35)$$

where  $r$  is the tip radius, and  $\rho$  is the resistivity of the underlying material. The two probes are scanned down the bevel and measurements are made at each point. The resistance is then compared to calibrated mobility data to determine doping concentrations. The precise control of the probe scanning and angle of bevel allow for possible depth resolutions of 5-10 nm. The SRP data provided in this dissertation comes from Solecon Laboratories. More details on the exact methods use to measure the spreading resistance and apply post-processing analytics to the data to obtain doping profiles can be found in [43].

### 3.5 Light and Dark JV Characterization

The most common technique to characterize solar cells, of any type, is that of current-voltage or, JV, characterization. Though the technique is referred to as a "current"-voltage, the term J is used as it is more useful to speak of a solar cell's current density. This is because different solar cells can be of different sizes and the current density allows for a more true comparison. Here, an overview of the measurement system used in this dissertation is given. The reader should direct their attention to Figure 3.13 for the remainder of this section.

In Figure 3.13 several components are shown. The most important is the black trapezoidal

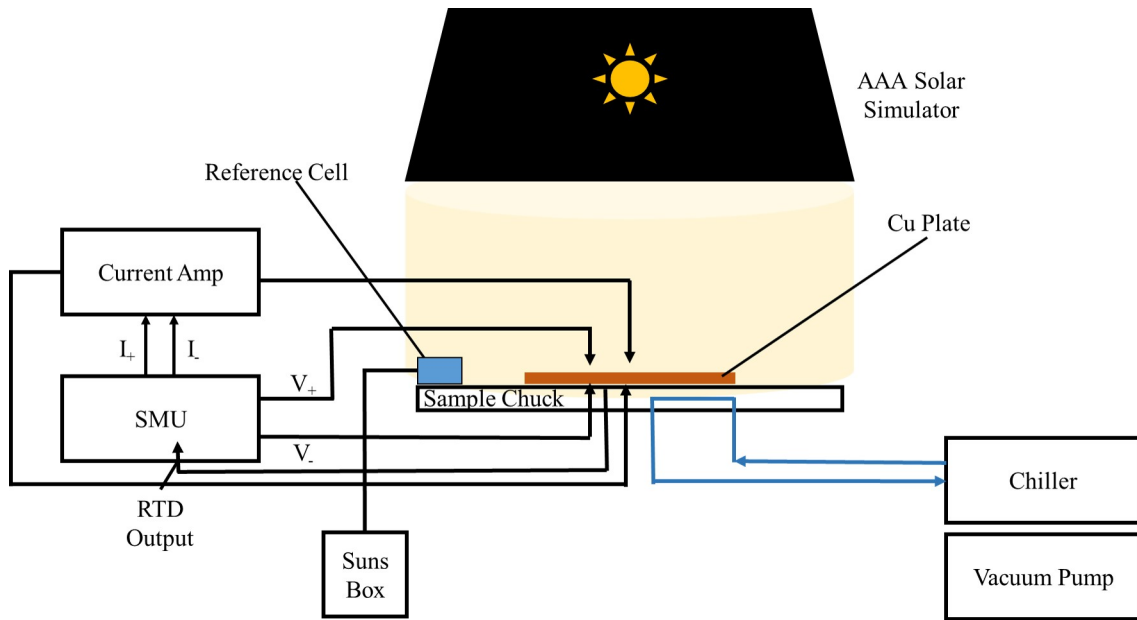


Figure 3.13: Block diagram overview of a JV measurement system complete with solar simulator, chiller, vacuum pump, and SMU for sourcing and measuring current and voltage.

box with a sun symbol in the middle. This is meant to represent a solar simulator. Solar simulators use a specially designed Xenon bulb with a set of optical components to match the optical output of the simulator to that of the actual sun. This light is cast upon a sample stage or “chuck” on top of which rests two additional components, a reference cell and a copper (Cu) plate. The reference cell is calibrated to maintain a specific cell output for various illumination conditions. This is converted to a Sun number ranging from 0 (no output, dark) to 1 (nominal intensity of the sun). The Cu plate serves as one contact for the back of the cell and is actually sub-divided into two electrically distinct parts, one for a current contact and the other for a voltage contact.

A chiller circulates cool water through the sample chuck to remove heat. This allows for the system to maintain a constant temperature. The properties of a cell, namely the  $V_{oc}$ , can vary depending upon the temperature. The accuracy of the temperature in this case is about  $0.1^\circ C$ . A vacuum pump is also used to gently hold the sample against the sample chuck. Finally, a source measure unit (SMU) is used to both supply and measure current and voltage. To properly measure the device characteristics of the solar cell, a 4-wire setup is used. In

this setup there are two voltage contacts, and two current contacts. The voltage connection to the front side of the cell  $V_+$  is sometimes called a “sense” voltage. Its purpose is to only sample the voltage by making contact to top busbar or gridline of the solar cell. A current contact,  $I_+$  is also made to the top of the device. For small cells, typically one current contact is enough, however, for industrial size devices, it is necessary to sample the current along several contact points of the busbar. This minimizes voltage drops that might otherwise impair the measurement. The voltage and current contacts on the backside of the cell act as return paths.

To carry out a measurement in the dark, a shutter is pulled over the simulator’s output. Then the SMU supplies a voltage to the device and the resulting current flow is measured. For a light measurement, the shutter is opened. This time the resulting current produced from the absorption of light in the device is measured at each voltage point. This produces a set of curves known as the dark and light JV curves.

The dark JV curve can give information about ideality factor and recombination mechanisms in the device. The light JV curve can yield information regarding the cell efficiency, open circuit voltage, short circuit current, maximum current, and maximum voltage. The fill factor (FF) can also be determined from the JV curve.

### **3.6 IQE/EQE**

Solar cells must respond to a spectrum of light from the sun that contains multiple different wavelengths of radiation. This includes UV components below 360 nm and even some infrared up to 1100 nm (or about the bandgap of Si). To assess how individual wavelength components of the spectrum are absorbed by the solar cell, a technique known as quantum efficiency (QE) can be used. There are two types of QE, internal quantum efficiency (IQE) and external quantum efficiency (EQE). Internal quantum efficiency takes in to account reflections that occur at the front side of the device, which it discriminates against and does not consider to be a loss. EQE assumes that this front reflection is a loss. It is typical for IQE to be higher than EQE.

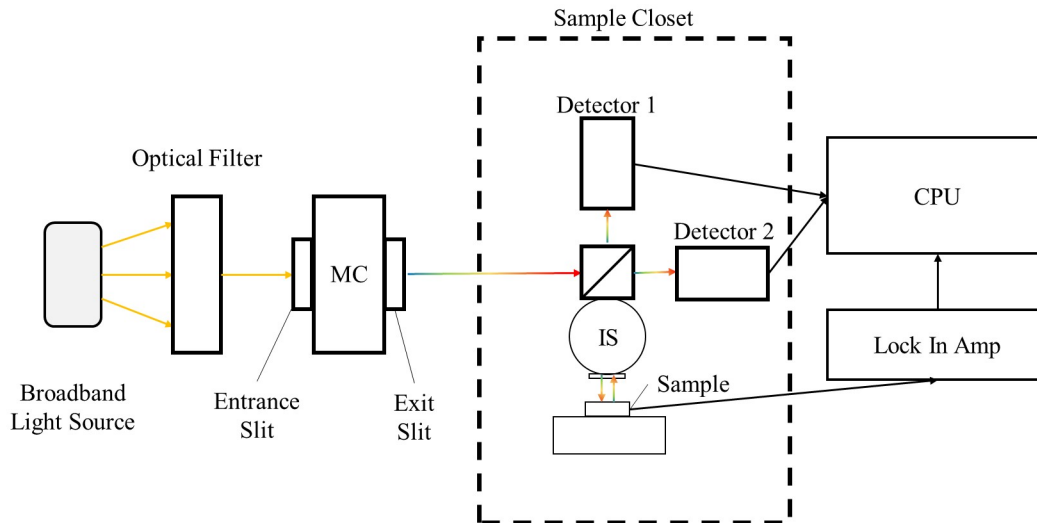


Figure 3.14: Block diagram showing relevant components of a commercial IQE/EQE system.

The system used to measure IQE/EQE is shown as a block diagram in Figure 3.14. A broadband light source, such as a tungsten-halogen lamp is used. The light output from this lamp goes through an optical filter wheel that is connected to a lock-in amplifier. The filter wheel chops up the light output at a specified frequency that the lock-in amplifier "locks on to". This helps to reduce noise in the measurement. The output from the filter wheel goes to a monochromator (MC). Inside the MC is a diffraction grating mounted on a motorized turret. The grating rotates to produce different outputs of light. This system can produce 320 nm to 1100 nm light output. The single wavelength light output then travels to a network of detectors, first entering an optical component that splits up the intensity of the output beam and directs it downward to a sample. Light is either absorbed or reflected from the surface of the sample, which then is directed to the detector arms. Detector 1 measures the reflected output from the device and detector 2 measures beam output from the source signal. In addition, an integrating sphere (IS) that contains a lambertian surface on the inside is used to gather all diffuse reflectance. The IS allows for the IQE to be measured, as sample surfaces can be optically rough, such that scattering prevents the reflected light from traveling in a direct path back to the detectors.

In a typical scan, the user sets the wavelength range of interest. The system then scans through



the wavelength range at intervals specified by a user set resolution (this system can go as low as 10 nm). A CPU monitors the cell output and beam output from the detectors and formulates the EQE. It can then use the gathered reflectance information to calculate the IQE.

### **3.7 Summary**

This chapter reviewed all of the main experimental methods that were required to carry out the research in this dissertation. Photoconductance spectroscopy was introduced, and reviewed in detail as it is this method that allows for measurement of the emitter recombination current density,  $J_{0e}$ . In addition, dopant profiling methods ECV and SRP were covered. All of these methods were used to characterize and design the experiments carried out in Chapters 4,5, and 6.

## Chapter 4

### Quinhydrone-Methanol Surface Passivation of Bulk n-type Silicon

For this dissertation, there were two goals in working with Quinhydrone-Methanol (QM). One goal was to demonstrate that the surface of silicon could be passivated to a high degree. The second goal was to develop a method for evaluating the lifetime of the silicon wafer samples used in this dissertation. The effective bulk lifetime of a material can be used as a purity gauge and is the first step in determining whether or not a material is suitable for recombination current density testing. The characterization necessary to measure the bulk lifetime also reveals information regarding the upper bound on the surface recombination velocity that the QM provides to the silicon sample. In performing the experiments to validate the quality of the bulk silicon and ability for QM to passivate the silicon, an additional study was undertaken regarding the stability of the passivation and that is included here for discussion as well.

#### 4.1 Quinhydrone-Methanol Passivation

Liquid solutions for surface passivation of silicon substrates have been shown to provide excellent passivation, albeit, for short durations of time. To that end, it was necessary to review the literature to determine in what ways QM had been used and what characteristics it was known to have. The following is a review of the current state of knowledge of QM passivation applied to silicon wafers.

QM is an organic compound that is a 1:1 combination of hydroquinone and benzoquinone. The first published use of QM solution to passivate silicon wafers was given by Takato et. al. in 2003 [44]. In this work, the authors investigated the stability of passivation on various bulk substrates and compared it to another liquid passivant, iodine-ethanol (IE). The next known study, again applied to bulk wafers, came from Chhabra et. al. [45]. This work involved a study on high resistivity float-zone (FZ) n-type wafers and lower resistivity p-type Czochralski (Cz) wafers. Bulk lifetimes as high as 3.3 msec (sampled at  $1 \times 10^{15} \text{ cm}^{-3}$  excess carriers) were measured. In addition, the stability of QM passivation was tested. Samples were placed in a solution of QM, contained in a plastic bag, and measured using a WCT-120

lifetime tester (as described in Chapter 2). Samples were then removed from the QM solution and re-measured over a time period of several days. The passivating capability of the QM was found to degrade significantly, with the sample having measured 3.3 msec, reducing to right around 0.8 msec after 3 days of degradation. This degradation over time was attributed to the oxidation of the silicon with oxygen atoms assuming to break the bond between the quinhydrone (QHY) molecule and the silicon surface. Researchers have shown that the active component in the passivation process is linked to benzoquinone [46]. Still others, have shown that the passivation quality is so good, that it can yield near perfect Schottky-Mott behavior between a Hg contact and a Si surface [47]. That is the junction formed between the Hg and Si produces minimal band-bending near the surface providing an ohmic contact. Despite all of QM benefits, it does have some drawbacks. For instance, the passivation does not last forever, and the longest time it has actively passivated has been published to be less than 2000 minutes [48]. In addition, the repeatability of the measurement has been called into question, but this seems to be overcome by careful and rigorous cleaning procedures [49]. The results provided in this section work to confirm those that exist in the literature in terms of providing high quality surface passivation to silicon surfaces.

## 4.2 Bulk Lifetime Measurements and Surface Recombination Velocity

In order to passivate silicon substrates with QM it was necessary to first develop a systematic method to do so. This involved discovering that a controlled removal of a layer of the silicon where saw damage exists was needed. The saw damage is a 5-10  $\mu m$  thick region at the surfaces of as-sawn silicon. As-sawn silicon refers to that silicon material that has had no surface processing done to it. Typically silicon wafers are etched and polished before being purchased. In this work, the material that was used was all as-sawn material. In addition, because QM is a liquid solution, it was necessary to work out the best containment option for making measurements. Finally it was required to take multiple lifetime measurements to observe trends that relate back to the objectives necessary for qualifying that QM can work to passivate silicon.

### 4.2.1 Saw Damage Removal

Most solar grade silicon is manufactured in a multiple step process that involves mining of silicon oxide (quartz), extracting of the silicon, and refinement of the silicon to electronic quality [50]. It is during refinement that the silicon is pulled into a large crystal boule in the Cz process. To obtain single wafers, a diamond wire saw is used to dice out wafers of a particular thickness from the boule. In doing so, one can obtain wafers, but not without a sub-surface volume that is populated by micro-cracks generated during the sawing process. An image visualizing this idea is shown in Figure 4.1.

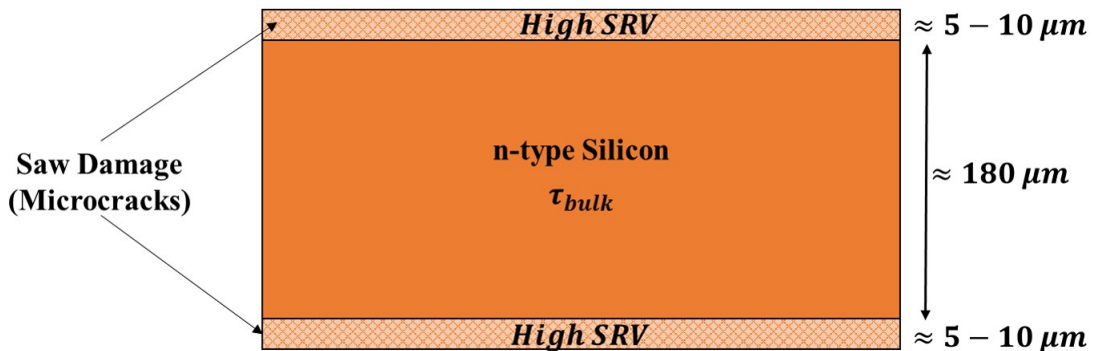


Figure 4.1: Illustration of bulk silicon with saw damage acting as a high SRV layer on either side fo the wafer.

This surface layer of “saw damage” is typically on the order of  $5-10 \mu m$  thick and acts to inhibit passivation of the silicon surface [50]. In order to remove such regions in the wafer, wet chemical etching is typically used. In a solar cell manufacturing process, this etching step also forms random pyramids at the surface that act to reduce reflections improving the optical characteristics of the cell. However, in this work, an isotropic etch was sought after in order to keep the surface as planar as was practically possible. A planar surface provides for simpler experimental observations and results. A review of the literature showed a viable candidate for such an etch process was a combination of hydrofluoric and nitric acid with water [51]. Further review revealed that the combination of hydroflouric and nitric acid was a standard method used to produce a “shiny etch” effect, named as it produces a mirror like wafer surface [32]. This type of etch is standard in solar research to produce a planar surface for passi-

vation measurement and experiment.

It was not immediately obvious from the literature what ratios of HF and HNO<sub>3</sub> would produce the desired etch rate of silicon. In initial trials, silicon samples that were 200 μm thick were etched completely in a few minutes. The etch solution would quickly go from a clear solution to a deep yellow to deep red solution and produce a thick cloud of fumes. Due to safety concerns, this etch process was not repeated and the literature was again consulted to determine the best way to remove saw damage from the silicon wafer.

The addition of acetic acid in place of H<sub>2</sub>O in a HF+HNO<sub>3</sub> solution prevents the formation of NO<sub>3</sub> or NO<sub>2</sub> and also acts to wet the silicon surface for a more uniform etch [52]. It was then decided to include acetic acid in trial etches to determine the etch rate of silicon. The combination of HF, HNO<sub>3</sub>, and CH<sub>3</sub>COOH is termed an HNA etch. An etching trial was carried out with a mixture ratio of 10:1:2 HNO<sub>3</sub>:HF:CH<sub>3</sub>COOH with the results shown in Figure 4.2. The approximate etch rate of the solution on Cz silicon was determined by taking the slope of the fit lines shown in Figure 4.2. The etch rate was found to be about 4.4 μm/min. to 5.12 μm/min. This rate was deemed satisfactory for a saw damage etch as it removes about 20 μm of material in about 3.9 to 4.5 minutes.

Another viable etching solution was trialed which involved the use of tetramethyl ammonium hydroxide (TMAH). This was determined to be another etchant of silicon after reviewing the work of Grant et. al. [53]. In that work, samples were submitted to a variety of chemical solutions including TMAH, HF:HNO<sub>3</sub> (combination of hydrofluoric and nitric acid), RCA-2 (a combination of water, hydrogen peroxide, and hydrochloric acid), HNO<sub>3</sub> (nitric acid), RCA-1 (traditionally a combination of water and ammonium hydroxide), and H<sub>2</sub>SO<sub>4</sub> (sulfuric acid). The samples were then immersed in HF acid following a special procedure [54]. Measured of the wafer lifetime were taken using the WCT-120 lifetime tester. It was found that a TMAH etch acted to provide the best chemical treatment to the surface of the silicon to enable high passivation in HF. This better passivation was attributed to the fact that the TMAH etching turns a <100> surface partially into a <111> surface through some slight texturing. The <111> silicon surface has a higher number of atoms than a <100> surface, and therefore, it

### 10:1:2 HNA Etch from Park et. al. on Cz Silicon

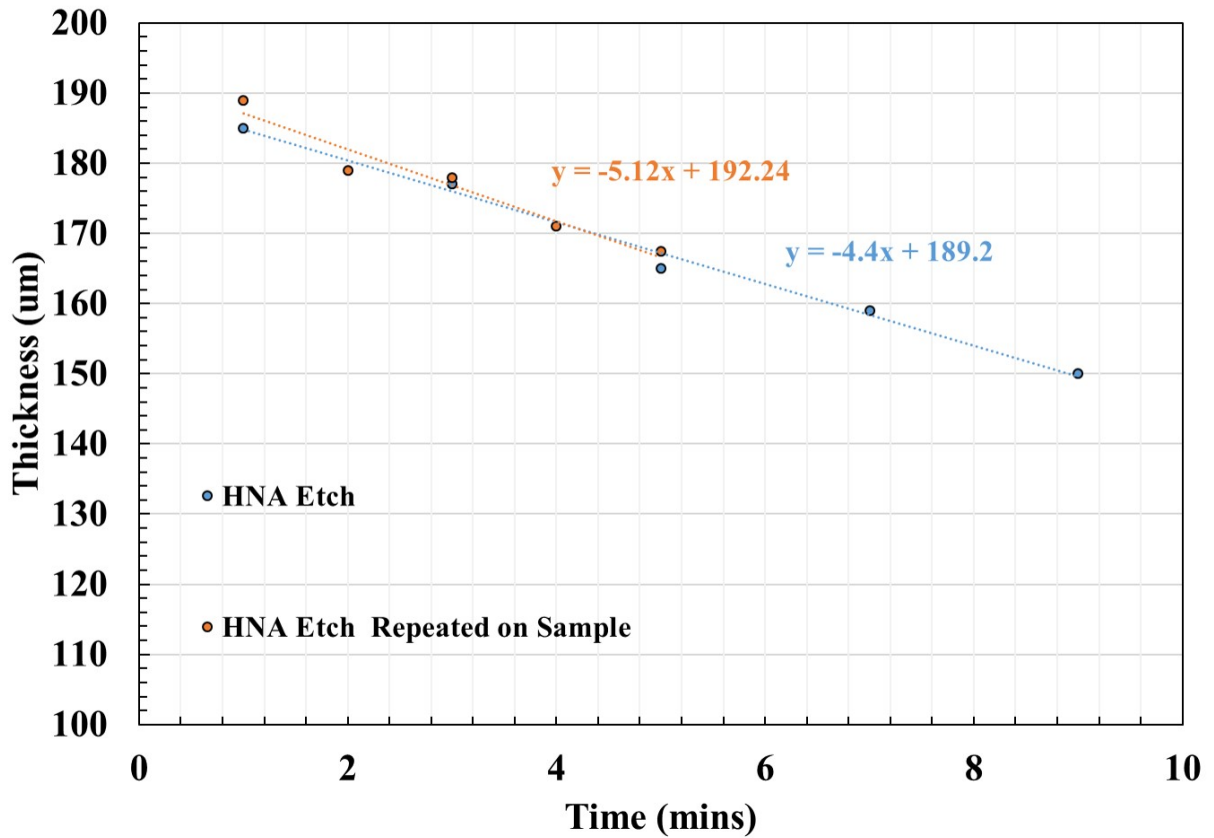


Figure 4.2: Thickness of a silicon wafer sample versus time showing linear etch rate of 10:1:2 HNA solution.

was concluded that there is more surface area for hydrogen (from the HF) to stick to. It was determined that the TMAH could provide an etch rate dependent on the temperature of the etch solution.

The data in Figure 4.3 reveal the effects that saw damage can have on a wafer surface.

The data is shown for FZ material that was received in an "as-sawn" condition and no processing was performed on it before placing it in QM solution. Next, the sample was subjected to a Piranha solution, which does etch the surface but only a few nanometers deep at most [55]. Almost no change in the measured lifetime was observed, indicative of the fact that the surface had high recombination given the flat measurement profile. Finally, after a 90°C 25% TMAH etch the lifetime of the sample is measured to be near 6 msec at  $1 \times 10^{15} \text{ cm}^{-3}$  revealing that the saw damage had been removed from the sample. Without saw damage in place, the

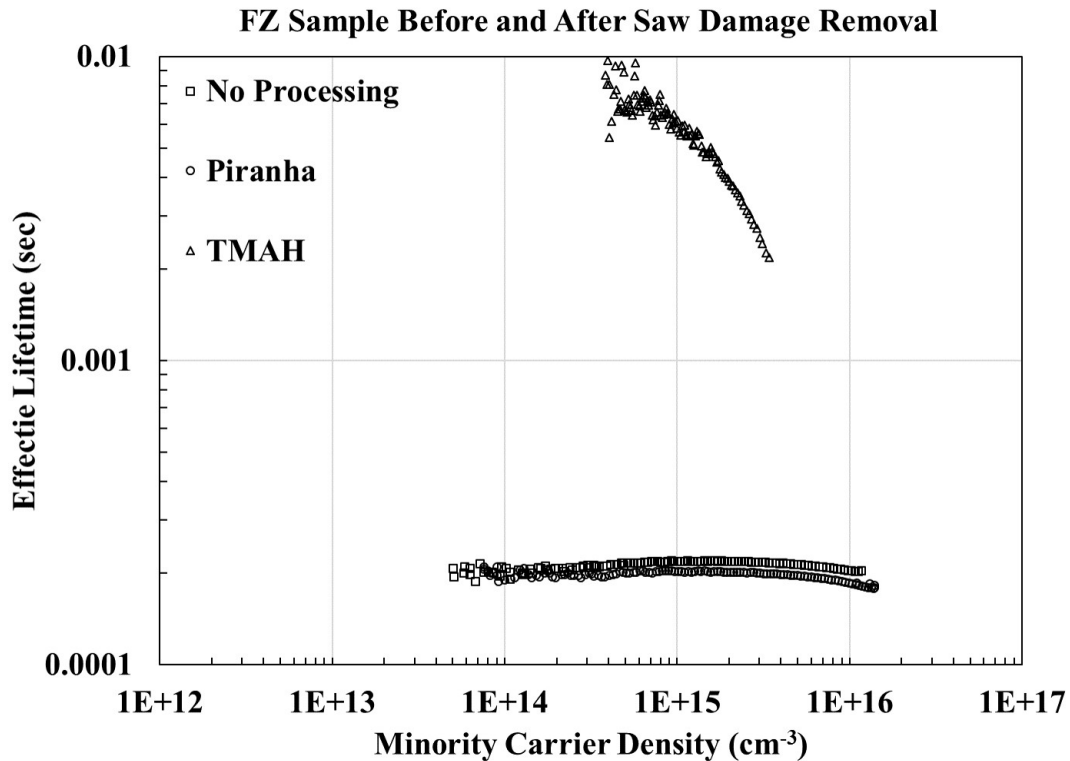


Figure 4.3: Lifetime measured on same sample with no processing, after a Piranha clean process, and finally after etch in 90°C 25% TMAH.

QM is able to passivate the surface of the silicon revealing the characteristics of its lifetime curve without surface SRH effects.

#### 4.2.2 Containment

An issue with choosing to use liquid passivation for silicon wafers is a means by which to contain the liquid. Two obvious options for containment are chemically resistant plastic bags or a plastic dish [45, 53]. Plastic bags have the advantage being thin enough so as not to place a large distance between the sample and measurement platform of the WCT-120 lifetime tool. This distance is important as the larger the distance, the larger the separation between the measurement coil inside the platform, thus weakening the eddy current signal that develops in the sample. Plastic dishes require recalibration of the WCT-120 to take into account the increased separation between the sample under test and the measurement coil. Some key disadvantage to using plastic bags were found to be air bubbles in solution and the limitation of

how much solution can be placed in the bag. This is best seen by examining Figure 4.4, which shows the minority carrier density (MCD) vs. lifetime plot for two Cz silicon samples having undergone the same cleaning processes and etch treatments. The only difference between the two measurements is that one sample was measured in a plastic bag and the other was measured in a plastic dish placed on top of the measurement platform.

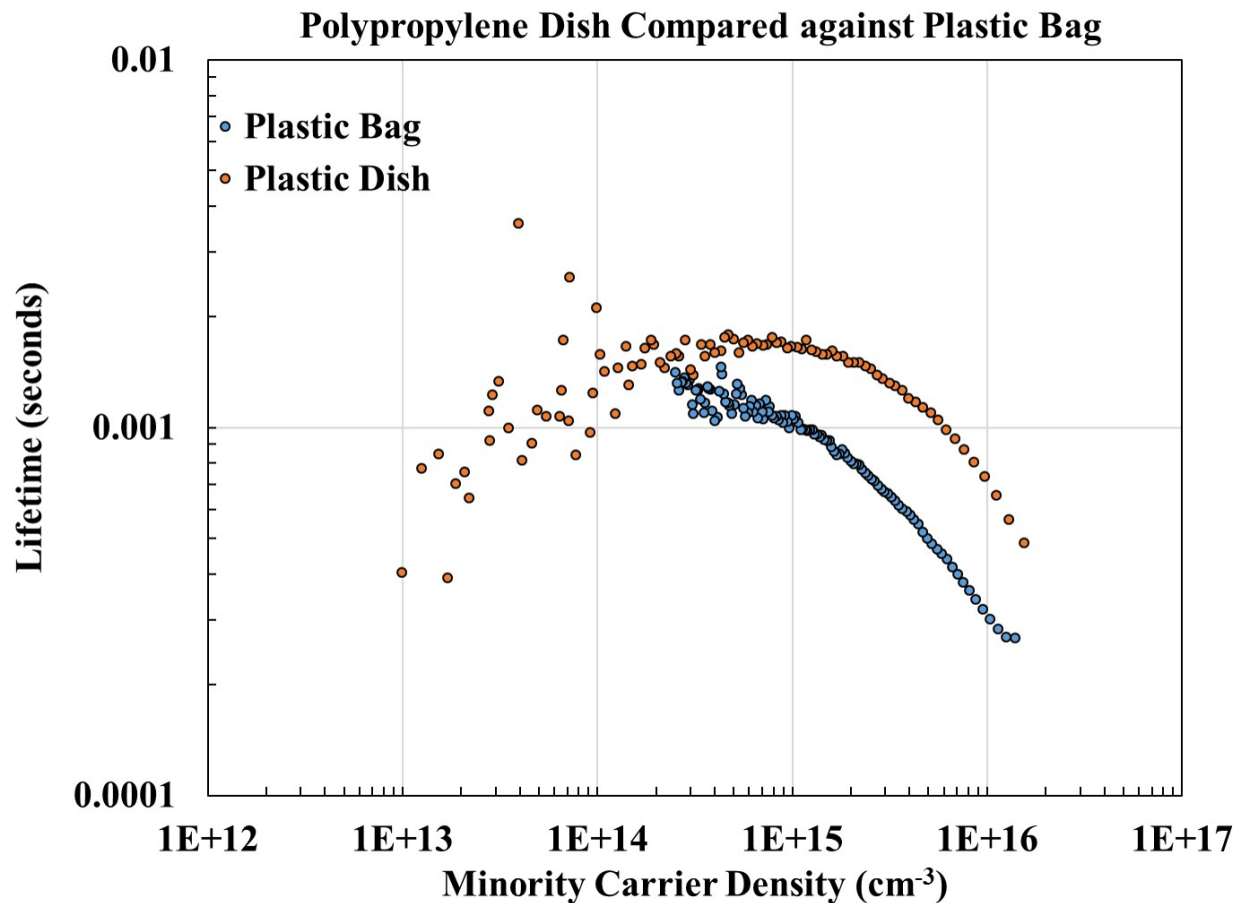


Figure 4.4: Comparison of transient photoconductance output between two samples having been passivated in QM but with two different containment methods.

Of the two curves in Figure 4.4, the curve with the higher MCD range was measured in the plastic dish. The curve with the shorter MCD range was measured in a plastic bag. This plot is representative of the typical results that were obtained when using a plastic bag for containment or a plastic dish. Note that the plastic dish has a higher lifetime over the entire MCD range and its MCD range is longer, giving more information about lifetime over the entire injection level.



In addition to the lifetime results, the method involving the use of a plastic bag to contain the liquid QM and sample on the measurement platform was unreliable. It was often that the bag would leak out the top or the bag would be punctured by the edge of the silicon, resulting in a failed measurement. Therefore, for the sake of measurement reliability and consistency, the standard method became to contain the sample and liquid passivation in a polypropylene dish that would sit on top of the measurement platform. This was possible through re-calibration of the constants used in the fitting routine in the WCT-120 lifetime tool, which was covered in Chapter 2.

### 4.2.3 Lifetime Data and Discussion

One of the main goals in working with QM was to make sure that it was viable as surface passivation. This could be done through use of the WCT-120 lifetime measurement tool. Samples that are poorly passivated have recombination dominated by the surface. In such a case, a flat lifetime curve is obtained. A qualitative indication that a sample is passivated is that the lifetime curve exhibits curvature that approaches the intrinsic recombination limits (radiative and Auger) of that sample. The degree to which a sample was passivated (determination of the surface recombination velocity (SRV)) was harder to determine, but was qualitatively determined and an upper bound to the SRV was calculated.

During the course of work in this dissertation 18 sets of lifetime measurements were performed on bulk silicon samples. Though the focus of this dissertation was on determining the effects of hydrogenating a boron diffusion, it was necessary to validate the surface passivation method, QM, on bulk silicon. The reason for this is two fold, previous research exists on the topic of passivating bulk Si with QM and it removes the added complexity of the boron diffusion from the sample. This allows for easier interpretation of the results. Table 4.1 provides a summary of the types of sample that were measured, the nominal doping ranges of such samples, the MCD at which the lifetime value was sampled, the maximum average effective lifetime value, and a calculated upper bound to the surface recombination velocity (SRV),  $SRV_{UB}$ .

Summary of Sample Types				
Type	Doping (cm <sup>-3</sup> )	MCD	Max. Avg. $\tau_{eff}$ (msec)	$SRV_{UB}$ (cm/sec)
FZ	1.11 - $1.48 \times 10^{14}$	$2 \times 10^{15}$	4.424	3.16
Cz-1	1.55 - $5 \times 10^{15}$	$2 \times 10^{15}$	1.511	5.79
Cz-2	$4.5 \times 10^{14} - 5 \times 10^{15}$	$1 \times 10^{15}$	0.311	24.12
Cz-3	$4.5 \times 10^{14} - 5 \times 10^{15}$	$1 \times 10^{15}$	0.505	17.82

The doping ranges provided in Table 4.1 reflect the nominal doping ranges of the materials measured as taken from the material manufacturer. As per the explanation in Chapter 2, the MCD represents a data point through which a fit is made to determine the effective lifetime measurement. The effective lifetime values in Table 4.1 represent the average maximum lifetimes for each type of material measured. In total, there were 2 FZ samples measured, 2 Cz-1 samples, 6 Cz-2 samples, and 8 Cz-3 samples measured. The process for measurement was to place the samples in QM and take measurements for several minutes at one minute intervals. This resulted in a collection of measurements for each material type and sample which is considered a “set” of measurements. The maximum average lifetime was then determined by taking an average over all the sets of measurements for each material.

In order to determine the upper bound on the SRV, the equation,

$$\frac{1}{\tau_{eff}} = \frac{1}{\tau_{bulk}} + \frac{2S}{W} \quad (4.1)$$

was used (the explanation of this equation is given in Chapter 2). Given a lifetime measurement, if one assumes that the sample  $\tau_{bulk}$  is infinite, then the measured effective lifetime  $\tau_{eff}$  will be entirely attributed to the SRV,  $S$ . This method provides a way to obtain the upper bound of surface passivation [32]. The upper bound SRV obtained on the FZ silicon of 3.16 cm/sec is lower than that reported by literature [45] for a similar material. This provides the evidence that the QM is a suitable passivation technique and shows that the method developed here to do so works.

The curves shown in Figure 4.5 provide the measured output from the WCT-120 with an ex-

ample given for each of the measurements provided in Table 4.1. The highest value of lifetime is near 10 msec for the FZ silicon, above 1 msec for the Cz-3 material, and Cz-2 and Cz-3 provide peak lifetimes around 0.4 msec. The Cz-1 and Cz-2 samples show lifetime curves characteristic of SRH defects, which is why the effective lifetime decreases with a decrease in the MCD. The FZ material actually is shown to possess fewer defects as one would expect out of a FZ material given the higher purity of FZ manufacturing. Since all of these measurements were conducted in QM it is likely that any defects captured are due to SRH recombination and not just surface effects. Although, given that QM is not perfectly passivating the surfaces, some of the measured effective lifetime might be due to the lack of surface passivation. Given the upper bound SRV values in Table 4.1 it is assumed that these surface effects on the lifetime curves are minimal.

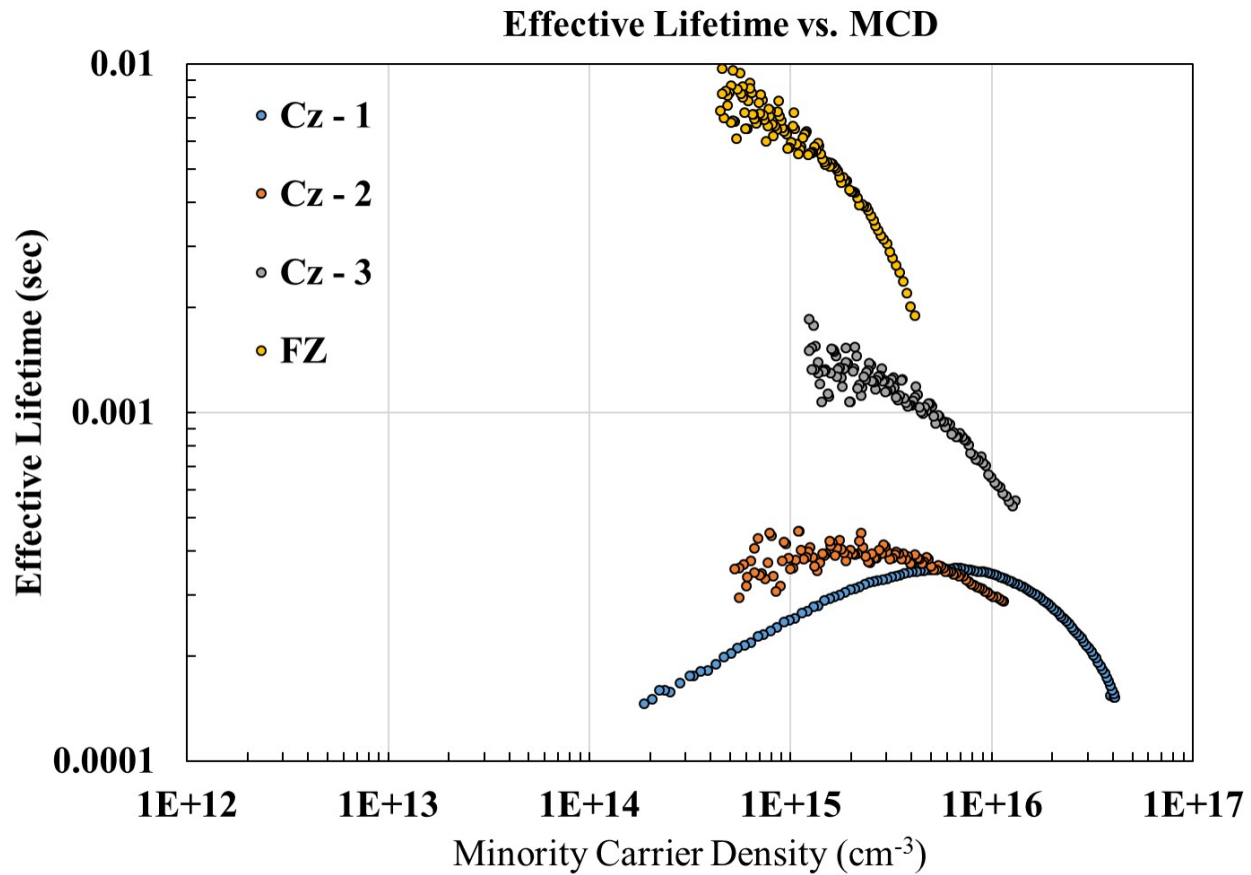


Figure 4.5: Comparison of transient photoconductance output between FZ and Cz silicon passivated with QM.

The highest value of lifetime is near 10 msec for the FZ silicon, above 1 msec for the Cz-3 material, and Cz-2 and Cz-3 provide peak lifetimes around 0.4 msec. The Cz-1 and Cz-2 samples show lifetime curves characteristic of SRH defects, which is why the effective lifetime decreases with a decrease in the MCD. The FZ material actually is shown to possess fewer defects as one would expect out of a FZ material given the higher purity of FZ manufacturing. Since all of these measurements were conducted in QM it is likely that any defects captured are due to SRH recombination and not just surface effects. Although, given that QM is not perfectly passivating the surfaces, some of the measured effective lifetime might be due to the lack of surface passivation. Given the upper bound SRV values in Table 4.1 it is assumed that these surface effects on the lifetime curves are minimal.

These measurements show that the samples are suitable for  $J_{0e}$  measurements as the measured effective lifetimes yield diffusion lengths of around 1030  $\mu m$  for Cz-1 and Cz-2, around 1944  $\mu m$  for Cz-1, and a value of 3446  $\mu m$  for the FZ material. These diffusion lengths are much greater than the thicknesses of the materials which is around 180  $\mu m$  for the Cz material and is about 270  $\mu m$  for the FZ material. This qualifies all of the material as suitable for boron diffusion processes to extract  $J_{0e}$ .

#### 4.2.4 Stability of Quinhydrone-Methanol Passivation

In passivating several bulk samples with QM, observations were made about its stability over time. It was known from the literature that the passivation would degrade when the sample was taken out of solution [45]. Researchers suggested that this had to do with the oxygen from the atmosphere breaking the QHY bond at the Si surface. Further research showed that benzoquinone, a constituent of QHY, was shown to have degradation while samples remained in the solution, again attributed to oxidation of the silicon [48]. The observations made were in contrast to the literature and are shown in Figure 4.6.

The data in Figure 4.6 reflect a measurement of three different Cz silicon samples with the measured lifetime plotted against the measurement time. The increase in the measured effective lifetime with time suggests an increase in the surface passivation with time. This result

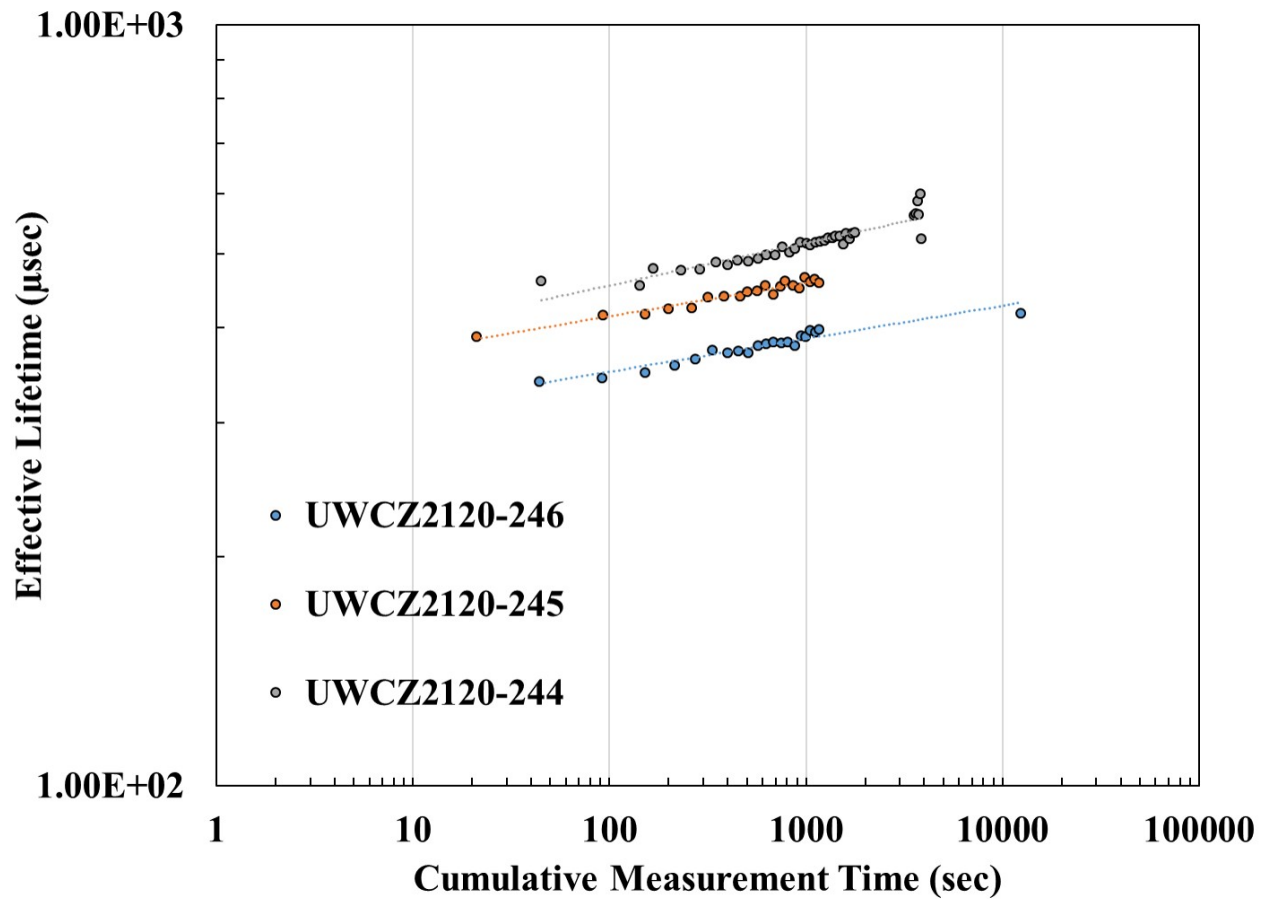


Figure 4.6: Stability of QM passivation over a short time period.

shows that the QM is at least temporarily stable for short measurement times on the order of several thousand seconds (about 15 minutes). It is not an issue that the passivation changes with time in so much as a measurement can be taken within seconds of the sample being submerged in the passivation solution.

### 4.3 Summary

This chapter explained observations made with experimentation performed on bulk silicon samples using QM passivation. A method was developed that allowed for removal of saw damage on as-sawn silicon samples so that QM could passivate the surface. Lifetime data supported the removal of the saw damage shown by the dramatic increase of the measured lifetime in a FZ sample. It was determined that a dish used to contain the QM provided for a

more manageable measurement. Multiple measurements on multiple different kinds of Si confirmed that the QM was effective in passivating the silicon surface with an upper bound of the SRV being achieved on FZ Si of 3.16 cm/sec. The measurements also confirmed that the diffusion length of carriers generated in the Si support use for  $J_{0e}$  extraction. Finally, QM was shown to provide better passivation with time. The goals of this work in this chapter were obtained which support the use of QM as use for passivation in determining the impact of atomic hydrogen on boron diffusions. Though the wafers in this chapter did not contain boron diffusions, the fact that the QM can effectively passivate bulk samples provides evidence that it may also passivate boron diffused surfaces.

## Chapter 5

### Boron Diffusions from BN Solid Sources

The development of a boron diffusion process was necessary in order to provide samples for assessing whether or not an atomic hydrogen treatment could reduce the recombination current density of the diffused region in a solar cell. Because of this, a brief overview of boron diffusion into silicon from boron nitride (BN) solid sources is given. The experimental work in developing and working with boron diffusions using BN solid sources is covered. A comparison of two different methods for removing the boron rich layer (BRL) is provided. The boron diffusion profile in the silicon is important to solar cell device operation because of the  $J_{0e}$  parameter. This is because the boron profile serves as a point of collection for generated minority holes in the n-type base of the solar cell. The doping density of the boron profile can have an impact on the dominant recombination mechanisms in this region, and thus effect device performance.

#### 5.1 Background

Boron diffusions were the first form of diffusion used to form silicon solar cells. Dating back to 1961 Queisser described slip patterns generated from boron diffusions into n-type silicon [56]. The cost of solar compared to competition for other energy sources limited the applicability of such devices in the 1960s. Instead, more emphasis was placed upon using solar cells for space applications. In space, the cost is not necessarily the driving metric for solar cell design, but rather, its energy density. Since early solar cells were silicon based, it was necessary to use a material that was hardened for the radiation exposure in space. This caused the bulk of research to be placed into the development of p-type silicon for which a phosphorous diffusion was used at the front side to generate a n+/p structure. It is interesting that according to Green, that efficiencies in early solar cells rose quite quickly from 6 % in 1954 for a p+/n structure to greater than 10 % within 18 months [57]. However, the transition to p-type cells saw the progression of the efficiency slow such that by 1971 only 14.5 % efficiency had been obtained on a n+/p structure [57]. It is probably a bit speculative to suggest that the effi-

ciency rise was, in part, due to the use of n-type silicon as the base material, but it is curious to ponder. This is especially true with the knowledge that n-type silicon is more resistance to metallic impurities [58], something which was harder to avoid due to technology limitations in the 1950s/1960s.

Because of the creation of p-type cells and the innovation in the aluminum back surface field (Al-BSF) cell design, there was not too much interest in the use of boron diffusions for silicon solar cells for some time. Instead, the focus was on the phosphorous diffusion for n+/p structures, with the aluminum screen printed metal on the backside of the cell allowing for a n+/p/p+ structure to be created. So, it has only become a more recent research topic to investigate the boron diffusion for the development of n-type silicon solar cells.

Boron diffusions typically have a reduced manufacturing throughput when compared to phosphorous diffusions [59]. This manufacturing throughput reduction is felt in industry due to the diffusivity of boron in silicon. Boron diffusions require higher temperatures and longer times to obtain a similar sheet resistance as compared to P diffusion conditions. Interestingly, research on selective emitters have indicated that deeper boron diffusions are more beneficial for selective emitter device design [60]. But, there is also established research that shows that boron diffusions typically create dislocations in the silicon bulk, which lowers carrier lifetime, and thus, diminishes cell efficiency [7]. If carrier lifetime is made too low, then extraction of thermal recombination current via photoconductance measurements can be compromised, which makes the electronic measurement of hydrogenation's effect on the boron diffusion difficult to measure.

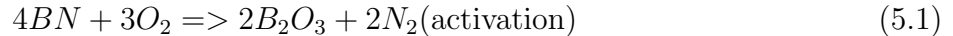
The necessity to extract meaningful emitter recombination current density data coupled with the lack of previously existing boron diffusion recipes were the driving factors in the work of this chapter. The boron doped silicon is the vessel into which atomic hydrogen diffuses and is the main phenomenon that is examined in the whole of this dissertation. To that end, it was necessary to develop a boron diffusion process to obtain desired boron concentration profiles, examine the impact of the effects of boron diffusion on the wafer material, and attempt to characterize the boron diffusion to better understand and frame the interaction with atomic



hydrogen in later chapters.

## 5.2 Boron Diffusion from a Boron Nitride Source Wafer

Boron diffusion from a solid boron nitride source involves the boron nitride wafer, silicon wafers, a quartz boat, and a furnace capable of reaching temperatures as high as 1100°C to allow for the diffusion of the boron. In general, the chemical process of liberating the boron from the source wafer follows [61]:



The first chemical process is obtained by placing the source wafers in an oxidizing ambient to activate them. This process grows a layer of boric oxide on the source wafer which acts as the source of boron in later steps. After the source wafers are oxidized they are loaded into a quartz boat as shown in Figure 5.1.

The quartz boat is loaded onto the furnace arm and then is driven into the furnace tube. To achieve boron diffusion into the silicon wafer, high temperatures ( $> 800^\circ\text{C}$ ) are used such that the boric oxide at the surface of the boron sources vaporizes and diffuses to the silicon wafer surface as shown in Figure 5.2. Once on the surface, a reaction occurs forming silicon dioxide and liberated boron atoms as shown in the deposition equation. These liberated boron atoms are then free to diffuse into the silicon lattice where they either travel by vacancy assistance, interstitial kick out, or interstitially assistance [62].

An excellent overview of the microscopic mechanisms responsible for B diffusion are given by [62], but a few key ideas are highlighted here to aid in understanding how the boron diffuses into silicon. For the specific case of B diffusion it is given a fraction of 1.0 for the interstitial mechanism suggesting it diffuses at the atomic scale by interstitial processes. The activation energies of dopant diffusion is about 1 eV lower than for silicon self diffusion, which suggests a barrier lowering. Coulombic effects do not contribute to this lowering entirely. One possi-

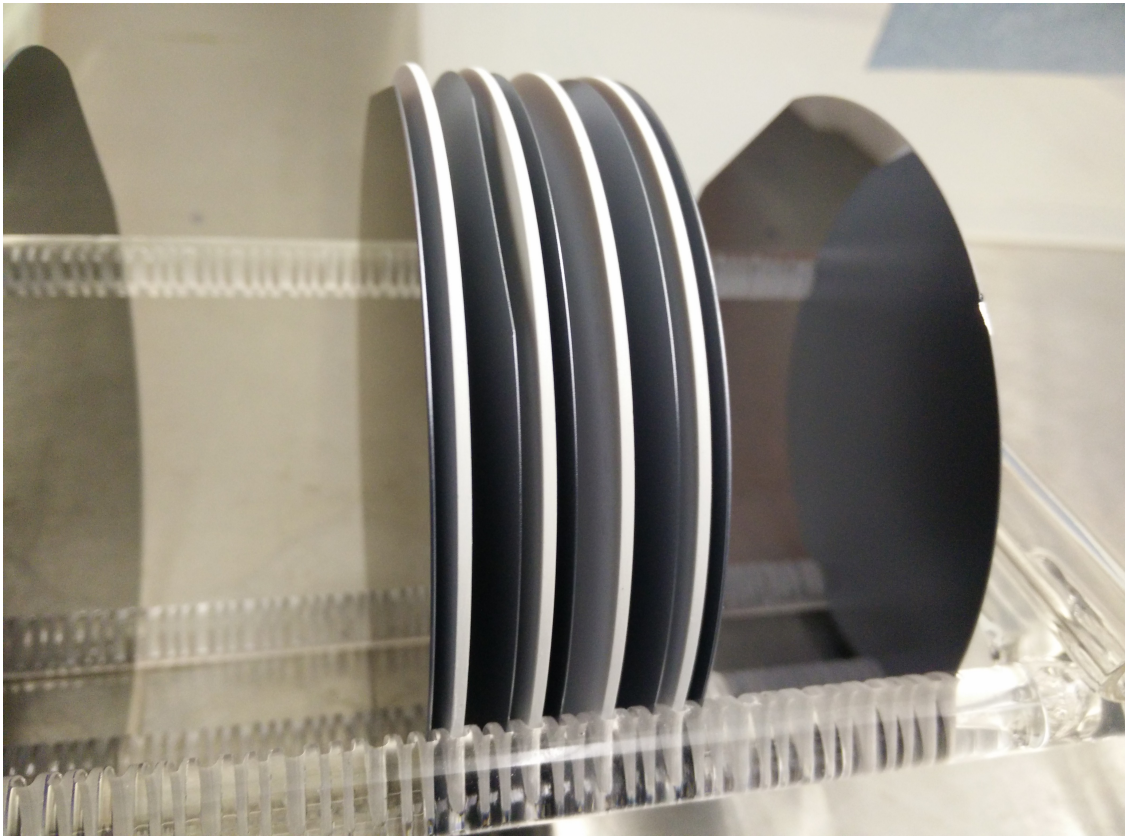


Figure 5.1: Image showing how boron nitride source wafers (white) are loaded into a quartz boat with silicon wafers.

ble mechanism to barrier lowering is lattice relaxation around the Si atoms, with theoretical calculations indicating B causes inward relaxation of the silicon lattice by 12 percent. Full coupling of the dopant defect interactions gives a better match to experimental data for a B diffusion. The flux of the boron species diffusing in the silicon is governed by the gradient of dopant concentration, the gradient of interstitials, and the electric field. Charged point defect diffusion is dependent on the Fermi level of the charged point defect.

The deposition of a boric oxide on the surface of the silicon wafer provides for a source of B atoms. However, it is well known that a boron rich phase forms between this boric oxide and the silicon surface [61, 63]. Termed the boron rich layer (BRL) this material system thickness depends upon diffusion conditions and has been published to be composed of  $\text{SiB}_x$  with  $x = 4$  or 6 [64]. It has also been published that such a layer acts as an efficient gettering engine to remove impurities that might otherwise cause lifetime degradation in the wafer bulk.

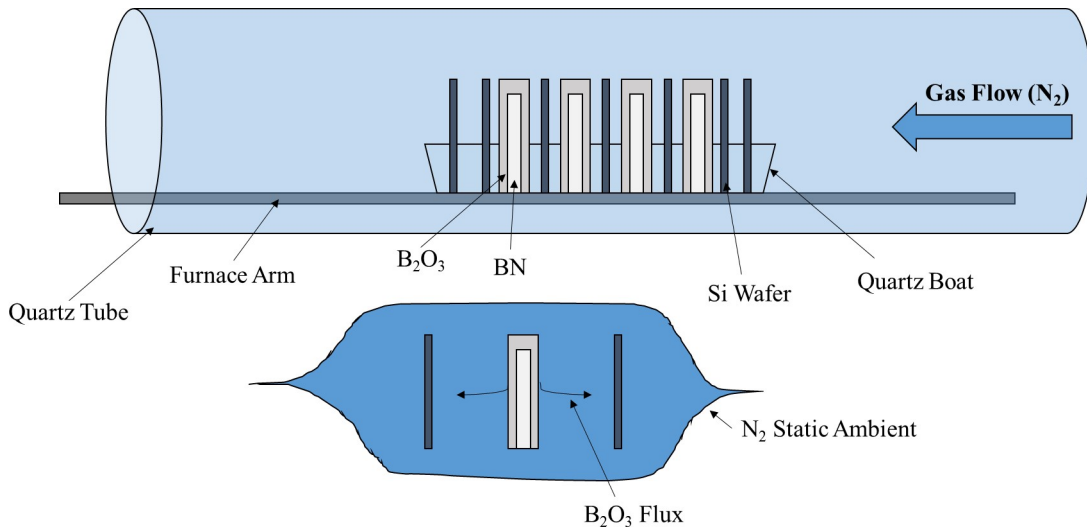


Figure 5.2: This image shows how Nitrogen gas forms a column of nitrogen around the sources and wafers. This allows for the diffusion of the B<sub>2</sub>O<sub>3</sub> from the source to the wafer surface.

Gettering refers to the physical process by which defects move through the lattice and are gathered together in a particular region of a material system. This BRL has to be removed to reveal a functioning boron diffusion, otherwise, the lifetime of the material is compromised from trapped defects in the BRL layer. In fact, historical methods to remove this BRL involved the use of an oxidation to oxidize the silicon underneath the BRL (oxygen can diffuse through the BRL) which then allowed for a simple HF etch to lift off the BRL exposing the boron doped silicon underneath. There are thermal diffusion conditions that exist under which a BRL is not known to form, while others suggest that the BRL will always form in the presence of heavy B concentrations and Si. In the diffusions studied here, the BRL was always observed.

### 5.3 Experimental Methods

Different sets of samples were used to develop the B diffusion recipes used within this chapter and the dissertation. Table 5.1 gives an overview of the characteristics of the samples used. Prior to any diffusion, samples underwent a strict cleaning process. Some of the materials used above (UWCZ-XX and UWCZ2120-XX) were solar grade materials and were received

Table 5.1: Nominal characteristics of wafer material used to study boron diffusions.

Sample Name	Material	Resistivity	Type	Orientation	Size
UWCZ-XX	Cz	1-10 ohm-cm	n	<100>	6" pS
UWCZ2120-XX	Cz	1-10 ohm-cm	n	<100>	6" pS
G35XY-XX	FZ	30-40 ohm-cm	n	<111>	6"
P0A9	Cz	4.8 ohm-cm	n	<111>	6" pS

Table 5.2: Standard cleaning process that most samples go through before a diffusion process

Step Number	Cleaning	Chemicals and Ratios	Time (mins)	Temp. (°C)
1	Rinse	DI Water	3	25
2	Organic	1:1 H <sub>2</sub> SO <sub>4</sub> :H <sub>2</sub> O <sub>2</sub>	10	(> 130)
3	Oxide Strip	1:10 HF:H <sub>2</sub> O	2	25
4	Saw Damage	TMAH	variable	90-100
5	Organic	1:1 H <sub>2</sub> SO <sub>4</sub> :H <sub>2</sub> O <sub>2</sub>	10	(> 130)
6	Oxide Strip	1:10 HF:H <sub>2</sub> O	2	25
7	Metallic Ion Clean	DI Water	10	60-70
8	Oxide Strip	DI Water	2	25

with saw damaged surfaces. The cleaning process involved an organic clean, oxide strip, saw damage etch, and finally finished with a full RCA clean. The details of such a cleaning process are shown in Table 5.2

Diffusions were carried out in a Bruce BDF4 diffusion stack featuring 3-zone temperature control and automated boat drive-in. The source of boron during the diffusion process was from a BN solid source. The initial diffusion recipe that was tried was provided by Saint-Gobain, the manufacturer of the BN solid sources. A thermal profile of such a diffusion recipe is shown in Figure 5.3.

The diffusion temperature profile of Figure 5.3 corresponds to the measured boron dopant profile of Figure 5.7. The soak times from Figure 5.3 is 1 minute. The control system of the Bruce BDF4 was able to repeat this short soak step without issue. The total diffusion times from Figure 5.3 is 91.98 minutes. The temperature profile begins with an initial temperature of 400°C and ramps to an intermediate 800°C set point wherein the wafers in the furnace are allowed to thermally stabilize before the 1000°C soak step. The thermal profile in Figure 5.3 can be used to estimate the total diffusion time of the boron into the silicon wafer. In addi-

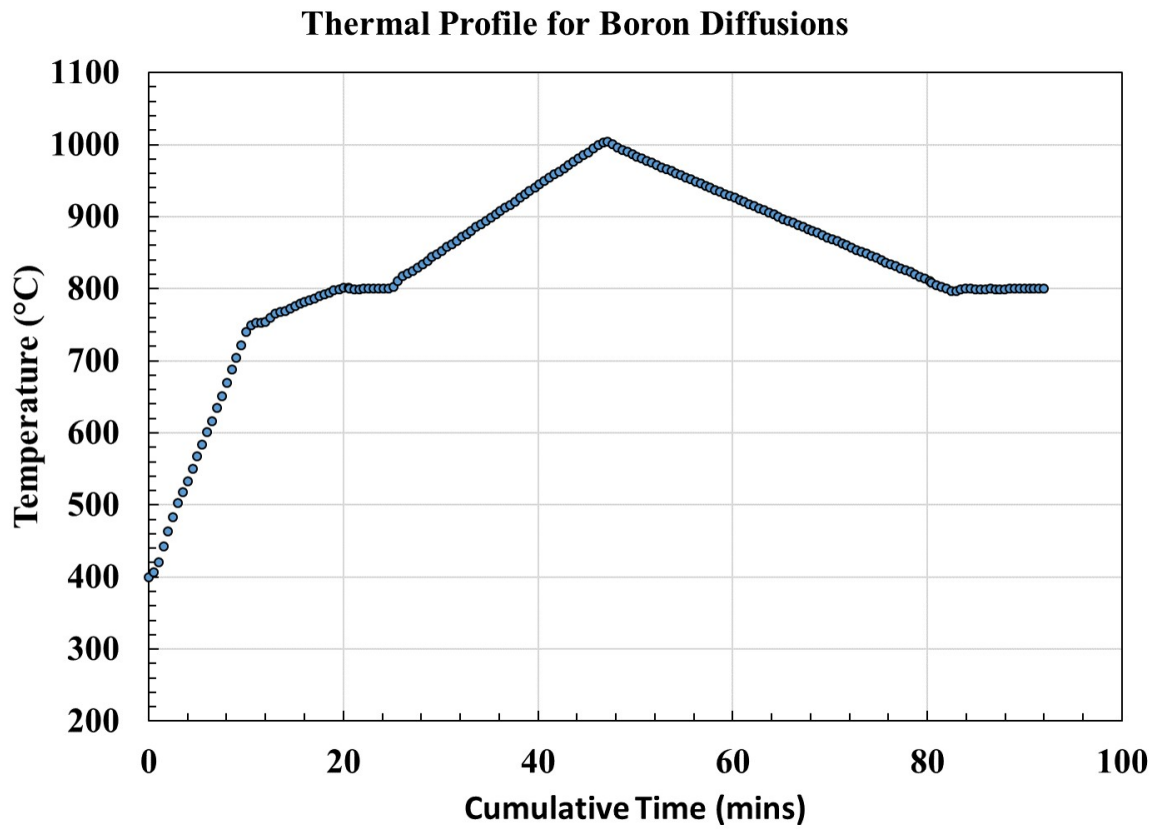


Figure 5.3: Thermal profile of diffusion recipes showing temperature variation with time.

tion, the data is important for replicating the work described in this section.

After the diffusion process the BRL layer is present which must be removed. Samples are then characterized using electrochemical capacitance voltage (ECV) to obtain information about the boron doping density versus depth. To obtain the sheet resistance of the diffused layer the four point probe (FPP) method is utilized. Photoconductance measurements are taken to extract the  $J_{0e}$ . Each of these three characterization methods are discussed in Chapter 2.

#### 5.4 Two Methods of Removing the BRL

In performing the work in this dissertation, it was the recommendation of the manufacturer of the BN sources that a low temperature oxidation (LTO) process be used to remove the BRL. More recent research articles about the removal of such a BRL have been shown that a chemical etch procedure can also remove the BRL [65]. The advantages of the etch procedure are that the detrimental effects of the LTO can be avoided. During the LTO, samples are subjected to a oxidation process where temperatures can be as high as 750°C or 800°C. This higher temperature process can cause the creation of crystal defects due to thermal stressing at the BRL/Si interface [66].

In the LTO method used in this dissertation, an oxidizing ambient is used to oxidize a thin layer of silicon underneath the BRL, which then allows for a follow up chemical etch procedure to remove the BRL layer. This method is performed at 750°C for variable amounts of time according to the thermal profile in Figure 5.4 (a). It is assumed that the composition of the BRL does not change significantly from run to run and that it also only becomes thicker for an increase in diffusion time. With these assumptions in hand, one can perform an experiment where various oxidation times are used. After each oxidation run, the BRL is lifted off and the sheet resistance is measured. By tracking the percent change in sheet resistance ( $\Delta R_{sh}$ ) after each subsequent oxidation and etch, a plot can be created of  $\Delta R_{sh}$  against time as shown in Figure 5.4 (b). The data points in Figure 5.4 (b) each represent a separate oxidation process carried out on a different diffusion sample. The time of the oxidation process in Figure 5.4 (b) relates to the time the sample is maintained at 750°C in Figure 5.4 (a).

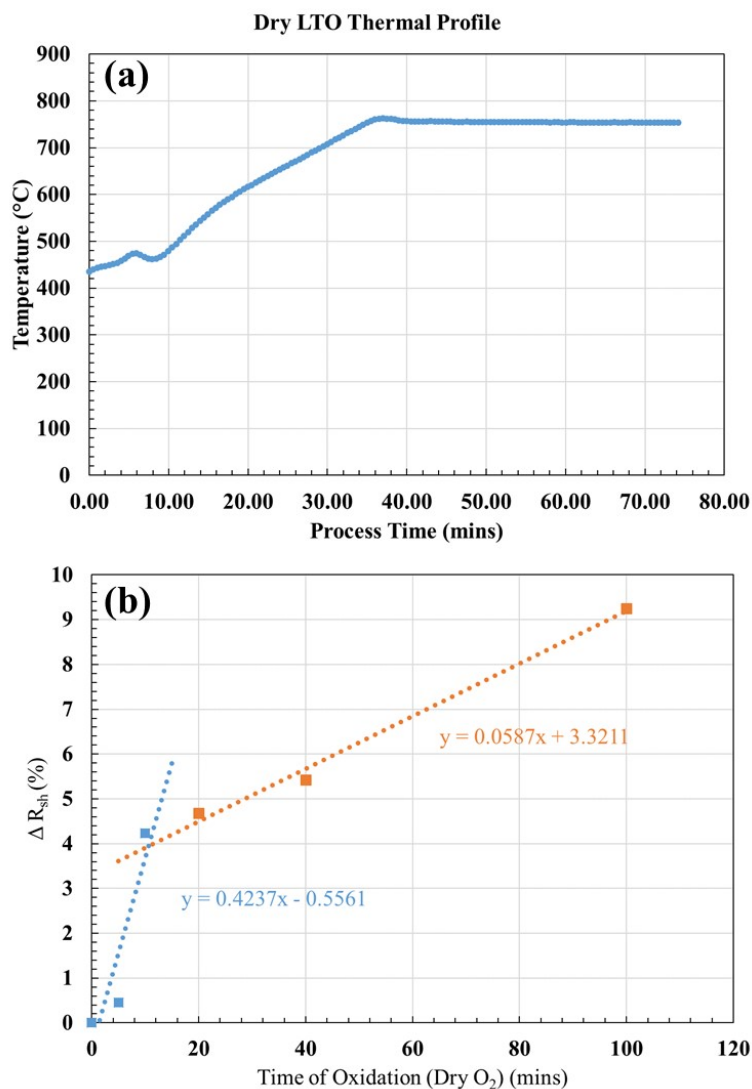


Figure 5.4: (a) Thermal profile of LTO recipe with (b) measured  $\Delta R_{sh}$  versus oxidation time.

Examining Figure 5.4 (b) one can see evidence for two different slopes as labeled by the fit lines. These slopes arise because after the LTO, if any part of the BRL remains, it gives a lower effective  $R_{sh}$  measurement. Once the BRL is totally removed via oxidation and etch, the slope changes as there is no longer a BRL to interfere with the  $R_{sh}$  measurement. The oxidation times were chosen based on experience in performing the LTO at a known oxidation time (20 minutes) recommended by the manufacturer of the BN solid sources [67]. Since it was desired to see the two slopes created by repeated oxidation, a collection of shorter times, 0, 5, and 10 minutes, were chosen, as well as longer times at 20, 40, and 100 minutes. The removal

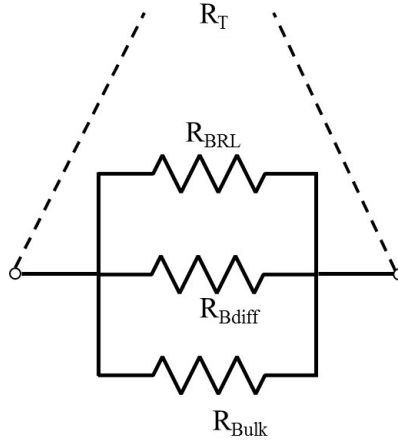


Figure 5.5: Parallel resistor model that explains measured  $R_{sh}$  values using FPP with a BRL in place.

or partial removal of the BRL layer is best explained by imagining a parallel resistor type situation as shown in Figure 5.5. The parallel resistor model shown has a value of a resistance for each material layer after a boron diffusion process. The resistance,  $R_T$ , represents the total resistance which is what would be measured by a FPP.

The resistance of the BRL layer is quite low in comparison to  $R_{bulk}$  but not nearly as low in comparison to  $R_{Bdiff}$ . In this way, the BRL acts to load down the measured  $R_T$  value that would be seen by a FPP measurement. When the  $R_{BRL}$  resistor is fully removed via etching or oxidation, a much simpler model emerges, where the total resistance measured is simply the boron diffusion (due to its low sheet resistance compared to  $R_{bulk}$ ). Any intermediate oxidation that only partially removes  $R_{BRL}$ , does not change the total resistance,  $R_T$ , so much as to drastically alter the calculated  $\Delta R_{sh}$  value. So long as the BRL is still in place, small changes in the measured  $R_{sh}$  are found which is shown by the first two data points at 0 and 5 minutes in Figure 5.4 (b). Finally, after the full BRL is removed, larger changes in the sheet resistance are observed. These larger changes are due to the fact that the extended oxidation times are removing part of the boron diffusion, thus increasing the resistance  $R_{Bdiff}$ , which is shown by the data points at 10, 20, 40, and 100 minutes in Figure 5.4 (b). This allows for repeated oxidations to occur on different samples that have undergone a boron diffusion. The data shown in Figure 5.4(b) are for a 1000°C 1 minute soak time (the thermal profile as given



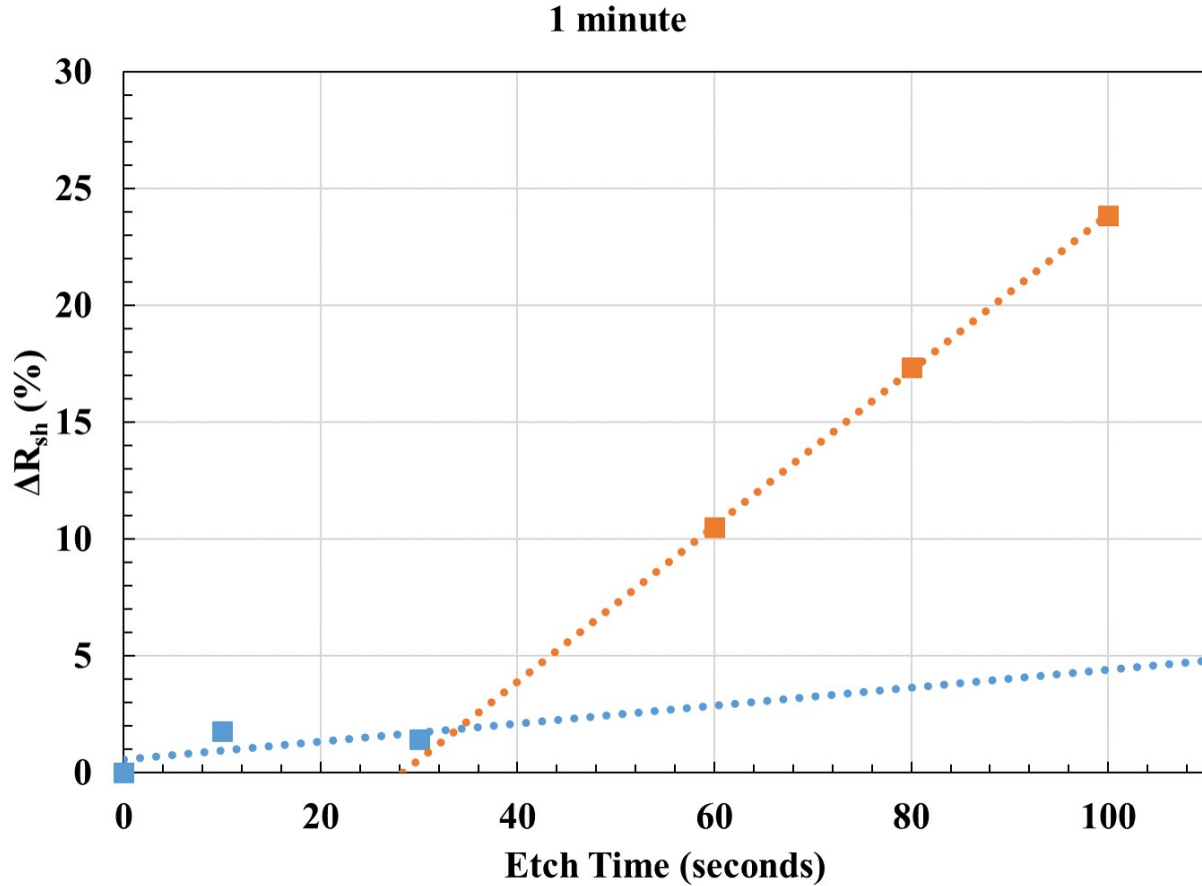


Figure 5.6: Percent  $R_{sh}$  change plot against etch time for chemical removal of the BRL.

in Figure 5.3). To arrive at an estimate for how long it was necessary to oxidize the samples to remove the BRL, six oxidations were carried out as shown in Figure 5.4 (b). The intersection of the two fit lines represents the approximate time needed for full removal of the BRL. Another method to remove the BRL is to subject the BRL to a chemical etch procedure. The BRL is actually not chemically soluble in hydrofluoric acid (HF) like the BSG layer, but an oxidizing etch, such as a combination of HF:HNO<sub>3</sub>:CH<sub>3</sub>COOH can be used to etch away the BRL on top of the silicon. A disadvantage of this method is that it can etch the underlying silicon. However, the same method of plotting  $\Delta R_{sh}$  against etch times can be used to extract estimated experimental etch times to fully remove the BRL layer. This was performed on several samples having undergone the boron diffusion process at 1000°C (thermal profiles as shown in Figure 5.3). The  $\Delta R_{sh}$  plots against etch time in seconds is shown in Figure 5.6.

To create the plot in Figure 5.6 six diffused samples, still having the BRL, were subjected to an etch in a solution of 1080 mL  $\text{CH}_3\text{COOH}$  + 108 mL  $\text{HNO}_3$  + 12 mL of HF. The  $R_{sh}$  was measured using FPP on each sample, followed by a 2 minute dip in 1:10 HF to remove any accumulated surface oxide during the FPP measurement. Then the samples were dipped in the etching solution at specified times (see Figure 5.6). Two fits lines were generated for the data, as was done for determination of the LTO process oxidation time. The intersection of the two fit lines indicated that the etch time needed to remove the BRL layer for the 1 minute diffusion process was approximately 30 seconds.

### 5.5 Measurement of Boron Diffusions and Extraction of $J_{0e}$

Important parameters in a boron diffusion include doping concentration profile, surface concentration, and junction depth. As covered in Chapter 3, a way to measure the boron diffusion profile, and hence obtain the diffusion parameters, is to use ECV. For the profiles in this chapter, ECV profiling was used.

Figure 5.7 shows a boron diffusion profile measured using ECV as well as a complementary error function (ERFC) fit to the measured data. The ERFC fit is used to help estimate the junction depth of the boron diffusion. Practical limitations with the ECV tool used to gather this data limited the collection of data to no more than  $10^{18} \text{ cm}^{-3}$  for the measured diffusion profile. The surface concentration was found to be at  $1.6 \times 10^{20} \text{ cm}^{-3}$  and the experimental profile tends to follow the ERFC shape until the experimental data starts to drop off. This behavior is seen in the last three data points of the measured profile in Figure 5.7. A straight line (dashed) was added to the plot in Figure 5.7 to aid in seeing the junction depth. The junction depth is determined to be where the boron concentration profile crosses the bulk substrate doping, which for the samples used here occurs at a value of about  $2 \times 10^{15} \text{ cm}^{-3}$  and is indicated by the thick black horizontal line at the bottom of Figure 5.7. The estimated junction depth from the ERFC fit was determined to be  $0.64 \mu\text{m}$ , where as the guideline for the measured profile in Figure 5.7 indicates a junction depth of  $0.5 \mu\text{m}$ .

In examining the measured profile in Figure 5.7, the box-like behavior of boron can be seen

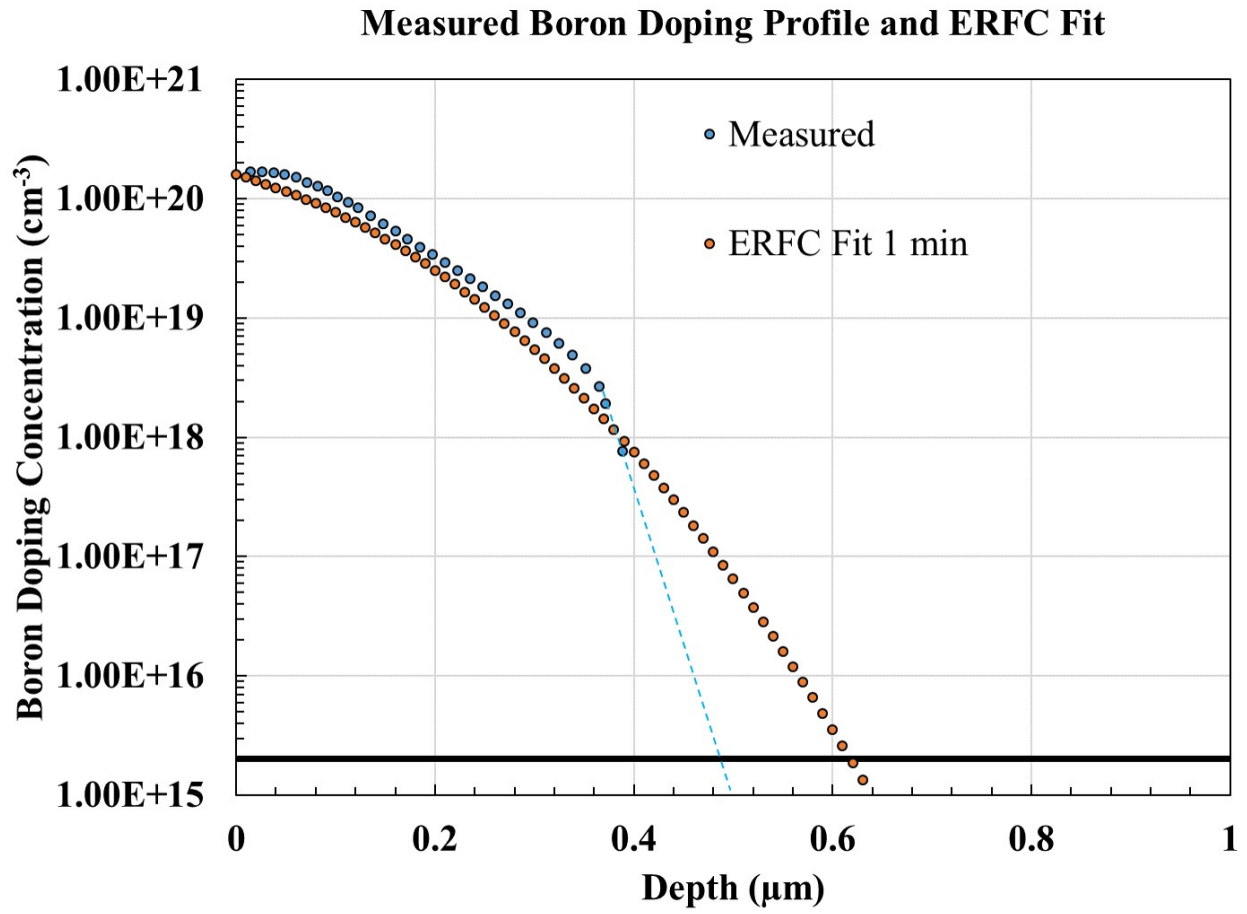


Figure 5.7: Boron diffusion profile as measured by ECV along with an ERFC fit to the data.

in how the last three data points begin to form a linear trend. This box behavior is typical of boron and is known to come from a diffusivity that is concentration dependent [62]. This suggests that measured profile has a junction depth less than the prediction made by the ERFC fit, as is indicated. The measured  $R_{sh}$  of the measured diffusion profile was found to be  $48.8 \Omega/sq.$ , whereas the calculated value was found to be  $52.75 \Omega/sq.$ , a 7.7% difference. It is possible that the ECV measurement is in slight error, and that either the surface concentration is lower, or the junction is a bit deeper, closer to the ERFC fit junction depth estimate. Both of these options would bring the calculated  $R_{sh}$  value closer to the measured value. Despite the difference, there is still strong confidence that the measured profile data is an accurate depiction of the diffusion process described in previous sections.

Figure 5.8 shows the output of EDNA 2 calculations for the boron diffusion profile shown in Figure 5.7. EDNA 2 is an online software that calculates diffused region recombination in silicon. It has been compared and validated against both PC1D and Sentaurus, a commercially available TCAD software for semiconductor device simulation [68–71].

The plot in Figure 5.8 shows the breakdown of the variation in  $J_{0e}$  with changes in the effective SRV. The dashed lines in each plot show the constituents of the total  $J_{0e}$  (dark black line in the figure). This calculation allows for the determination of what can be termed the "Auger Limit" of the diffusion profile. When the effective SRV tends to 0 cm/sec (perfect passivation) it is evident that Auger recombination becomes the limiting factor in determining the total  $J_{0e}$  of the emitter. This value of  $J_{0e}$  where SRV tends to 0 cm/sec is the "Auger Limit". For the measured profile of Figure 5.7, the "Auger limit" occurs at  $51.4 \text{ fA/cm}^2$ . This calculated  $J_{0e}$  value is useful in a comparison against measured  $J_{0e}$  values.

For the diffusion profile shown in Figure 5.7, photoconductance (PC) measurements were performed on symmetrically diffused lifetime structures. As outlined in Chapter 3, the symmetrical lifetime structure allows for deduction of  $J_{0e}$  from a PC measurement. Multiple symmetrical lifetime structures, featuring the diffusion process discussed in previous sections, were generated over a number of weeks. The samples were then measured using a WCT-120 Sinton lifetime tester (as described in Chapter 3) with quinhydrone-methanol (QM) used for surface

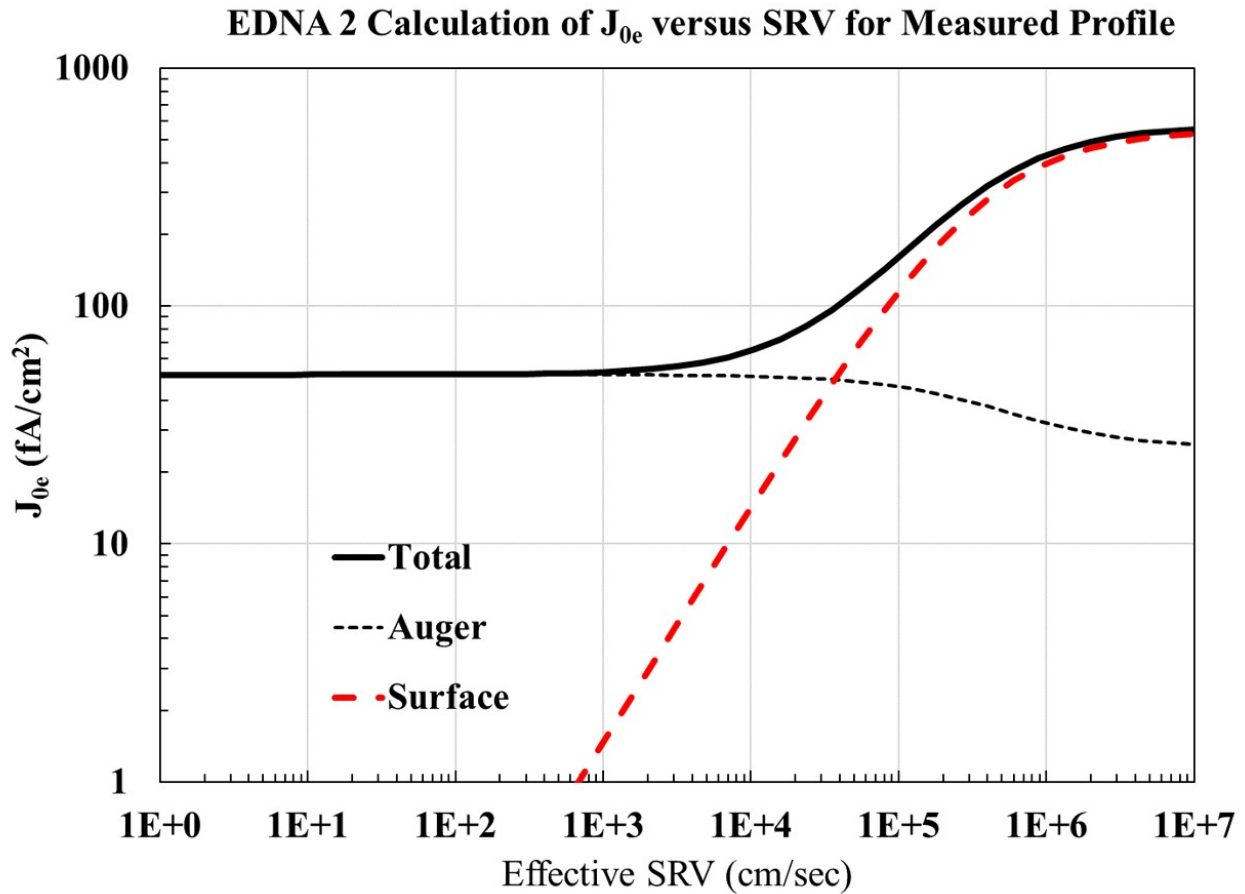


Figure 5.8: EDNA 2 calculations showing  $J_{0e}$  plotted against effective SRV for the profile shown in Figure 5.7.

passivation. All measurements were performed in a solution of 0.07 M QM. This concentration of solution was found to give the best results on bulk silicon (Chapter 4) and in addition, it is the solubility limit of quinhydrone in methanol.

It is natural to pose a question at this point regarding the use of QHY-ME passivation on silicon samples featuring B diffused surfaces. The behavior of QM passivation on a boron diffused surface is something that is not readily found in the literature. All of the studies found concerning QM involve the passivation of bulk n and p-type silicon, but no studies found had used QM passivation on boron diffused samples. A reason for the lack of available research on such a topic probably has to do with the fact that QM is a temporary passivation technique and would not typically be applied to a boron diffusion to form a finished device. It was deemed useful for the experiments in this dissertation because it seemed to provide excellent

passivation (Chapter 4) to bulk silicon and was expected to passivate boron diffusions equally well. In addition, as alluded to in Chapter 1, atomic hydrogen does not readily permeate the dielectrics used on commercial solar cells. Since the focus of this dissertation was on the underlying impact of the atomic hydrogen on the  $J_{0e}$  of a boron diffusion, QM seemed to provide an excellent tool through which to suppress surface recombination to be able to extract  $J_{0e}$  using the lifetime tester tool on symmetrically diffused test structures.

The focus here is on showing that QM can adequately passivate a boron diffused surface and to make sure that the passivation is stable enough to obtain a measurement that yields  $J_{0e}$ . Given the age of the diffusion furnaces used to produce the boron diffusions for the lifetime test structures, there was some experimental uncertainty regarding whether or not the boron diffusions were of device quality. To dispel this uncertainty, measurements were also performed on samples produced at an outside lab with completely different equipment on different silicon. These samples were treated as a known good that should possess a low  $J_{0e}$  value.

All samples were cleaned using a Piranha process then dipped in HF 2 minutes prior to being submerged in QM. The QM was contained in a polypropylene dish as discussed in Chapter 3. Figures 5.9 and 5.10 show the results of the measurements for the G35XY FZ samples and P0A9 Cz samples (obtained from an outside lab), respectively. For each sample measured, the  $J_{0e}$  was extracted over a series of minutes. The error was calculated from the collective standard deviation of each measured sample as determined from its average  $J_{0e}$ . The average  $J_{0e}$  was found by averaging the measured values for a given sample. For the FZ material in Figure 5.9, the population average  $J_{0e}$  was found to be  $66.28 \pm 8.53$  fA/cm<sup>2</sup>. The data shown in Figure 5.10 was determined to have an average  $J_{0e}$  of  $68.026 \pm 16.52$  fA/cm<sup>2</sup>.

Examining the data in Figure 5.9 and 5.10 the measurements can be seen to be fairly stable over short time periods. With most samples there was a slight drift in the measured value of  $J_{0e}$  upward over time which was attributed to methanol evaporating out of the dish during the course of the measurement. The data in Figure 5.9 and 5.10 are shown to occur above and below the auger limit calculated by EDNA 2. Probable reasons for this might be drift of the diffusion furnace temperature and variations in sample temperature during the diffusion

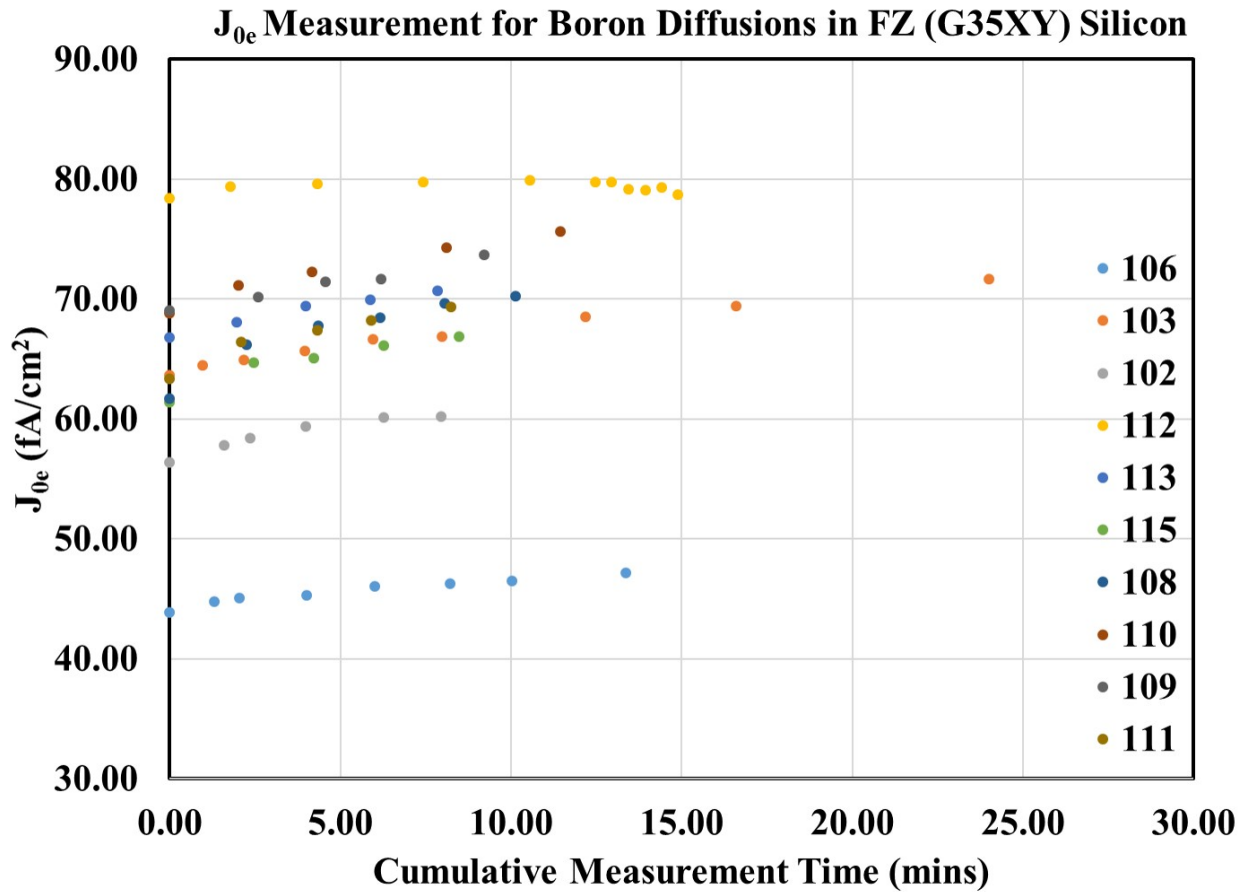


Figure 5.9: Measured  $J_{0e}$  for B diffusions in G35XY FZ material.

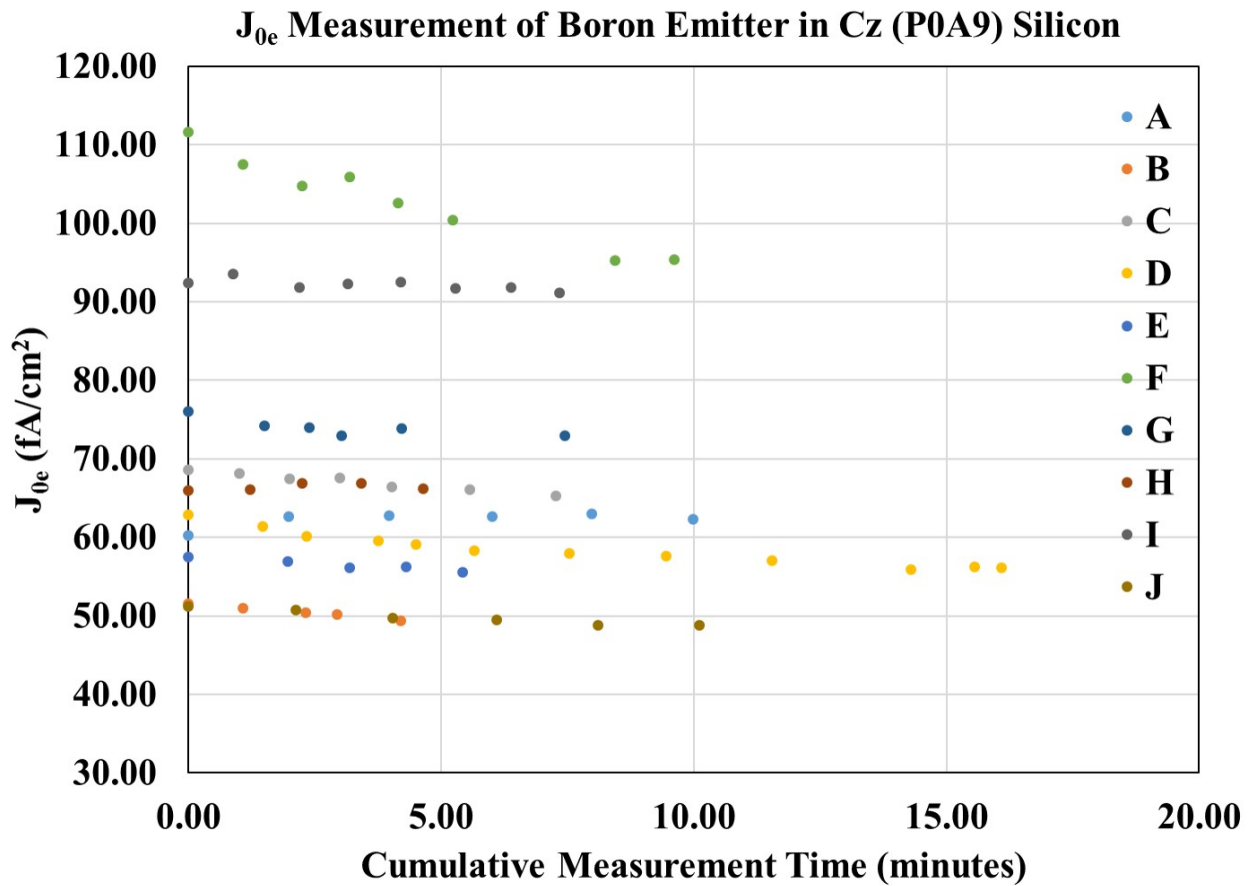


Figure 5.10: Measured J<sub>0e</sub> for B diffusions in P0A9 material from an outside lab.



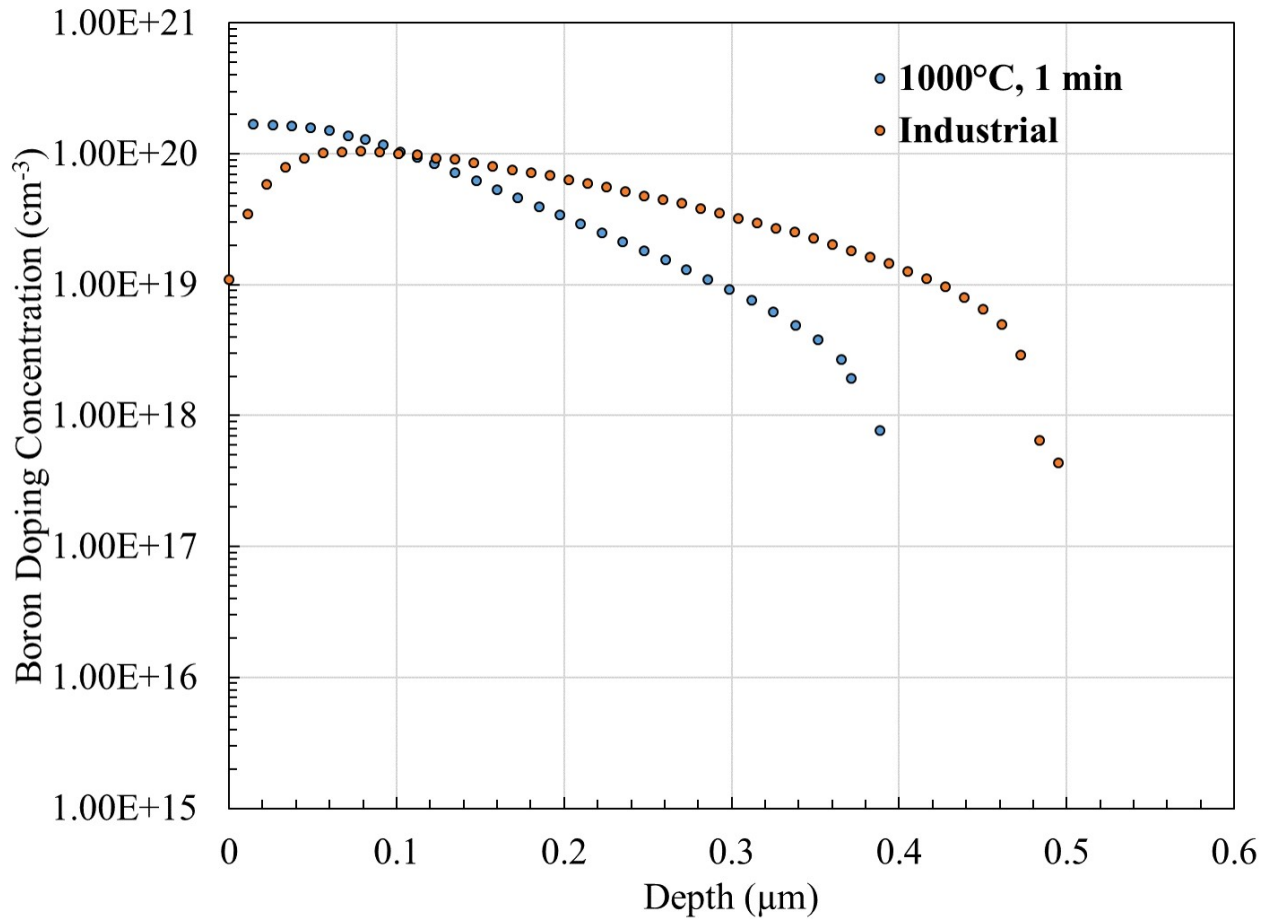


Figure 5.11: Comparison between boron diffusion profile created locally versus one that is from an industrial process.

process creating slightly different emitters with differing surface concentrations and junction depths. This is why it was decided to collect enough data to form population averages and observe the natural variation in the measurement as a result of environmental factors.

The profile shape of the 1000°C 1 minute diffusion closely resembles an industrial diffusion profile. An industrial diffusion profile was provided by a commercial partner of Picasolar, Inc. ECV measurements were obtained from this sample and compared to that created locally.

The profiles are shown together in Figure 5.11. However, this industrial process profile is not the profile that was used on the P0A9 samples.

The main differences between the two profiles are a lower surface concentration for the industrial B diffusion profile and a slightly deeper junction depth. The sheet resistance of the two diffusion profiles are 49.7  $\Omega/sq.$  for the industrial profile and 53.2  $\Omega/sq.$  for the 1000°C 1

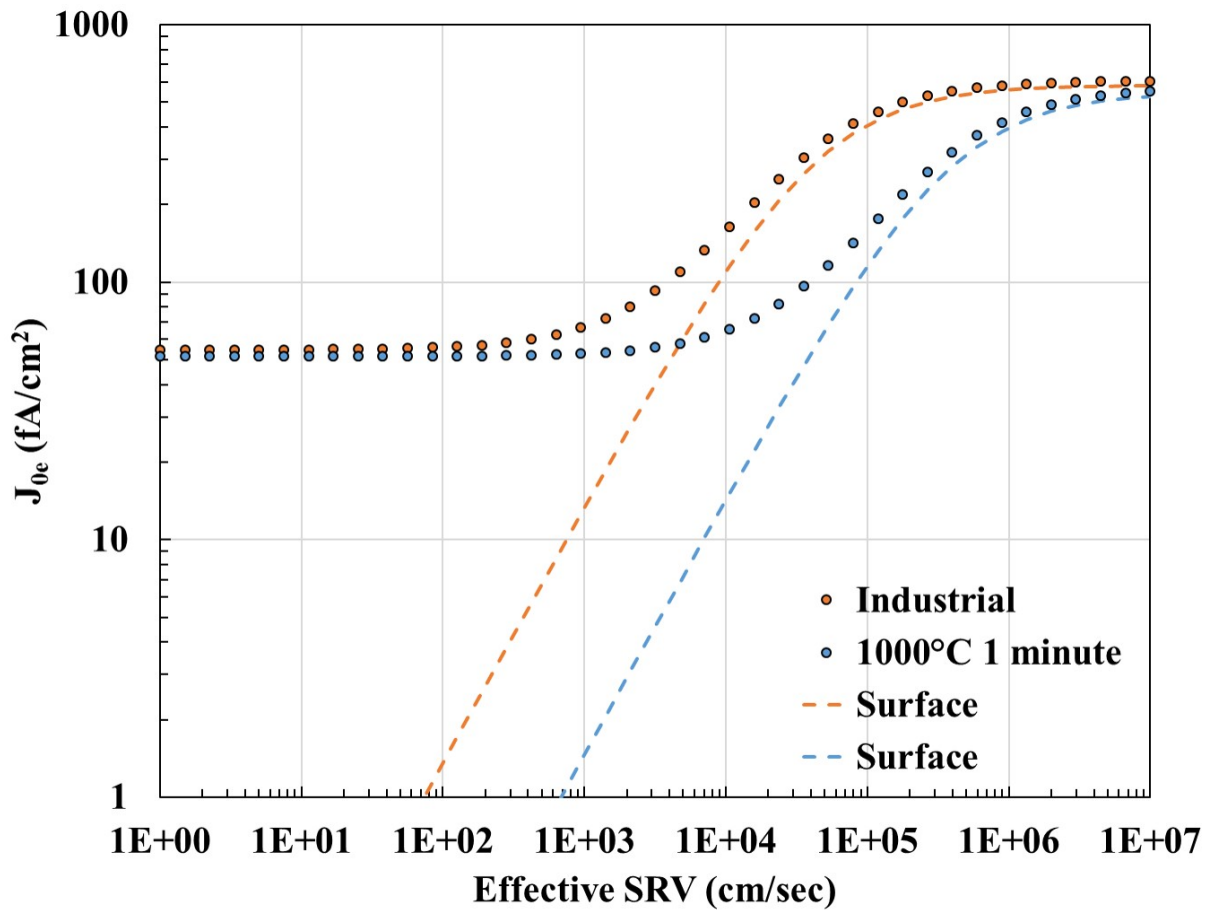


Figure 5.12: EDNA 2 calculation of boron diffusion profiles shown in Figure 5.11. Colors are coordinated between the plots.

minute diffusion. The reduction in the surface concentration for the industrial B diffusion process is a by-product of the BRL removal for the diffusion. Whereas the chosen method in this work is a chemical removal process, that of the industrial profile shows how segregation into an oxide layer has reduce the doping at the near surface. The  $J_{0e}$  surface curves were generated for both profiles in EDNA 2 and are shown in Figure 5.12.

The reduction of the doping concentration in the near surface of the industrial profile causes a shift in the  $J_{0e}$  versus effective SRV curve. This is due to the fact that the surface in an unpassivated state will always have a maximum number of recombination sites (due to abrupt ending of the crystal lattice). Since the 1 minute "in-house" diffusion has a heavier surface doping, there exists more Auger recombination in the emitter as compared to the in-house diffusion. This Auger recombination acts to passivate the surface in the sense that the SRV

will be, overall, a lesser impact on the emitter performance. In practice, this means that the industrial diffusion will require much better surface passivation than that of the heavier diffusion. Given the short diffusion time necessary to form such an emitter, and its comparable characteristics, the "in-house" diffusion is more ideal for a device. This data supports the fact that the boron diffusion process developed in this work possess a  $J_{0e}$  that is comparable to industrial-like processes. In addition, the diffusion profile that was created shares characteristics (in terms of its profile shape) with that of an industrial boron profile.

## 5.6 Summary

This section gave the reader an overview of the effort taken to develop a thermal boron diffusion process using BN solid sources and a Bruce BDF4 diffusion stack. Two different methods of removing the BRL were explored, an LTO and a chemical removal process. The chemical removal process was preferred over the LTO due to the fact it lessens a high temperature furnace step in processing. It also occurs in minutes on a wet bench as opposed to close to 1.5 hours at 750°C. The boron diffusion was profiled using ECV to obtain information regarding surface concentration, junction depth, and the doping concentration with depth. The surface concentration for the diffusion profile studied was found to be  $1.6 \times 10^{20} \text{cm}^{-3}$ . The junction depth was determined to be from 0.55 to 0.64  $\mu\text{m}$ , however FPP measurements increased the confidence that it was closer to 0.55  $\mu\text{m}$ . The 1 minute diffusion profile was chosen as a baseline profile as it most closely resembled that of an industrial diffusion profile. EDNA 2 calculations were used to estimate the "Auger Limits" of each profile. Measurements of the actual  $J_{0e}$  using a WCT-120 Sinton Lifetime tester were taken on a number of samples. The measurements in FZ and Cz silicon were compared to samples obtained from a partner of Picasolar, Inc. The average measured  $J_{0e}$  of each profile was found to correspond closely with one another, however, the deviation in the outside samples was found to be nearly double of that than the locally created diffusions. The in-house boron diffusion profile was also compared to an industrial boron diffusion profile. This vets the boron diffusion process developed in this chapter as well as the QM passivation of the boron diffusions as being consistent with a calcu-

lated total bound (error) on the measurement.

## Chapter 6

### Hydrogenation of Boron and Reduction in Recombination Current

As explained in Chapter 2, the fundamental device parameter,  $J_{0e}$ , provides a description of the recombination activity in a given region of the device. Reducing  $J_0$  is a key design role in making the best silicon solar cells. In this chapter, atomic hydrogen is applied to symmetrically diffused test structures and the  $J_0$  is measured using photoconductance spectroscopy. Surface passivation is provided by quinhydrone-methanol (QM) as was done in Chapter 4 for bulk silicon and in Chapter 5 for boron diffusions. Without surface passivation in place, surface recombination processes dominate, and a measure of  $J_{0e}$  is not possible. Several samples are passivated and compared to control samples in order to obtain an experimental error on the measurement, as was done in Chapter 5 for boron diffusions.

#### 6.1 Experimental Methods

The silicon used for extraction of  $J_{0e}$  was scribed to 2" squares from full size industrial-like 6" pseudo-square wafers to increase sample count and to meet local infrastructure requirements. After dicing, the silicon underwent an initial Piranha clean ( $\text{H}_2\text{O}_2:\text{H}_2\text{SO}_4$  1:1) for 10 minutes, followed by a saw damage etch in Tetra-Methyl-Ammonium-Hydroxide (TMAH) at 90°C for 10-14 minutes. TMAH was chosen as an etchant as it has been previously shown to promote the creation of a surface that provides better passivation [53]. After the TMAH etch, samples went through a full RCA clean including a second Piranha clean for 10 minutes, a dip in 1:10 HF, and finally an RCA-2 clean (1:1:5 HCl: $\text{H}_2\text{O}_2$ : $\text{H}_2\text{O}$ ) at 70°C for 10 minutes.

To prepare samples with boron diffusions, the same process as outlined in Chapter 5 was used. BN sources were used with a Bruce BDF4 diffusion furnace and diffusions were carried out at 1000°C for 1 minute to produce a diffusion profile similar to an industrial profile (Chapter 5). Following the boron diffusion, samples were allowed to cool to room temperature and placed in a 1:10 HF solution for 2 minutes to remove the boro-silicate-glass (BSG) layer. Following the removal of the BSG, samples underwent an etch in a Nitric acid, Acetic acid, and HF solution to remove the boron-rich-layer as discussed in Chapter 5. The samples were then

taken to a custom built hydrogenation chamber for exposure to atomic hydrogen.

Additional samples were prepared using the same method as above. However, the samples were diced to smaller 1" squares. Samples that were diced to 1" square were used for  $R_{sh}$  testing to determine how the hydrogenation chamber parameters effected the resulting  $R_{sh}$  of the boron diffusion. Clean Si samples that sit for an extended period of time typically begin to grow a thin native oxide. In order to make sure that each sample was free of native oxide, samples were periodically dipped in 1:10 HF:H<sub>2</sub>O solution. Following hydrogenation of these samples, the  $R_{sh}$  was measured using a four point probe tester.

In Figure 6.1 (A) an external view of the custom hydrogenation chamber is shown. The arm out of the front of the chamber is a magnetically coupled transfer arm for placing and removing the sample substrate holder. On top of the chamber sits the turbo pump, which is an Agilent Twistorr 304FS. Figure 6.1 (B) shows a view of the opposite side of the chamber. In Figure 6.1 (B) one can see the Proton On-Site hydrogen generator. This unit functions to turn deionized water into hydrogen gas on demand. Figure 6.1 (C) shows the inside of the hydrogenation chamber. At the bottom of the image is the substrate platform beneath which is the substrate heater. The substrate heater is a solid block of aluminum that has coaxial heaters in one side of the block. Tests were performed to make sure of the temperature uniformity of the block, and all tests confirmed that for a given temperature set point, the block had a uniform temperature. The sample holder sits on top of the substrate heater and can accommodate a full size 6" solar cell. Above the sample platform in Figure 6.1 (C) the tungsten (W) filaments can be seen. The filaments are high purity (>99%) W from Midwest Tungsten Service. They are stretched across the substrate platform 5" above the sample holder platform. The tungsten filaments are secured at their ends with heat resistant standoffs secured to a block of boron nitride. Just above the filaments in Figure 6.1 (C) the gas shower head can be seen. This shower head is a coil of stainless steel pipe that is perforated so as to allow hydrogen gas to be emitted directly over the filaments. The filaments are powered through a DC power supply to produce a temperature compatible with dissociating hydrogen gas into atomic hydrogen. Not pictured are mass flow controllers for nitrogen and hydrogen as well as

the mechanical pump.

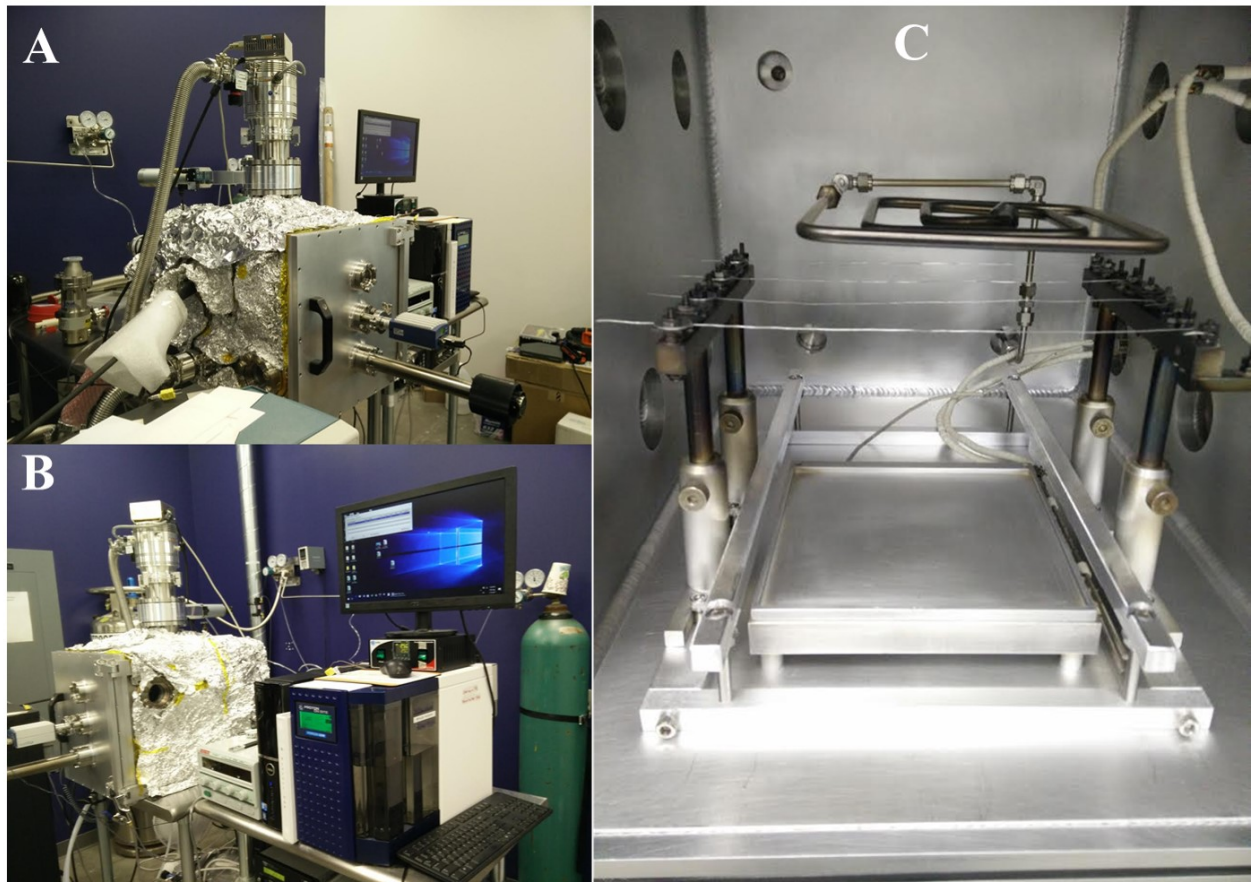


Figure 6.1: Series of images showing the hydrogenation apparatus used in this work to expose boron diffused samples to hydrogenation.

The only process gases used in the hydrogenation chamber are hydrogen. Nitrogen is used as a venting gas to remove samples. The ultimate base pressure was found to be  $8 \times 10^{-7}$  mbar after an overnight pump and baking. There is no load lock on the chamber, so each vent process opens the entire process chamber to atmosphere.

Symmetrically diffused samples were used in order to extract  $J_{0e}$  from PC measurements. In order to hydrogenate both sides of a sample, the sample was first exposed to hydrogen on one side. The system was vented, the sample was removed and the sample was flipped. The back-side hydrogenation was then carried out in an identical fashion. Samples were then removed from the hydrogenation chamber and taken to a cleanroom where the WCT-120 lifetime tester was kept at the time of this study.

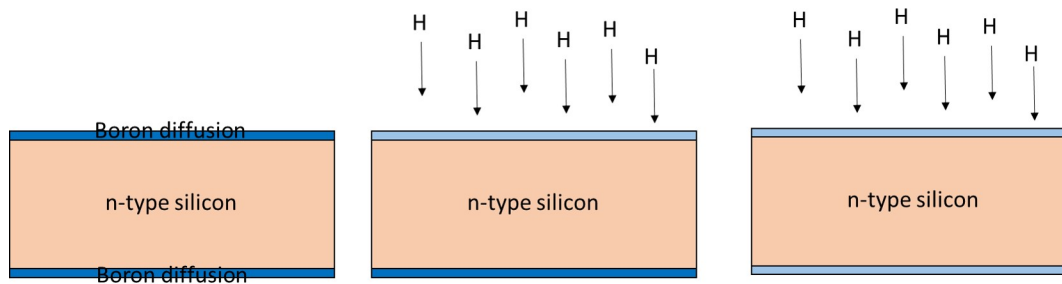


Figure 6.2: From left to right: The step involved in creating a symmetrical diffusion having undergone double sided hydrogenation.

## 6.2 Experiment to Control Sheet Resistance

When first experimenting with the hydrogenation chamber in Figure 6.1, it was necessary to determine how the hydrogenation parameters would effect the sheet resistance of the boron diffusion. It was known from previous experiments in an older chamber that increases hydrogenation times or high filament currents would lead to sheet resistance increases of the boron diffusion. This increase in sheet resistance comes as a result of the electrical deactivation of the hydrogen bonding to the boron and silicon atoms in the lattice [72]. In order to elucidate the behavior of the hydrogenation chamber as it relates to increases in sheet resistance an experimental design was created using the software package JMP 12. The custom design included 40 samples featuring 10 replicate designs and 11 center point runs. The samples were cut from boron diffusions into 1" squares to facilitate a large sample count. The sample count was chosen to be as high as practically possible in an attempt to observe trends that were considered statistically significant. The samples were Cz silicon with a  $\langle 100 \rangle$  surface orientation. Prior to diffusion, the preparation of the samples followed the procedure described in Chapter 5. The center point runs were included in order to determine if any response curvature existed. The response was chosen to be the percent change in sheet resistance. The factors for the experiment as well as their minimum, mid-range, and maximum values is given in Table 6.1.

The factors were chosen based on the practical limits of the equipment used and information from the literature. The minimum temperature was chosen based upon a literature search



Table 6.1: Factors Used in Experimental Design for Sheet Resistance Testing

Factor	Minimum	Middle	Maximum
Substrate Temperature ( $^{\circ}\text{C}$ )	100	150	200
Processing Pressure (Torr)	0.1	1.1	2
Hydrogenation Time (minutes)	0.5	2.75	5
Filament Current (A)	10	11.5	13

that revealed the the boron-hydrogen complex forms for temperatures as low as about  $60^{\circ}\text{C}$ , but an optimum is found at a  $100^{\circ}\text{C}$  [73]. Though the minimum temperature was chosen to be  $100^{\circ}\text{C}$ , it was thought that increases in temperature might create a faster hydrogenation process, therefore a maximum of  $200^{\circ}\text{C}$  was used. The processing pressure was chosen to be at the extremes of what the throttle valve could maintain with the given flow rate of hydrogen gas that the mass flow controller could maintain. This flow rate was chosen to be 100 sccm of hydrogen. There was an interest in performing the hydrogenations in a short time from the perspective of technology implementation. In addition, short processing times could better ensure a faster experimental process. In working the tungsten filaments, it was found that currents much beyond 15 A degraded the tungsten significantly. Therefore, the filament current was kept between 10 A and 13 A. The results of the experimental design were modeled to produce a response surface showing the relationship between temperature and pressure on the hydrogenation process and this is given in Figure 6.3.

The trend that was observed in the response surface model was that with increasing pressure and temperature, a very rapid increase in the diffusion sheet resistance occurs, in this case, by as much as 3000%. While the experimental design focused strictly on what parameters maximized the sheet resistance, the actual target sheet resistance was desired to be much less than what was predicted by the response surface model for high temperatures and pressures. If the sheet resistance of a diffused layer increases too much, this could lead to losses in the solar cell efficiency, due to the resistance of the lateral transport of carriers between gridlines on the top of the solar cell. Therefore, it was desired to only marginally increase the sheet resistance of the diffusion, targeting no more than a 100% increase for  $50 \Omega/\text{sq.}$  diffusion. This experimental design lead the acceptance of a standard set of parameters for temperature and pressure

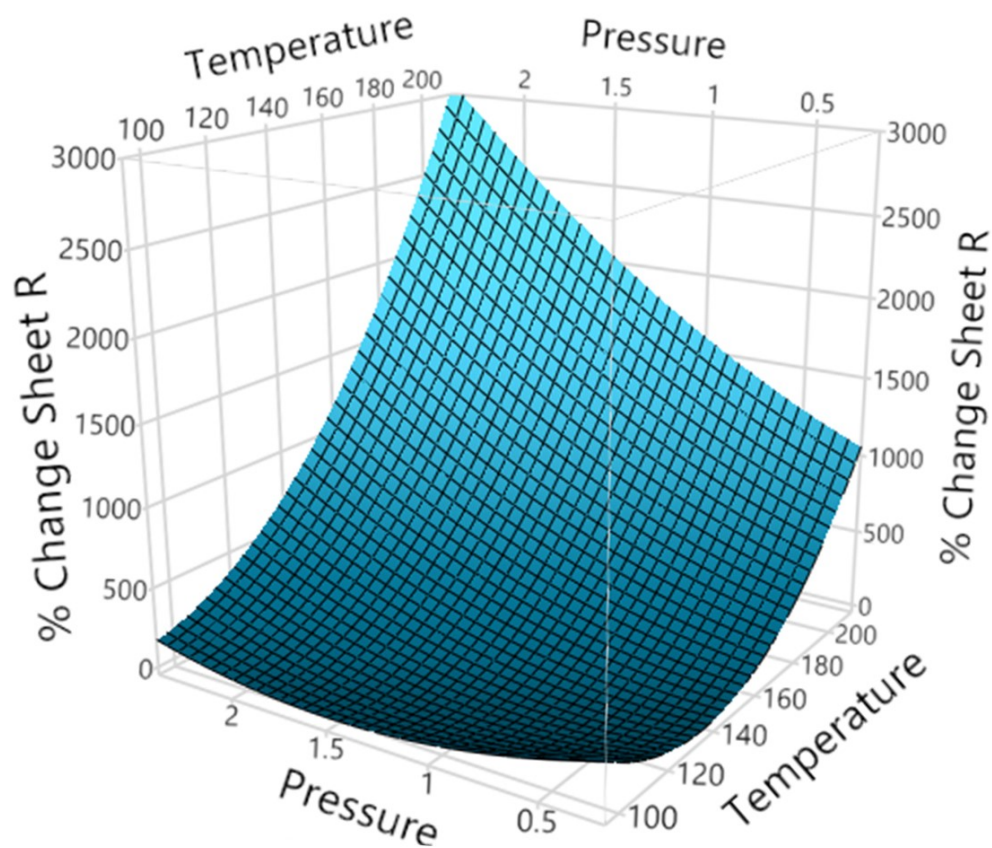


Figure 6.3: Response surface showing relationship between temperature and pressure against sheet resistance percentage change.

at 150°C and 1 Torr pressure. According to the response surface model shown in Figure 6.3, this should keep the change in sheet resistance below 500%. In addition, the filament current was chosen to be even lower than what was used in the experimental design, at 8 A, to make sure the hydrogenation process was controllable for a target sheet resistance.

### 6.3 Initial $J_{0e}$ Measurements

For the initial test of  $J_{0e}$  symmetrical diffusions were prepared in accordance with the method given previously (Experimental Methods). For the first study that was conducted, the experimental design was used to establish hydrogenation parameters at 8A, 150°C, and 1 Torr pressure. Symmetrically diffused samples were hydrogenated on both sides at these parameters for 5 minutes, 15 minutes, and 60 minutes with the results shown in Figure 6.4.

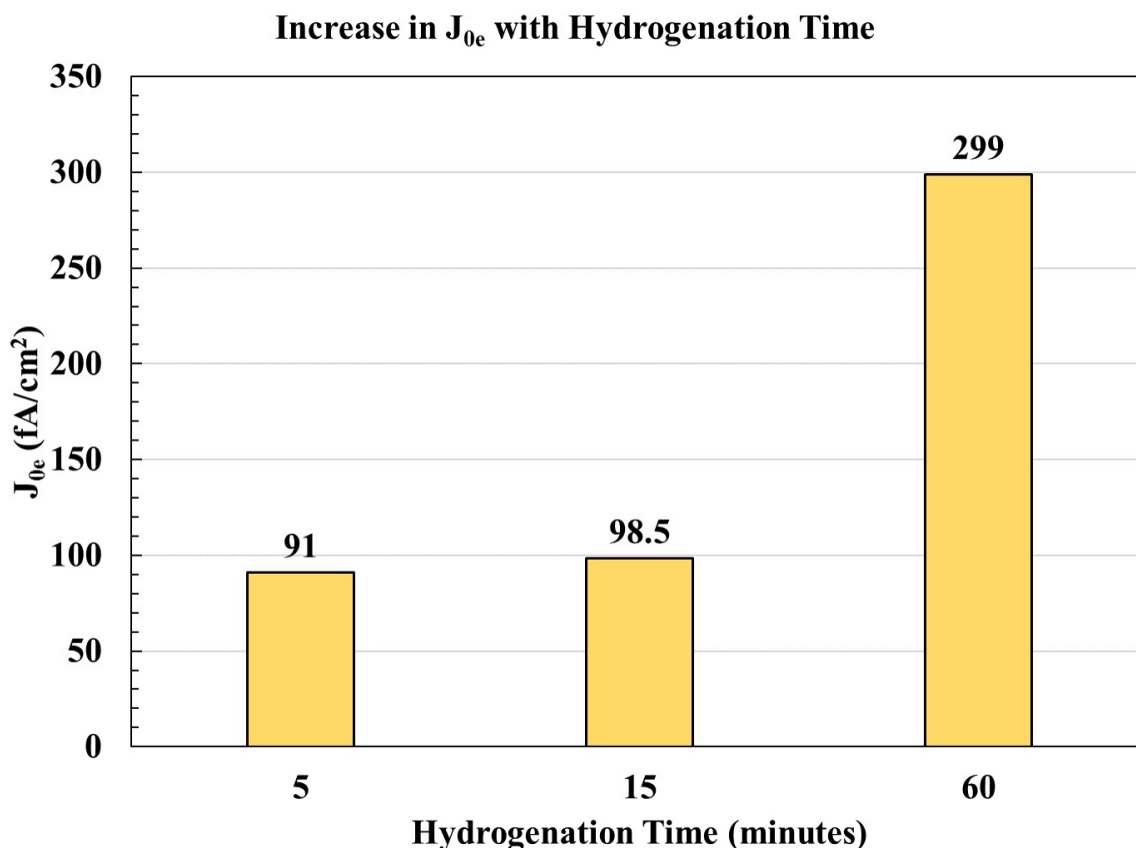


Figure 6.4: Degradation of  $J_{0e}$  with increase hydrogenation time.

Based upon the results in Figure 6.4 it was hypothesized that one of three things was occurring. The first was that the tungsten filaments were producing some form of contamination on the surface of the samples. The second was that the atomic hydrogen was actually creating lattice defects within the silicon or boron diffusion. The third possibility was that the QM was not as effective as passivating the now lightly doped hydrogenated surface. The first hypothesis was developed due a visual observation inside the hydrogenation chamber. After several runs (in excess of a hundred), the sample substrate holder was noted to have the outline of the sample remaining on the substrate holder. This created cause for the concern of W contamination. The second hypothesis was proposed based upon research that showed atomic hydrogen could actually etch the sample surface and insert defects into the crystal lattice [74–76]. The third hypothesis was developed as a result of a publication that showed QM to be less effective than another liquid passivant at passivating lightly doped silicon [49].

It was determined that one of the easiest ways to investigate the various hypotheses was to have secondary ion mass spectroscopy (SIMS) analysis ran on a few samples. SIMS can quantify the relative concentration of atoms of a material with depth into the sample. This is similar to ECV, but SIMS is capable of looking at the total chemical concentration of an element, whereas ECV is limited to only electrically active elements. The result of the SIMS analysis to investigate the impact of W contamination is shown in Figure 6.5.

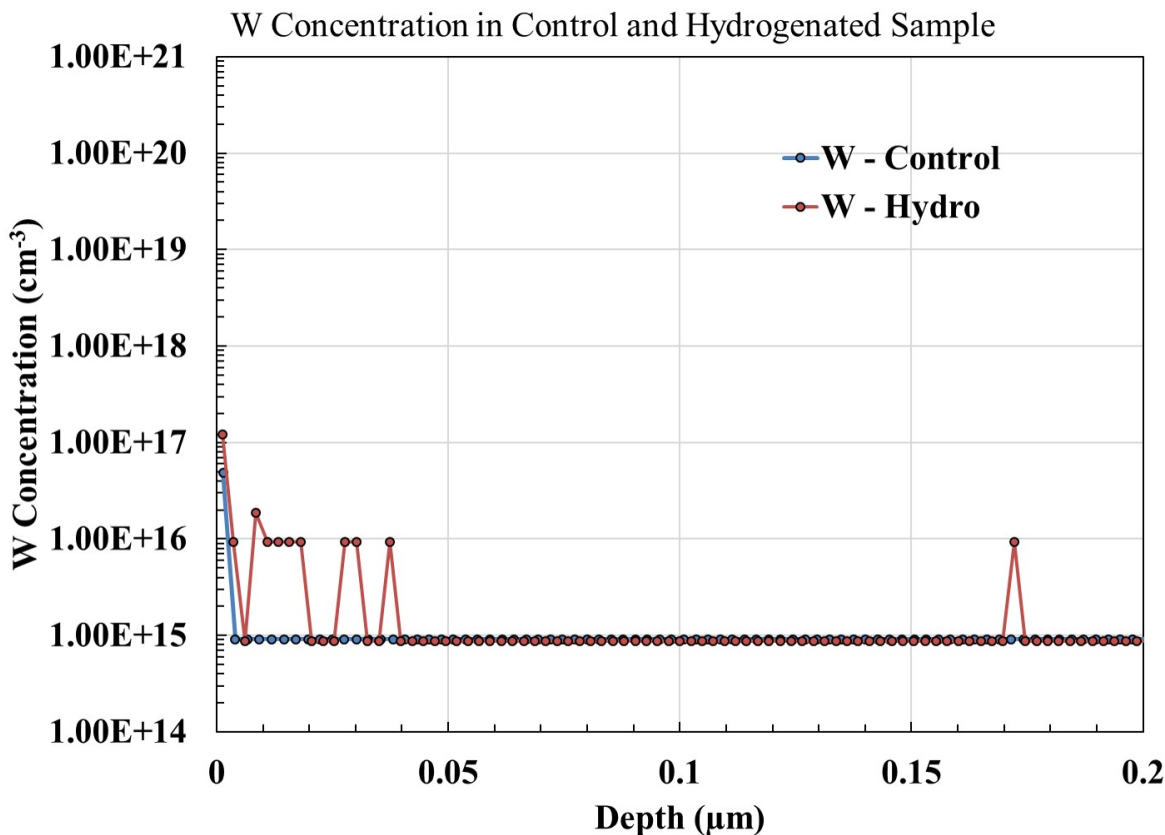


Figure 6.5: SIMS analysis of two samples, a control, and a hydrogenated sample.

The data in Figure 6.5 allowed for the elimination of the idea that W contamination was a problem, at least to some extent. The control sample had not undergone any processing in the hydrogenation chamber, yet, the detected amount of W at the surface was the same as the hydrogenated sample. Both signals show detection of W that is at the noise floor of the sensitivity of the measurement. When the SIMS analysis was performed, samples were also measured for B and H concentration with the results shown in Figure 6.6.

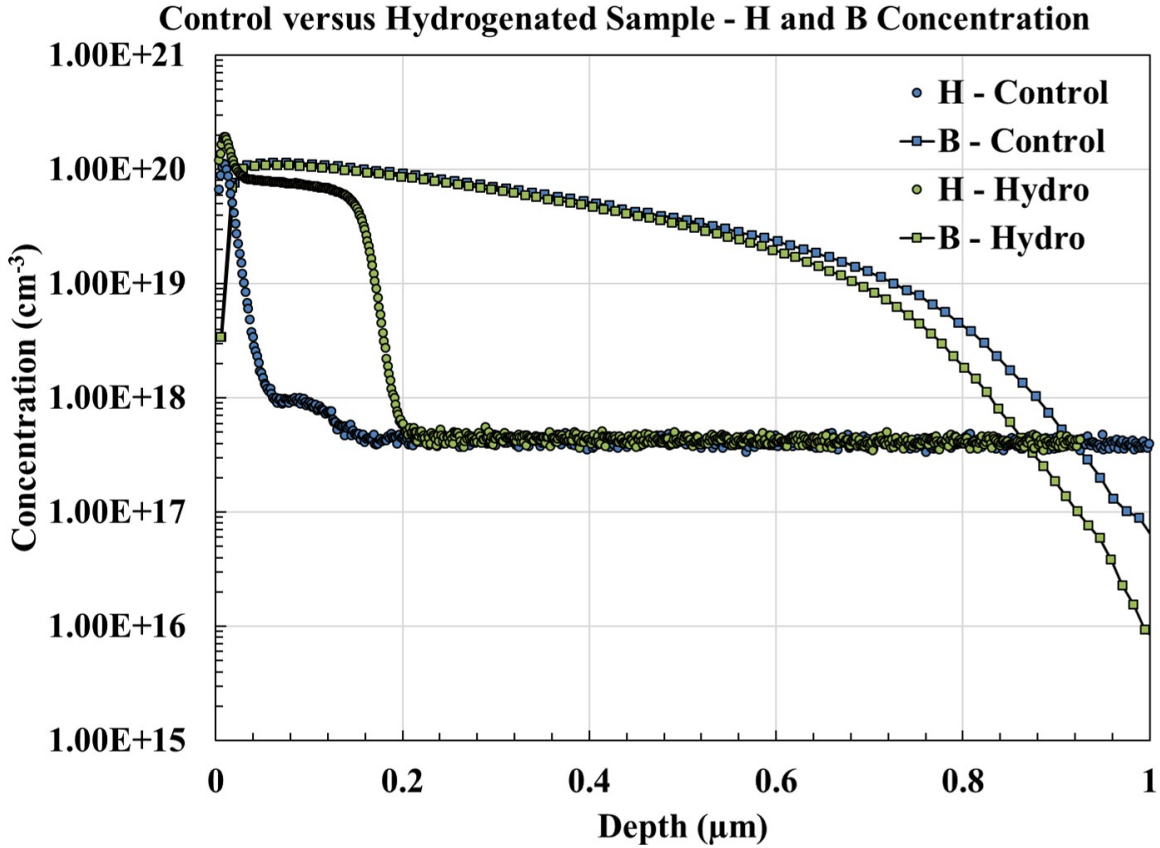


Figure 6.6: Enlarged view SIMS analysis of two samples, a control, and a hydrogenated sample.

The data in Figure 6.6 shows four different curves, for two different samples. One sample was a control sample having a boron diffusion, but not having undergone any processing in the hydrogenation chamber. The control sample is shown to have a boron diffusion (blue squares) that has a peak concentration near  $1 \times 10^{20} \text{ cm}^{-3}$  and decreases with increasing depth into the sample beyond  $1 \mu\text{m}$  in depth. The hydrogenated sample shows a similar boron concentration. The main differences in the two samples, however, is the amount of atomic hydrogen that is measured. The control sample is shown to have some amount of atomic hydrogen within the first  $0.04 \mu\text{m}$  of the sample. This quickly decays down to a value of about  $5 \times 10^{17} \text{ cm}^{-3}$ , where the profile is shown to flatten out. This level is the detection limit of the SIMS analysis for atomic hydrogen due to the background noise of atomic hydrogen. The hydrogenated sample shows a quick peak at the surface exceeding  $1 \times 10^{20} \text{ cm}^{-3}$  in concentration, which then decays down into a flat plateau that extends to almost  $0.2 \mu\text{m}$  within the sample. At this point,

the hydrogen profile quickly drops off to the noise floor of the measurement. This behavior of the atomic hydrogen profile in showing a peak near the surface with a plateau into the sample depth has been reported in the literature previously [77]. This behavior was modeled by Mathiot and shown to relate to the position donor level of the hydrogen atom in boron doped silicon [78].

The hydrogen peak at the surface of the samples shown in Figure 6.7 was observed to be a possible validation for the second hypothesis, that atomic hydrogen might be damaging the sample surface. A blown up plot of the region of interest (the atomic H peak) in Figure 6.7 is shown in Figure 6.8.

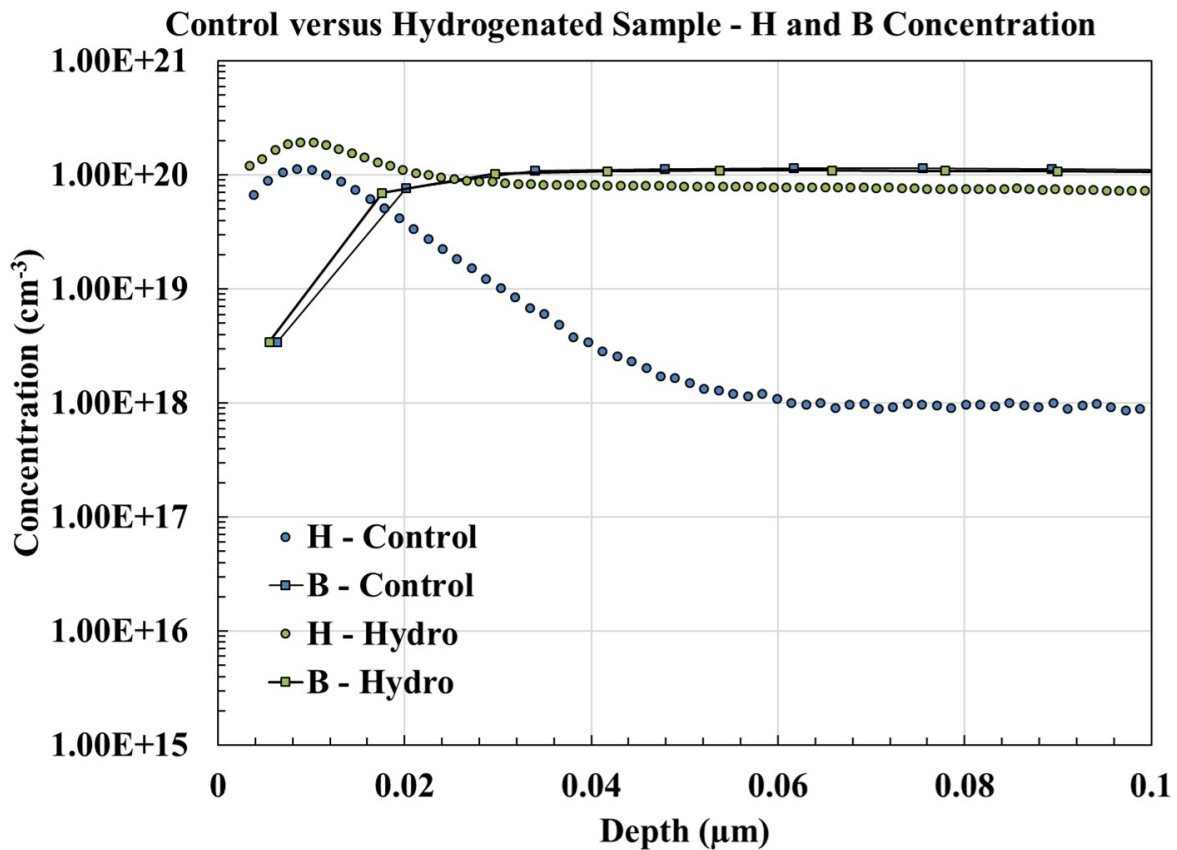


Figure 6.7: SIMS analysis of two samples, a control, and a hydrogenated sample.

The data presented showed evidence that W may not be a problem and that atomic H might be inhibiting the surface passivation of the samples. However, it was decided that an easy way to test to see if something was inhibiting the surface was to develop a slow etching procedure

that could be controlled and allow for the removal of a few tens of nanometers of the sample surface (enough to remove the hydrogen peak shown in Figures 6.6 and 6.7). This etchback process might also act to either etch W from the sample surface (if that were to be the issue) or at least lift it off. It was decided to trial TMAH etches at various temperatures in order to determine an etch rate. The result of the TMAH etch is shown in Figure 6.8.

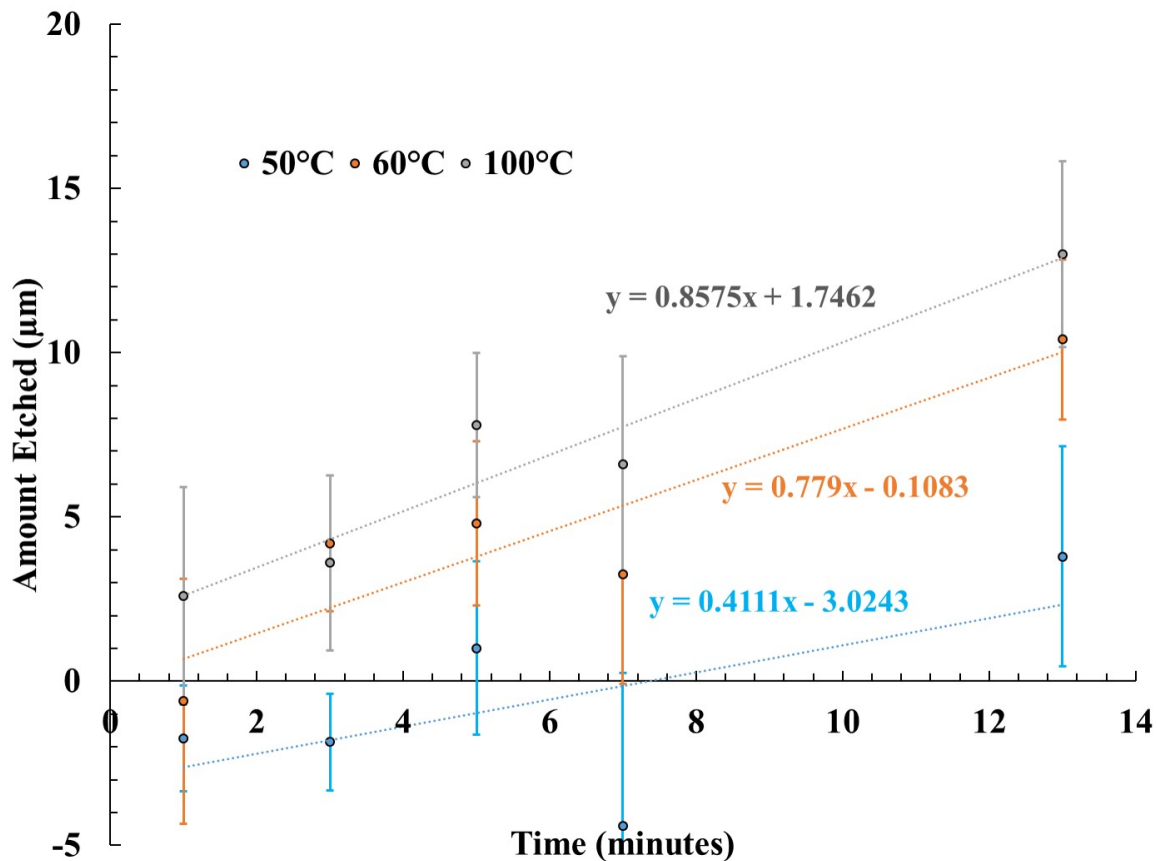


Figure 6.8: SIMS analysis of two samples, a control, and a hydrogenated sample.

The standard TMAH procedure that was developed to remove saw damage on the silicon samples was carried out at near 100°C, so it was decided to start there. The results in Figure 6.8 indicate that that temperature could be used to slow down the TMAH etch rate. An etch temperature of 50°C, was deemed appropriate for controlled removal of tens of nanometers of the boron diffused silicon surface. A 20 second etch might remove around 100 nm of material. With this etch process in hand, it was decided to retriail symmetrical diffusions as a means to prove that atomic hydrogen can lower the  $J_{0e}$  of a boron diffusion.

## 6.4 Hydrogenation Results on Symmetrical Diffusions

The Baseline curve in Figure 6.9 shows the result of measuring the industrial boron diffusion profile (Chapter 5 Figure 5.11) using ECV. This diffusion was applied to multiple different samples and each piece then underwent hydrogenation using 8 A of filament current, a 100 sccm hydrogen flow rate, a substrate temperature of 150°C, and a pressure of 1 Torr of hydrogen for 30 seconds, 1 minute, and 2 minutes as Figure 6.3 depicts.

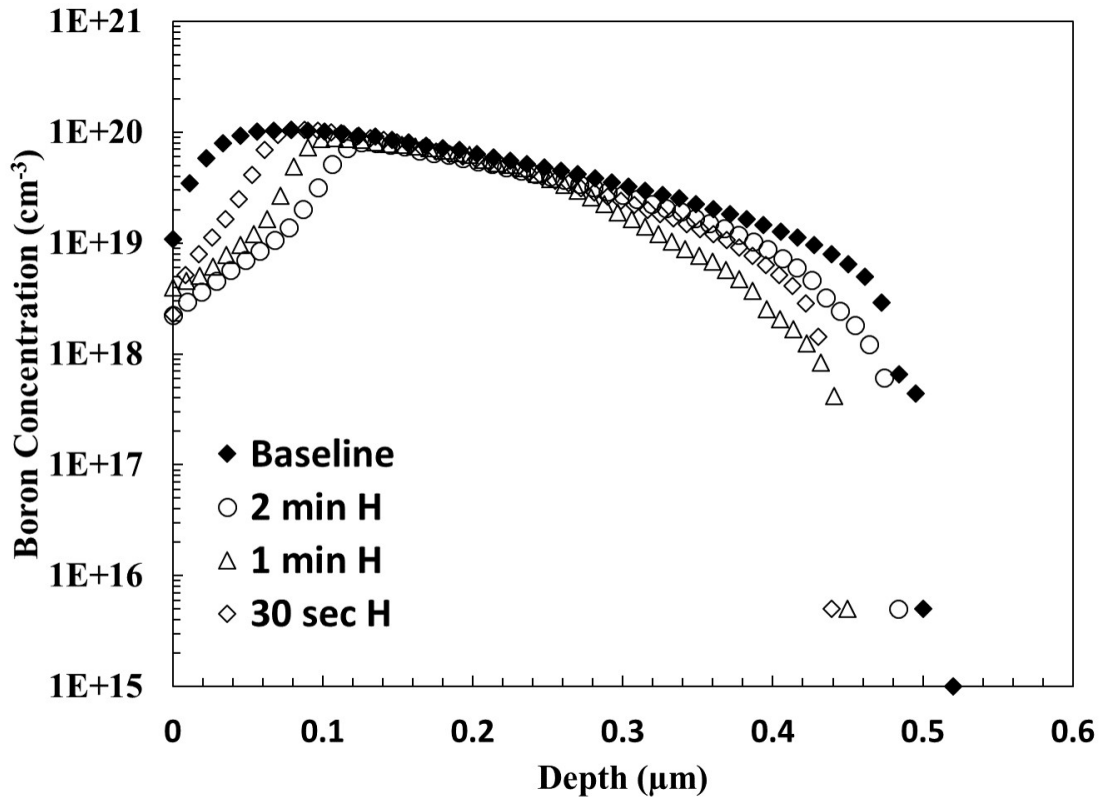


Figure 6.9: Impact of hydrogenation process on industrial boron diffusions.

The hydrogenation process acts to decrease the surface doping concentration of the boron diffusion profiles and also shaves off part of the peak exhibited in the baseline profile. The background doping of the samples here was  $1 \times 10^{15} \text{cm}^{-3}$ , such that the junction depths all occur right around  $0.5 \mu\text{m}$ . While it may appear that the hydrogenation process alters the junction depth, the spread in the data can be attributed to error in the ECV measurement. Each of these profiles was put into EDNA 2 for calculation of its  $J_{0e}$  dependent upon effective SRV.



The output of such calculations is shown in Figure 6.4.

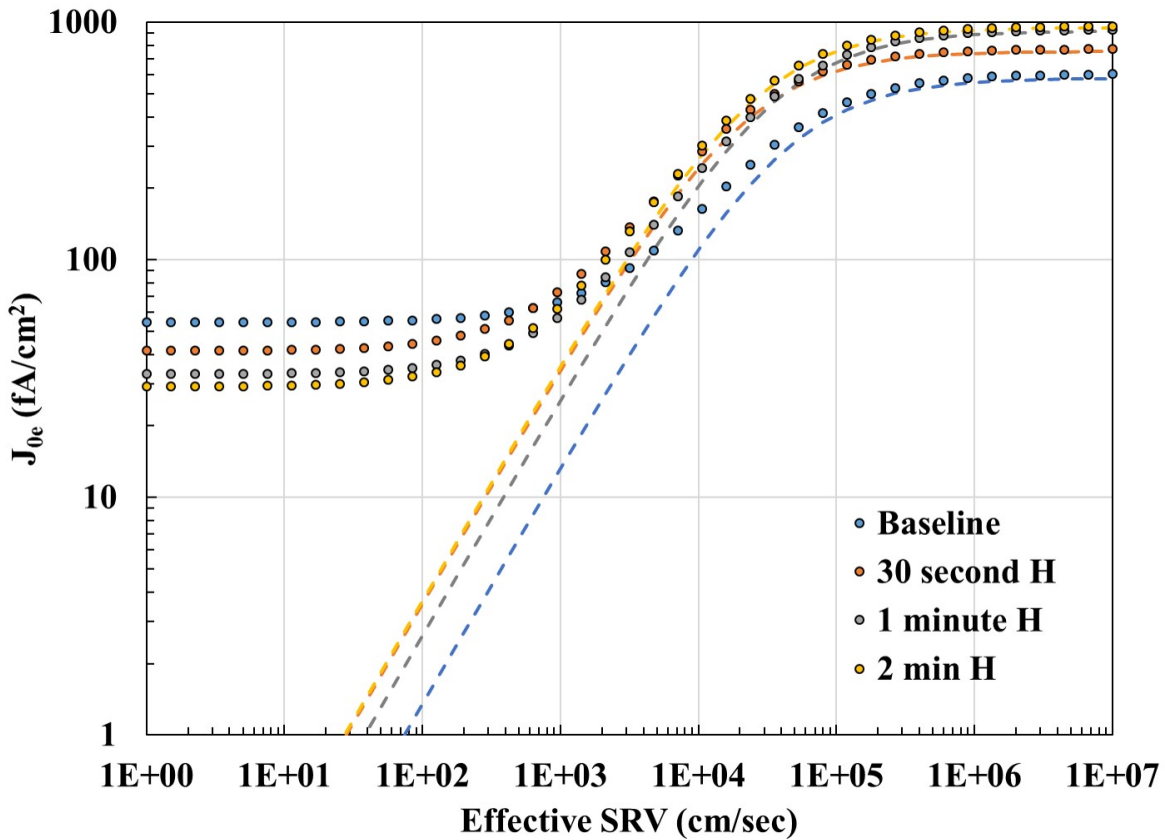


Figure 6.10: EDNA2 simulations of diffusions shown in Figure 6.9.

With increasing hydrogenation time, a trend is seen in the reduction of Auger recombination. This is result of lessening the boron doping concentration of the emitter profiles. The surface recombination component of  $J_{0e}$  is also plotted for each diffusion profile of Figure 6.9 in dashed lines. This calculation predicts that the hydrogenations of the diffusion profiles in Figure 6.3 should result in a lower  $J_{0e}$ . In addition, the hydrogenated emitters tend to become more sensitive to the surface passivation conditions. The hydrogenation results behave not unlike the retrograde profile given by the industrial diffusion that was discussed in Chapter 5. The idea being that the reduction in Auger recombination causes the surface recombination to become a bigger component of the total recombination. Therefore, the sample must be passivated more adequately in order to observe any  $J_{0e}$  reduction due to the hydrogenation process.

To establish that the theory behind the EDNA 2 calculations was sound an experiment was devised wherein multiple types of symmetrical diffused samples were exposed to similiar hydrogenation conditions as those used to produced the profiles of Figure 6.9. The symmetrical diffused samples were partly taken from the data displayed in Chapter 5 for the FZ and P0A9 material. In addition, samples beyond those presented in Chapter 5 were produce. The samples underwent a double sided hydrogenation process according to the flow described in Figure 6.2. The hydrogenation times were allowed to vary from 10 minutes to 20 or 30 minutes, but the other hydrogenation parameters remain fixed. The goal of this experiment was to hydrogenate samples and compare them to non-hydrogenated controls to 1.) determine if atomic hydrogen can reduce  $J_{0e}$  and 2.) to calculate a standard deviation from which it would be possible to tell if the hydrogenation process had an effect greater than the error of measurement.

Samples were measured in QM according to the same procedure used to measure boron diffusions in Chapter 5. The measured  $J_{0e}$  and  $R_{sh}$  is given for each sample that was hydrogenated compared against a control and the data are shown in Figures 6.11 and 6.13. Figures 6.12 and 6.14 show the corresponding measured  $R_{sh}$  values for each of the samples that were hydrogenated.

The averages of all 14 control samples was found to be  $87.43 \pm 21.706$  fA/cm<sup>2</sup> where as the average of all 14 hydrogenated samples was found to be  $60.725 \pm 13.75$  fA/cm<sup>2</sup> for the FZ material. For the Cz samples the control data had a  $J_{0e}$  of  $99.035 \pm 34.56$  fA/cm<sup>2</sup> and the hydrogenated samples had a  $J_{0e}$  of  $62.732 \pm 13.75$  fA/cm<sup>2</sup> It is seen from this data set that the hydrogenation process seems to reduce the overall spread in the measurement data. In addition, the hydrogenation process lowers the  $J_{0e}$  by 36.05% on the FZ material and by 36.6% on the Cz material. The  $R_{sh}$  data is shown in Figure 6.12 for the FZ material and in Figure 6.14 for the Cz material. The variation in the increase in  $R_{sh}$  is because various hydrogenation times were tried in trying to obtain the  $J_{0e}$  reduction. This data proves that atomic hydrogen can reduce the  $J_{0e}$  of a boron diffusion as suggested by the EDNA 2 calculations. However, it is important to note that due to the reduction in Auger recombination, that better surface pas-

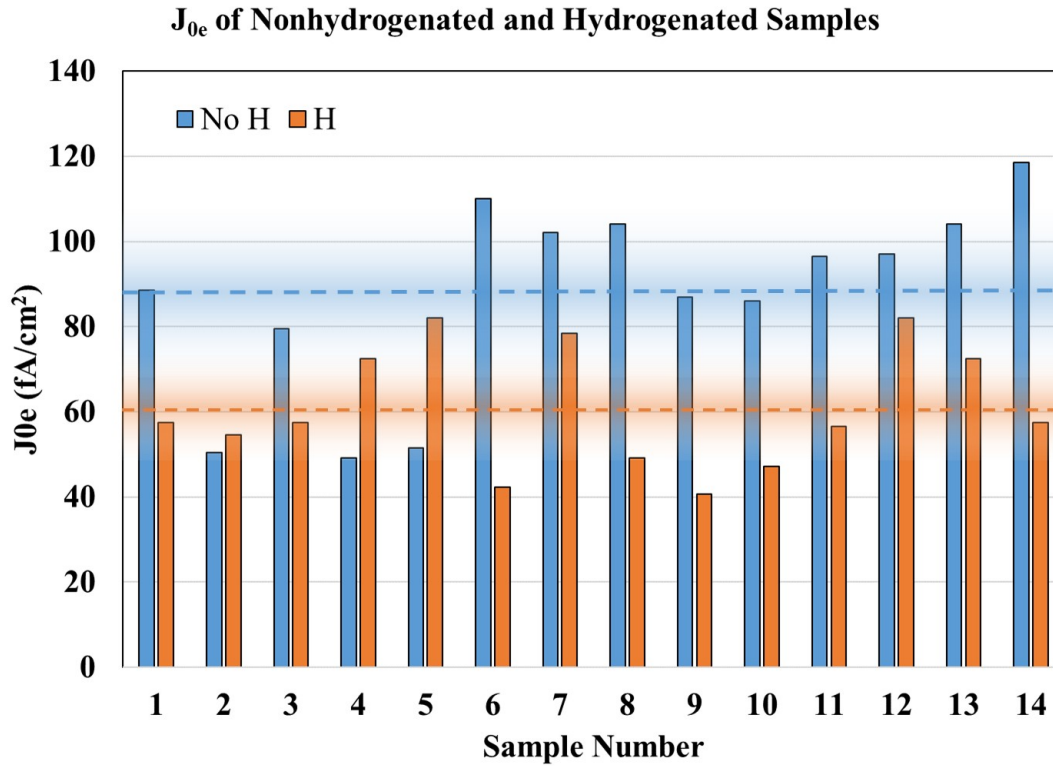


Figure 6.11: Measured  $J_{0e}$  of 14 control samples and hydrogenated samples on FZ silicon (G35XY). Averages for each sample population are shown by horizontal dashed bars.

sivation would be required if implemented into a cell architecture. In order to rule out the possibility that the TMAH etch process was removing the atomic hydrogen from the sample surface, ECV data was collected on control sample, and a sample having undergone hydrogenation, a TMAH etch of the surface, and subsequent dehydrogenation. The data for this is shown in Figure 6.15.

The samples in Figure 6.15 show that after the sample is hydrogenated, the surface doping is reducing and the overall concentration of the profile is reduce to a depth of 200 nm. The sample having undergone a TMAH etch shows the same profile shape as the hydrogenated sample, indicating that it does not remove any substantial amount of the hydrogenated silicon. Finally, after annealing the hydrogenated sample (dehydrogenation) the profile is restored back to its original shape. This data proves that the TMAH etch process does not remove any substantial amount of silicon, thus strengthening the conclusion that atomic hydrogen does, in fact, reduce the  $J_{0e}$  of a boron diffusion. Figure 6.16 shows the measured  $J_{0e}$  of the 1000°C 1

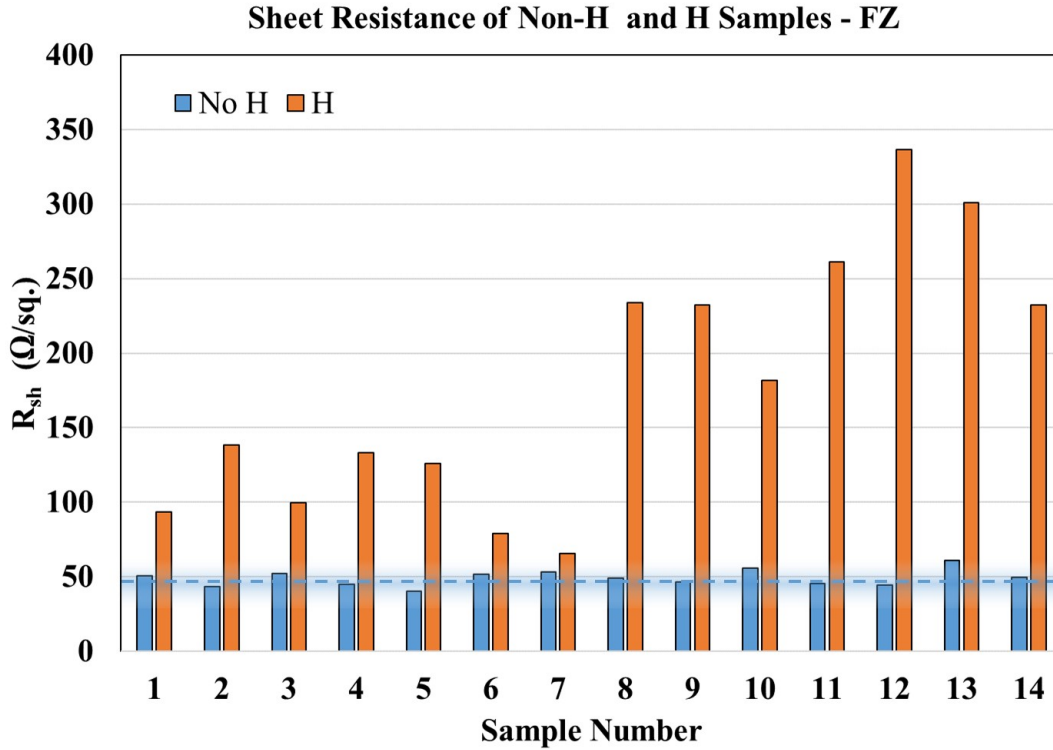


Figure 6.12: Measured  $R_{sh}$  of 14 control samples and hydrogenated samples on FZ silicon (G35XY). Averages for the control sample population are shown by horizontal dashed bars.

minute profile from Chapter 5 plotted against the measured sheet resistance.

This graph was created by taking a standard boron diffusion and repeatedly etching it back in a TMAH etching solution. As the emitter profile is etch, sheet resistance increases as more the profile is removed (becomes shallower) and the surface concentration is reduced. After each etch step, the sample was taken to a FPP tool to measure  $R_{sh}$ , then it was rinsed and cleaned using a Piranha process. Following the Piranha process, the sample was then passivated using QM. Each measurement was performed in a fresh QM solution. The process was repeated until it seemed as though the emitter had been completely etched through. This was repeated on both a hydrogenated sample and a nonhydrogeanted sample.

The intention in the data shown in Figure 6.7 was to capture the fact that the hydrogenated emitter showed reduced  $J_{0e}$  until the hydrogenated portion of the emitter was completely etched away. Then once the hydrogenated portion of the emitter was etched, the measured  $J_{0e}$  should return to measured the same as its non-hydrogenated counterpart. It is typical for

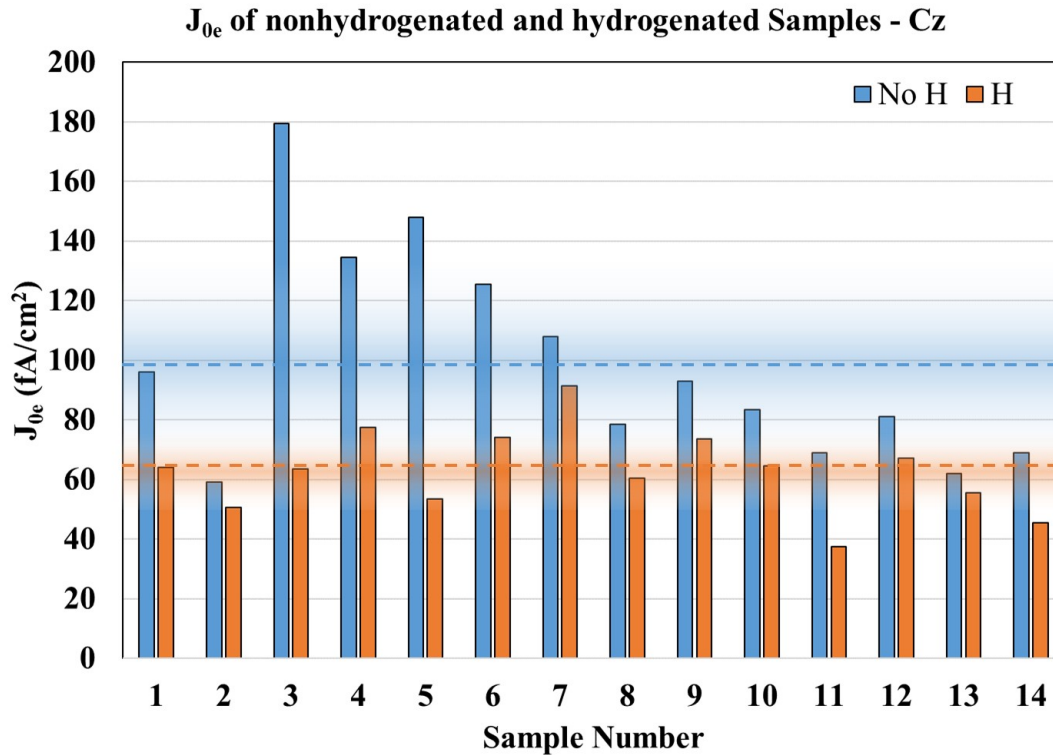


Figure 6.13: Measured  $J_{0e}$  of 14 control samples and hydrogenated samples. Averages for each sample population are shown by horizontal dashed bars.

a diffusion profile to have an exponential decay in the  $J_{0e}$  with increasing sheet resistance especially when the surface recombination velocity is at a fixed value. The SRV would remained fixed in this case assuming since the same type of passivated was used for each measurement. The plot shows that the boron emitter actually has a lower  $J_{0e}$  initially, but then the hydrogenated emitter is shown to out perform until the values decay and converge back to a common average (around  $190\Omega/sq$ awre). However, based upon other measurements presented in this chapter and in chapter 5, it is likely that the data do not show an improvement in this case much beyond the error of measurement. Nonetheless the exponential behavior of  $J_{0e}$  versus  $R_{sh}$  is seen for both emitter profiles.

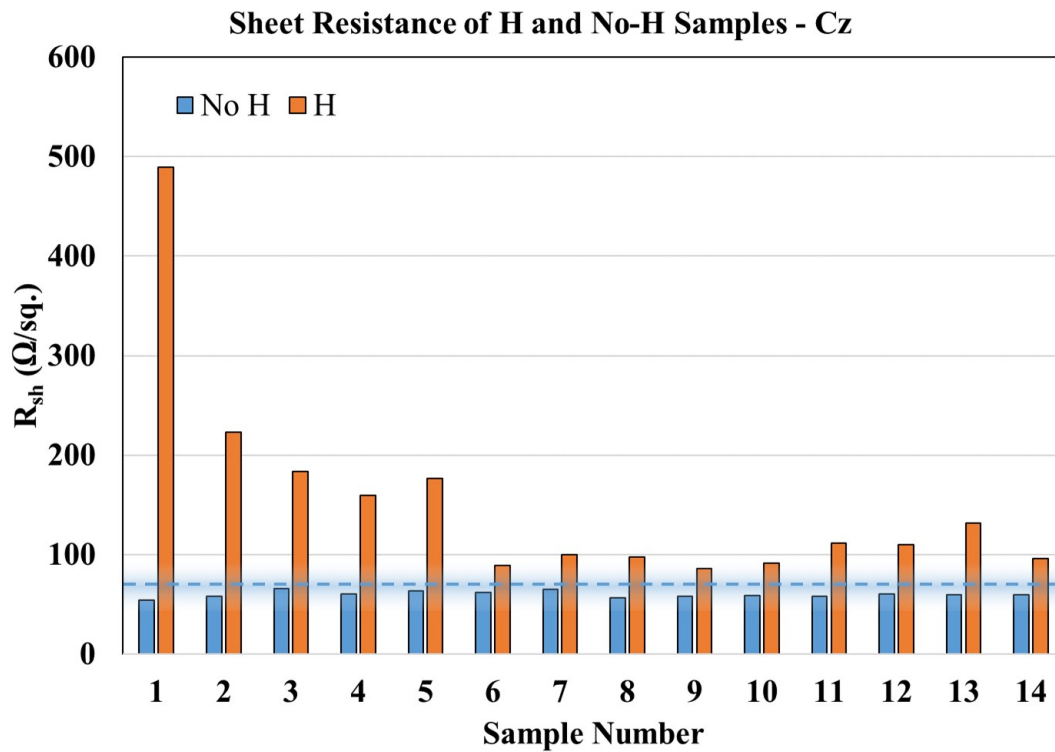


Figure 6.14: Measured  $R_{sh}$  of 14 control samples and hydrogenated samples. Averages for the control sample population are shown by horizontal dashed bars.

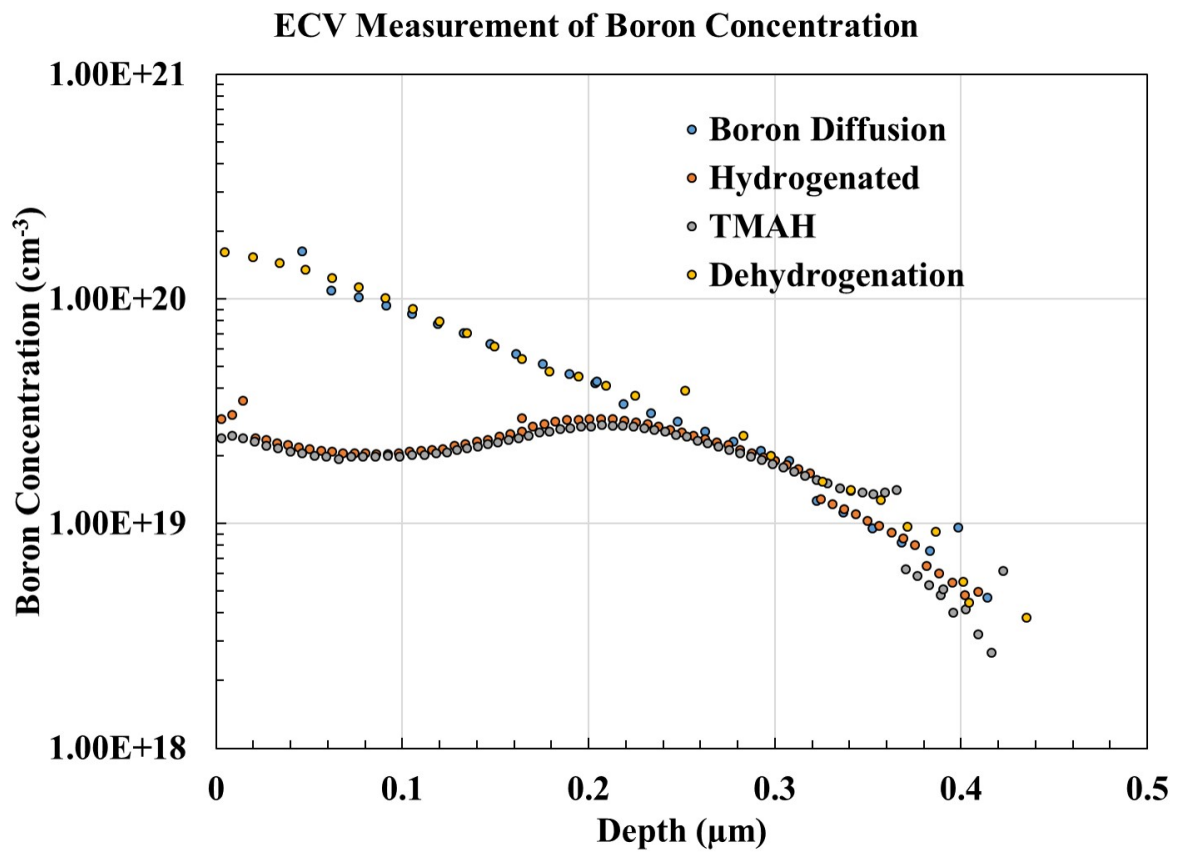


Figure 6.15: Measured  $R_{sh}$  of 16 control samples and hydrogenated samples. Averages for each sample population are shown by horizontal dashed bars.

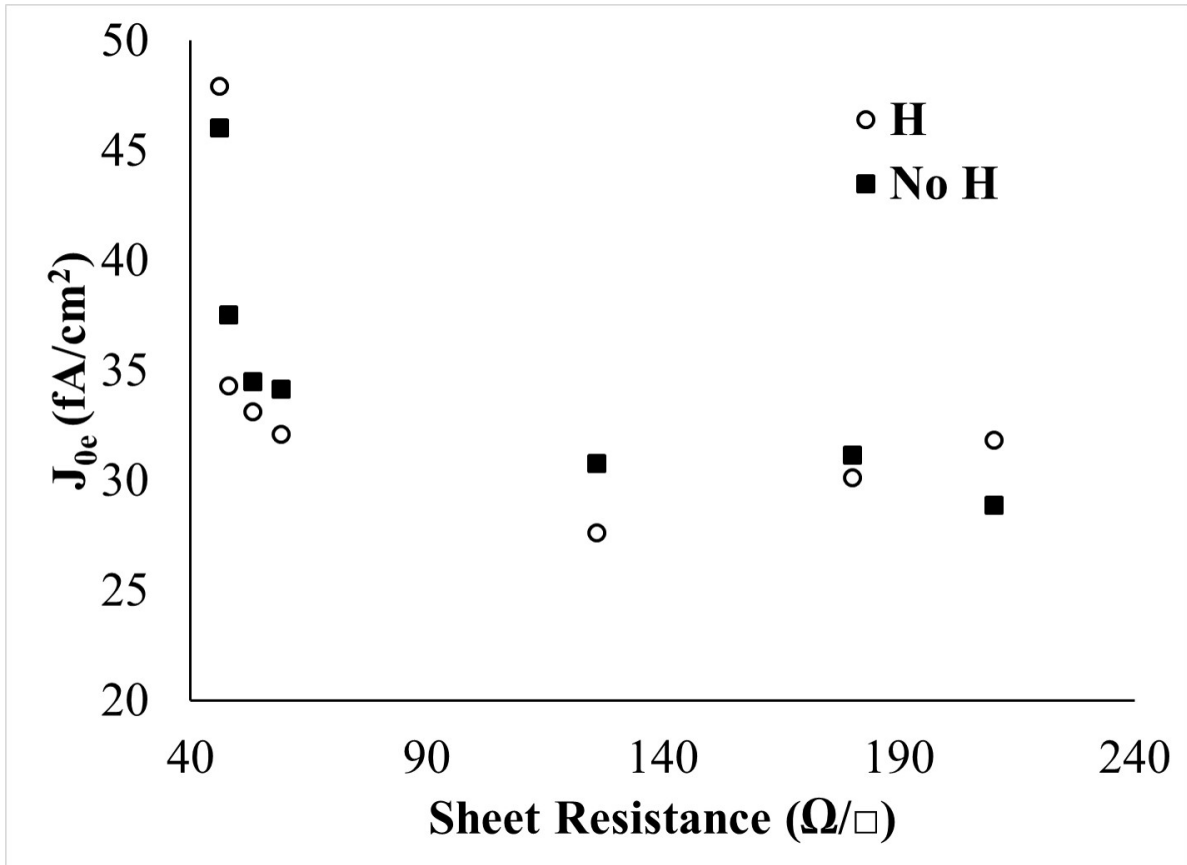


Figure 6.16: Emitter etchback study on a hydrogenated emitter versus a non-hydrogenated emitter.



## 6.5 Summary

This chapter showed the apparatus used to hydrogenate boron diffusions. It was shown that a hydrogenated emitter was capable of about a 36% reduction in the  $J_{0e}$  value of a boron diffusion. This was determined by hydrogenating multiple different sample types. This result proves that a hydrogenated emitter experimentally outperforms a non-hydrogenated counterpart boron diffusion. Thus showing that atomic hydrogen treatment does in fact reduce the  $J_{0e}$  of a boron diffusion.

## Chapter 7

### Device Concept and Fabrication

The demonstration of a  $J_0$  reduction on the hydrogenated boron diffusions warrants the inclusion of a hydrogenated diffusion into real silicon solar cell devices to demonstrate the potential of the technology. The hydrogenation process was carried out on full-size industrial silicon solar cell that were fabricated by the Georgia Institute of Technology. A special process flow was developed to fabricate such cells to accommodate the HSE technology. This chapter gives an overview of such a process and then includes an analysis of the results. Under the correct conditions, efficiency could be enhanced by 0.4% absolute over a baseline process.

#### 7.1 Fabrication Overview of Silicon Solar Cells

The fabrication process flow for the cells used in this dissertation is outlined in Figure 7.1. The wafers that were utilized were Cz, <100> orientation. Prior to cleaning, the cells were put through a KOH solution to form < 111 > pyramids across the surface. After this, a full RCA clean was performed. Next a B implantation was performed into the front side of the cell, followed by a P implantation to form the backside BSF. Implantation processes require the annealing of the implant to activate the dopant atoms. This was performed after both species were implanted into the front and rear. During this annealing process, an oxide is formed on the front and back that acts to passivate the wafer surfaces. A  $SiN_x$  layer is then put down on the backside to provide further passivation.

Following application of the back silicon nitride, contact holes are opened in the back passivation stack to allow for local contacts to be made via silver printing. Next the front gridlines and a full back metal are applied and fired. Hydrogenation is then admitted to the cell through the front oxide layer. The metal gridlines act as a natural mask for the hydrogen, preventing the inactivation of boron beneath the contacts. Next a low temperature silicon nitride is applied to the hydrogenated oxide-coated cell. The  $SiN_x$  deposition is kept below  $220^\circ C$  in order to prevent driving out the boron-hydrogen bonds. Because the  $SiN_x/SiO_x$  stack does not provide sufficient enough passivation to a p-type surface, the cells are then sub-

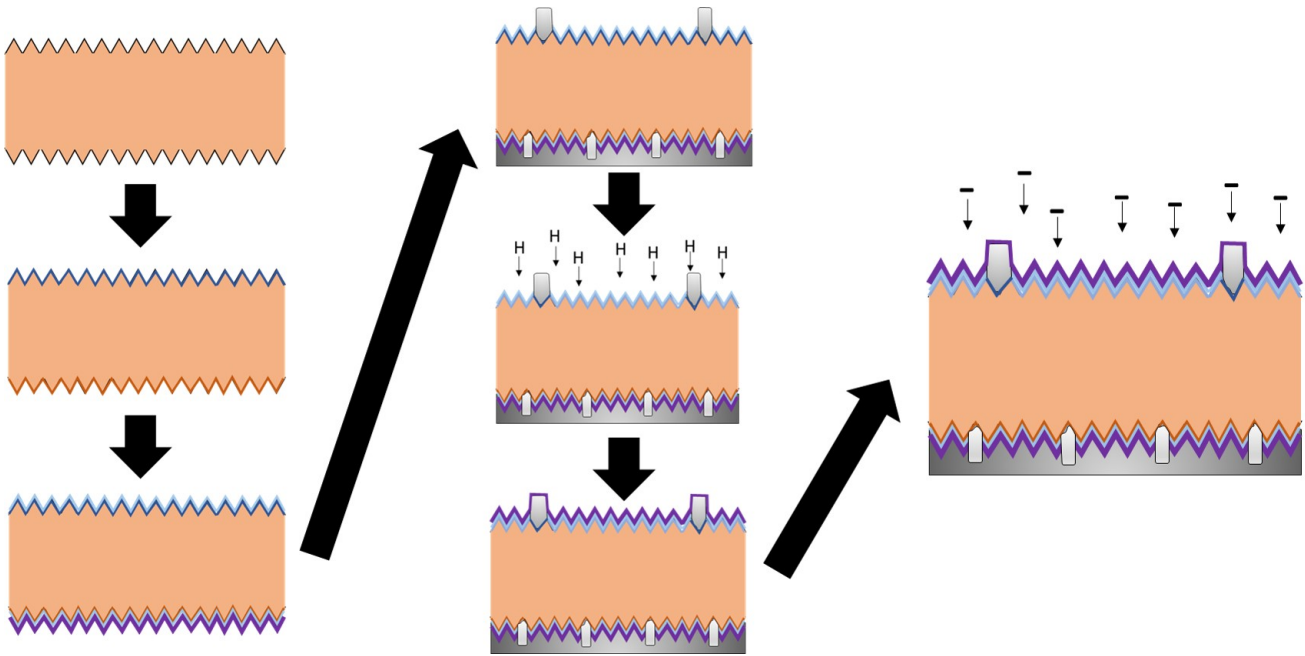


Figure 7.1: Image that shows steps in creating HSE enhanced cells with modified silicon solar cell fabrication process.

jected to a proprietary dielectric charging process that implants negative charges in the  $SiN_x$  layer by changing the  $K+$  centers to  $K-$  centers [79].

### 7.2 Analysis of Hydrogen Selective Emitter On Industrial-Like Solar Cells

Following fabrication, hydrogenation, and dielectric charging, the cells are measured using JV analysis to extract the relevant cell parameters  $V_{oc}$ ,  $J_{sc}$ , FF, and  $\eta$ . Cells were hydrogenated according to a 4-factor experimental design in JMP 12. The 4 factors that were varied included Substrate Temperature, Process Pressure, Filament Current, and Process Time. The design included a total 24 experiments all of which are listed in Table 7.1 with the resulting output data.

A visual depiction of the data presented in Table 7.1 can be found in Figure 7.2 which gives a histogram of the compiled efficiency data for all 24 cells as well as histogram data for cells that had not undergone the hydrogenation process. A summary of the statistics from the histogram is given in Table 7.2

The data in Table 7.2 shows the compiled quantile information for the histogram data of Fig-

Table 7.1: Tabulation of 24 experiments conducted for 4 factor experimental design to test hydrogenation of industrial like silicon solar cells.

Number	Temperature ( $^{\circ}$ C)	Pressure (Torr)	Current (A)	Time (min)	$\eta$
1	100	500	10	120	16.9
2	100	500	12.5	20	17.56
3	100	500	15	75	17.7
4	100	2750	10	20	17.6
5	100	2750	15	120	17.27
6	100	5000	10	75	17.84
7	100	5000	12.5	120	17.9
8	100	5000	15	20	17.77
9	100	5000	15	20	17.94
10	150	500	10	20	18.41
11	150	500	15	120	16.85
12	150	2750	12.5	75	17.91
13	150	2750	12.5	75	17.37
14	150	2750	12.5	75	18.03
15	150	5000	10	120	18.51
16	200	500	10	20	18.57
17	200	500	10	75	18.25
18	200	500	12.5	120	17.64
19	200	500	15	20	17.12
20	200	2750	10	120	18.24
21	200	5000	10	20	18.12
22	200	5000	15	20	18.32
23	200	5000	15	120	16.89
24	200	5000	15	120	17.7

Table 7.2: Tabular summary of maximum, median, and minimum values obtained form histogram analysis of data in Table 7.1.

Quantile %	Quantile Label	$\eta$ - H	$\eta$ Control
100	Maximum	18.57	18.21
50	Median	17.805	18.04
0	Minimum	16.85	17.8

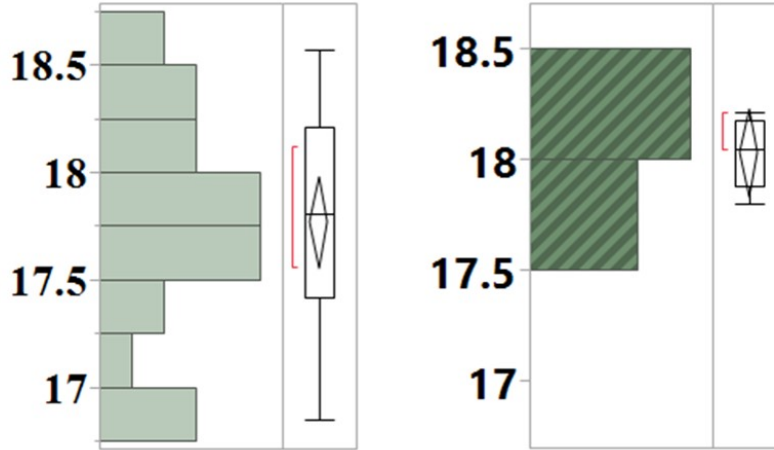


Figure 7.2: (Left) Histogram analysis for  $N = 24$  total cells that had undergone the cell fabrication process of Figure 7.1. (Right) Population,  $N = 5$ , of control cells.

Figure 7.2. The  $\eta$ -H column gives the efficiency values measured after the entire fabrication process of Figure 7.1 was carried out on  $N = 24$  cells. The  $\eta$  Control column gives the same data for a limited number,  $N = 5$ , cells. The control cells went through the entire process of Figure 7.1 with the exception of the hydrogenation step to form the selective emitter.

The histogram of Figure 7.2 shows a distinct difference in the distribution that was obtained. The hydrogenation process gives increases in the variance of the data set and creates something of a normal distribution. The control data has a much tighter variance. The only difference between the two fabrication process is that of the hydrogenation process. This does not mean that the hydrogenation process possesses a large variance. The fact that there is such a wide variance has to do with the fact that several different combinations of hydrogenation factors were carried out from experiment to experiment (see Table 7.1). In fact, a narrow distribution similar to the control histogram would be indicative of a non-effect from the hydrogenation, which should not be the case given the  $J_0$  results presented in Chapter 6. A key takeaway from this data is that the maximum hydrogenated cell is nearly 0.4% better in efficiency than that of the control population. However, some caution should be added to this as a conclusion, given the limited number of cells in the control population. Nonetheless, the data seems to indicate that, under the proper hydrogenation conditions, a 0.4% enhancement in cell efficiency can be had.

### 7.2.1 JV Analysis

To show the behavior of the JV analysis throughout the processing steps listed in Figure 7.1, a singular sample of the cell data from Table 7.2 was taken. The result of the light JV measurement from the cell at different processing steps is given in 7.3. The "OoB" label indicates an "Out-of-Box" condition, or the condition of the cell with only oxide passivation at the front side. The Post-H data shows the same JV analysis carried out on the cell but after the hydrogenation process. Note that only a small boost to  $J_{sc}$  and  $V_{oc}$  is given. The oxide passivation tends to inhibit the ability of the hydrogenation to give a larger boost due to the lack of surface passivation. Following the nitride deposition and charging process, the cell gains in both  $J_{sc}$  and  $V_{oc}$ . The gain in  $J_{sc}$  is largely thought to come from the nitride deposition. The boost to  $V_{oc}$  and even, to some extent  $J_{sc}$ , comes from a reduction of the  $J_{0e}$  due to the hydrogen shaping of the boron doped region at the front of the cell.

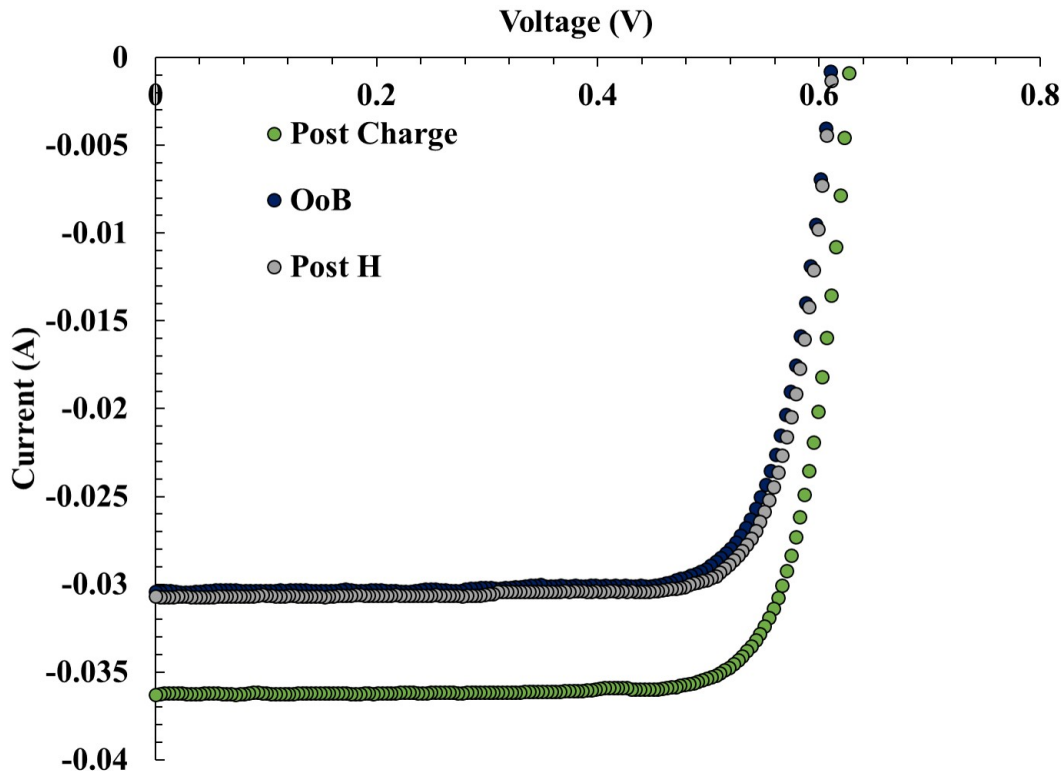


Figure 7.3: Light JV curves collected on full size cells with just thermal oxide passivation (OoB), right after the hydrogenation process (Post H), and following SiNx deposition and di-electric charging (Post Charge).

Figure 7.4 shows a comparison of the JV curves of the best hydrogenated cell and the best control cell. The scale makes it a bit difficult to observe, however, the hydrogenated cell has a slight boost to  $J_{sc}$  and  $V_{oc}$ , as expected.

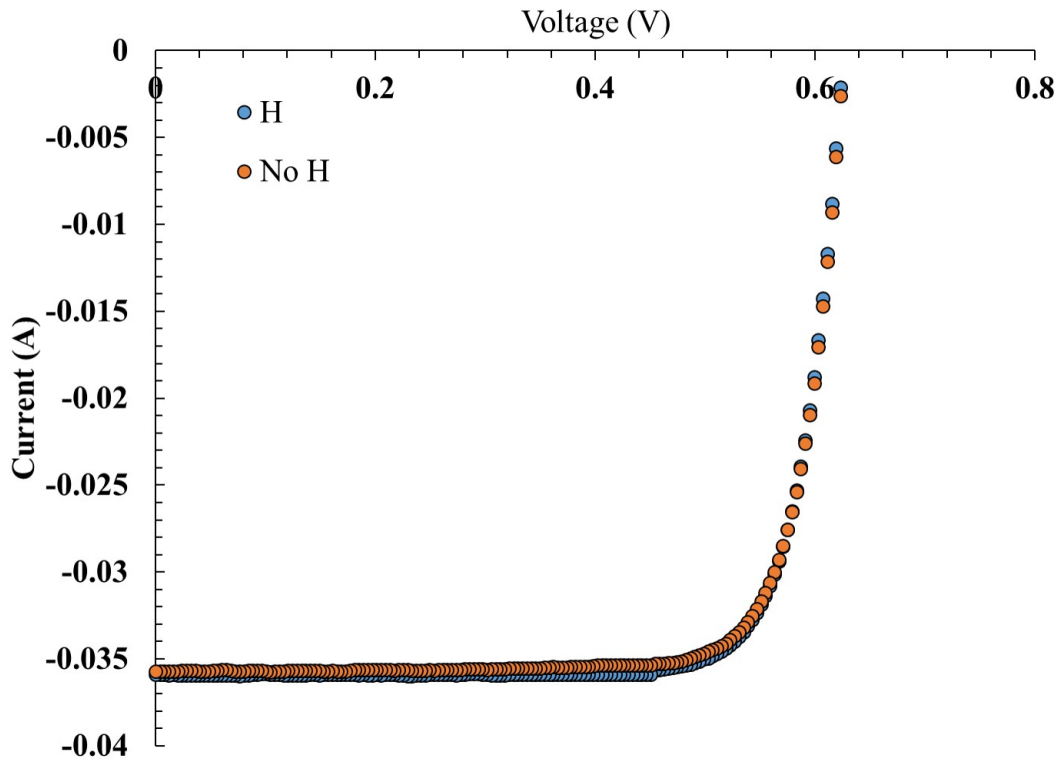


Figure 7.4: The highest efficiency hydrogenated cell versus the highest efficiency control cell. Though not visible because of the scale of the graph, the  $V_{oc}$  of the H cell is 2 mV greater than that of the Non-H cell.

The JV data given in Figures 7.3 and 7.4 do not show dramatic gains in the efficiency or other cell parameter. It should be noted that the hydrogenation conditions presented, do not represent the optimum. Under the correct conditions the cell can lose efficiency as shown in Table 7.2, but, according to the study presented herein, an absolute gain of 0.4% can be had over a control cell with the hydrogenation process.

### 7.2.2 EQE

An unknown contact issue prevented the cells of Table 7.2 from being able to be measured using EQE. However, a different set of research cells was chosen to exemplify the effect of the

atomic hydrogen process on the cell EQE. Shown in Figure 7.5 are the EQE curves of several oxide-coated solar cells (having no  $SiN_x$  coating).

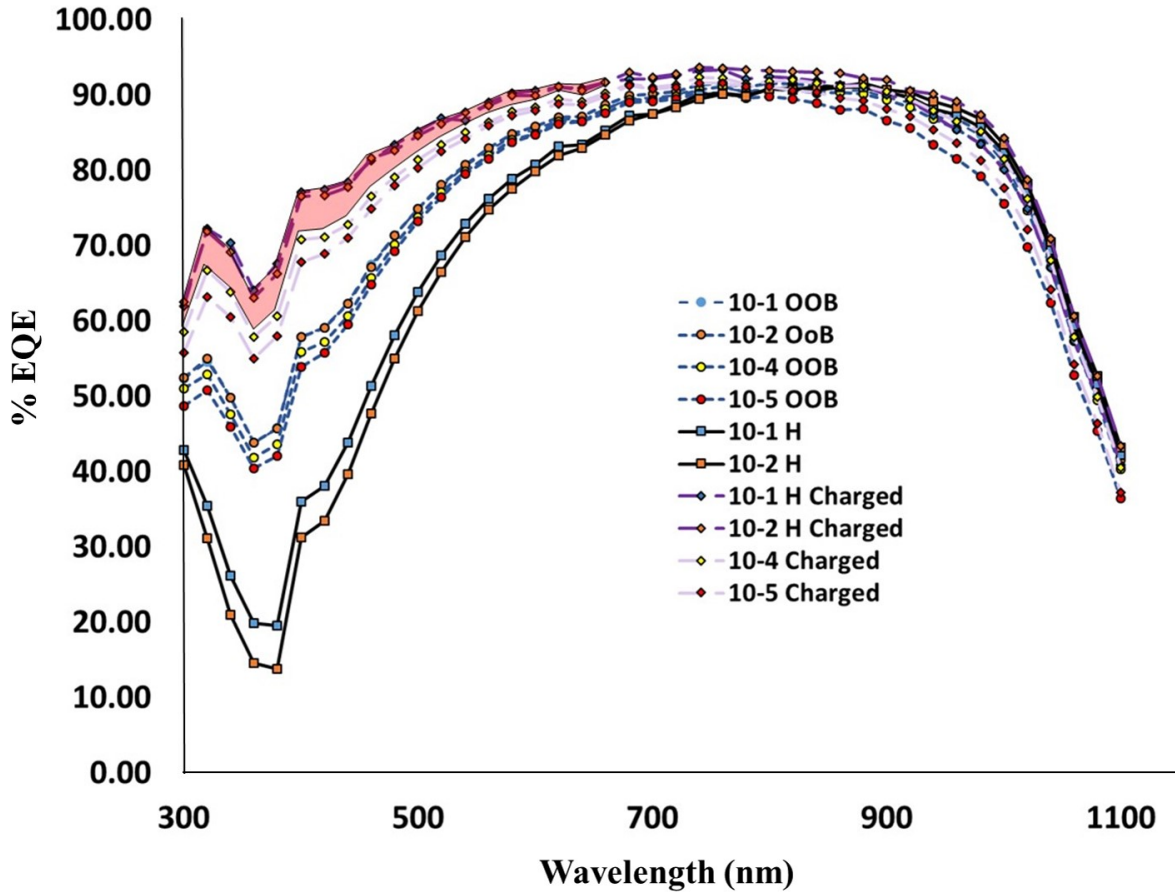


Figure 7.5: EQE plots of small oxide cells that were passivated with thermal oxide, put through the hydrogenation process, and then charged with negative charges. The red highlighting indicates the increase in short wavelength response obtained from the selective emitter structure.

The EQE data of four different cells are shown in Figure 7.5, 10-1, 10-2, 10-4, and 10-5. The OoB condition for all of the cells shows a tight clustering of the EQE data, indicating there is little processing difference between the four the cells. 10-1 and 10-2 were subjected to a hydrogenation process and the EQE data measured after this process is given by the curves labeled “10-1 H” and “10-2 H”. The EQE decreases in the range from 300 nm to 700 nm, from an average of about 50% to less than 40%, and as low as 10% at around 400 nm. The reason for this is because of the poor quality passivation of the oxide layer in conjunction with the lighter doping in the near surface region. The hydrogenated cells, 10-1 and 10-2, were charged



with a negative charge, along with 10-4 and 10-5, to act as controls. The EQE plots of Figure 7.5 show the results, with the red shading indicating the gain experienced in cells 10-1 and 10-2 due to the hydrogenation process. This enhancement of the blue wavelength EQE is consistent with the  $J_{sc}$  and  $V_{oc}$  boost presented in Figures 7.3 and 7.4.

### 7.3 Summary

This chapter showed the application of atomic hydrogen to an industrial like silicon solar cell fabrication process. The atomic hydrogen treatment was required to be enhanced by use of a negative dielectric charging to bolster field effect passivation. The best result obtained was 0.4% boost with a hydrogenated cell over a control cell. The increase in efficiency comes from the reduction in  $J_{0e}$  due to the inactivation of majority carriers lessening the effect of Auger recombination. This can only be the case with high enough quality surface passivation. These results demonstrate that a hydrogenated selective emitter, under the right conditions, can provide an enhancement to a cell process by post-diffusion shaping of the boron diffused/implant region of a device.

## Chapter 8

### Conclusions and Future Work

In this chapter, conclusions and future work are laid out to encourage additional research in this topic area.

One remaining obstacle for successful implementation of the HSE process into cell manufacturing is to show that atomic hydrogen can penetrate silicon nitride layers. Not only must the atomic hydrogen penetrate the silicon nitride layers, but it must do so without damaging either the SiO/Si interface or the bonds in the emitter lattice. A promising way to potentially drive atomic hydrogen through the silicon nitride ARC is with a biasing method. In such a method, atomic hydrogen is driven by an electric field through the ARC into the emitter.

This is akin to ion implantation, except the energy levels in this case will be lower. Though the work in this dissertation shows that atomic hydrogen can have a beneficial impact on a p+ emitter layer, it is necessary to combine the hydrogenated emitter with good passivation. This needs to be accomplished without altering the cell architecture for the largest cell efficiency gains to be had.

The recombination current density was shown to be reduced through comparison to control samples with two different types of silicon. The contained work could benefit from additional experimentation to find the maximum reduction that could be obtained. In addition, for work on real silicon solar cells, it will be necessary to explore the hydrogenation of oxide layers on silicon, and oxide/nitride stacks. Oxide/nitride passivation/ARC stacks are the most common layers on the front of silicon solar cells and, the nitride at least, is a barrier to hydrogen diffusion. Therefore, it is necessary to explore ways to either drive the atomic hydrogen through the nitride/oxide stack to create a selective emitter. A suggested method of doing this is to use biasing to drive the hydrogen inward through the nitride layer. Care must be taken to evaluate the electron and optical properties of the passivation layers following such a process though, it is possible that biasing through these layers could alter their material properties for the worse (or perhaps the better). Another viable option might be the use of a controlled laser rastered over the surface of the cell to release atomic hydrogen from the front silicon ni-

tride layer on a solar cell. This however may pose a significant challenge as the temperature release from the nitride layer maybe different than that required to bond atomic hydrogen with boron.

Successful introduction of atomic hydrogen into the front boron emitter region of a solar cell through the oxide and nitride layers will allow for implementation as the last step in industrial fabrication.

## Bibliography

- [1] J. Benick, B. Hoex, G. Dingemans, W.M.M. Kessels, A. Richter, M. Hermle, S. W. Glunz, Fraunhofer Institute for Solar Energy Systems (ISE), Heidenhofstrasse, D-79110 Freiburg, and Germany. High-efficiency n-type silicon solar cells with front side boron emitter. In *24th European Photovoltaic Solar Energy Conference, 21-25 September 2009, Hamburg, Germany*, 2009.
- [2] International technology roadmap for photovoltaic (itrpv) 2015 results. Technical Report Seventh Edition and March, 2016.
- [3] Jiun-Hong Lai, Ajay Upadhyaya, Saptharishi Ramanathan, Arnab Das, Keith Tate, Vijaykumar Upadhyaya, Aditya Kapoor, Chia-Wei Chen, and Ajeet Rohatgi. High-efficiency large-area rear passivated silicon solar cells with local al-BSF and screen-printed contacts. *IEEE Journal of Photovoltaics*, 1(1):16–21, jul 2011.
- [4] Jan Schmidt and Andreas Cuevas. Electronic properties of light-induced recombination centers in boron-doped czochralski silicon. *J. Appl. Phys.*, 86(6):3175, 1999.
- [5] Andrew W. Blakers, Aihua Wang, Adele M. Milne, Jianhua Zhao, and Martin A. Green. 22.8% efficient silicon solar cell. *Appl. Phys. Lett.*, 55(13):1363, 1989.
- [6] Stuart R. Wenham Malcolm D. Abbott et. al. Brett J. Hallam, Phill G. Hamer. Advanced bulk and defect passivation and techniques for and silicon solar and cells. 2013.
- [7] P.J. Cousins and J.E. Cotter. The influence of diffusion-induced dislocations on high efficiency silicon solar cells. *IEEE Trans. Electron Devices*, 53(3):457–464, mar 2006.
- [8] Dr. Joris Libal & Dr. Radovan Kopecek. N-type silicon solar cell technology: ready for take off? Online, March 2015.
- [9] Joris Libal Radovan Kopecek. Switch from p to n, June 2012.
- [10] David D. Smith, Peter J. Cousins, Asnat Masad, Staffan Westerberg, Michael Defensor, Reynold, Ilaw, Tim Dennis, Rhea Daquin, Neil Bergstrom, Arjelene Leygo, Xi Zhu, Bennet Meyers, and Ben. Sunpowers maxeon gen iii solar cell: High efficiency and energy yield. *IEEE*, 4799.
- [11] Mikio Taguchi, Ayumu Yano, Satoshi Tohoda, Kenta Matsuyama, Yuya Nakamura, Takeshi Nishiwaki, Kazunori Fujita, and Eiji Maruyama. 24.7 % record efficiency HIT solar cell on thin silicon wafer. *IEEE Journal of Photovoltaics*, 4(1):96–99, jan 2014.
- [12] Ronald A. Sinton Richard R. King, Peter E. Gruenbaum and Richard M. Swanson. Passivated emitter in silicon solar cells. *IEEE*, 1990.
- [13] Mohammad Ziaur Rahman. Status of selective emitter for p-type c-si solar cells. *Optics and Photonics Journal*, 2012.
- [14] Ulrich Jger, Mahir Okanovic, Matthias Hrtheis, Andreas Grohe, Ralf Preu, Fraunhofer Institute for Solar Energy Systems (ISE), Heidenhofstrasse, 79110 Freiburg i. Brsg, and Germany. Selective emitter by laser doping from phosphosilicate glass. In *Presented at the 24th European PV Solar Energy Conference and Exhibition, 21-25 September 2009, Hamburg, Germany*, 2009.

- [15] Homer Antoniadis, F. Jiang, W. Shan, and Y. Liu. All screen printed mass produced silicon ink selective emitter solar cells. *IEEE*, 4244.
- [16] Seth Shumate. *Top-Down Aluminum Induced Crystallization for Photovoltaics*. PhD thesis, University of Arkansas, 2014.
- [17] A. Breitschwerdt C. P. Herrero, M. Stutzmann and P.V. Santos. Trap-limited hydrogen diffusion in doped silicon. 1990.
- [18] Martin A. Green. *Solar Cells: Operating Principles, Technology, and System Applications*. PrenPrentice Hall., 1982.
- [19] Christiana B. Honsberg and Stuart Bowden. Standard solar spectra. Online, 2016.
- [20] Christian Gueymard. Simple model of the atompsheric radiative transfer of sunshine. Online, November 2016.
- [21] M. A. Green. Self-consistent optical pparameter of intrinsic silicon at 300k including temperature coefficients. *Solar Energy Materials and Solar Cells*, 2008.
- [22] Christian Honsberg and Stuart Bowden. Optical properties of silicon. Online, November 2016. <http://pveducation.org/pvcdrom/materials/optical-properties-of-silicon>.
- [23] Pietro Altermatt. Altermatt’s lectures on photovoltaics. Online, November 2016. available at <https://www2.pvlighthouse.com.au/resources/courses/altermatt/altermatt>
- [24] Thorsten Trupke, Jianhua Zhao, Aihua Wang, Richard Corkish, and Martin A. Green. Very efficient light emission from bulk crystalline silicon. *Appl. Phys. Lett.*, 82(18):2996, 2003.
- [25] Hieu T. Nguyen, Simeon C. Baker-Finch, and Daniel Macdonald. Temperature dependence of the radiative recombination coefficient in crystalline silicon from spectral photoluminescence. *Appl. Phys. Lett.*, 104(11):112105, mar 2014.
- [26] Armin Richter, Martin Hermle, and Stefan W. Glunz. Reassessment of the limiting efficiency for crystalline silicon solar cells. *IEEE Journal of Photovoltaics*, 3(4):1184–1191, oct 2013.
- [27] Armin Richter, Stefan W. Glunz, Florian Werner, Jan Schmidt, and Andres Cuevas. Improved quantitative description of auger recombination in crystalline silicon. *Phys. Rev. B*, 86(16), oct 2012.
- [28] Andreas Cuevas. The recombination parameter  $j_0$ . *Energy Procedia*, 2014.
- [29] *WCT-120 Photoconductance Lifetime Tester User Manual*.
- [30] Christopher Bege Henning Nagel and Armin G. Aberle. Generalized analysis of quasi-steady-state and quasi-transient measurements of carrier lifetimes in semiconductors. *Journal of Applied Physics*, 1999.
- [31] Andres Cuevas Ronald A. Sinton and Michael Stuckings. Quasi-steady-state photocon-

ductance, a new method for solar cell material and device characterization. *Proceedings of the 25th IEEE-PVSC*, 1996.

- [32] Mark J Kerr and Andres Cuevas. Very low bulk and surface recombination in oxidized silicon wafers. 2002.
- [33] Andres Cuevas Jan Schmidt, Mark Kerr. Surface passivation of silicon solar cells using plasma-enhanced chemical-vapour deposited silicon films and thin thermal SiO<sub>2</sub>/plasma silicon stacks. *Semiconductor Science and Technology*, 2001.
- [34] Carlos del Canizo Rosa Lago-Aurrerkoetxea, Ignacio Tobias and Antonio Luque. Lifetime measurements by photoconductance techniques in wafers immersed in a passivating liquid. *Journal of the Electrochemical Society*, 2001.
- [35] Malcolm Abbot Keith R. McIntosh. Recombination calculator. Online, November 2016. <https://www2.pvlighthouse.com.au/calculators/Recombination>
- [36] Martin A. Green. Limits on the short-circuit current and voltage and efficiency of silicon solar cells and imposed by intrinsic. IEEE, 1984.
- [37] Kane and Swanson. Measurement of the emitter saturation current by a contactless photoconductivity decay method. *IEEE Photovoltaic Specialists Conference*, 1985.
- [38] Mohamed Amara Romain Couderc and Mustapha Lemiti. Reassessment of the intrinsic carrier density temperature dependence in crystalline silicon. *Journal of Applied Physics*, 2014.
- [39] Valdes. Resistivity measurement on germanium for transistors. 1953.
- [40] Nanometrics. Conversation, 2013.
- [41] Nanometrics. *ECVPro: Electrochemical C-V Profiler User Manual*. P/N: 9PROF-UM01 Rev. B.
- [42] Dieter K. Schroder. *Semiconductor and Material Device Characterization*. John Wiley & Sons, 2006.
- [43] Solecon Laboratories. Technical information - solecon laboratories. Internet, 2016. available at: [www.solecon.com/sra.htm](http://www.solecon.com/sra.htm).
- [44] Takato. Surface passivation of silicon and substrates using quinhydrone-methanol treatment. In *3rd World Conference on Photovoltaic Energy Conversion May 11-18, ZOO3 Osaka, Japan, 2003*.
- [45] Bhumika Chhabra, Stuart Bowden, Robert L. Opila, and Christiana B. Honsberg. High effective minority carrier lifetime on silicon substrates using quinhydrone-methanol passivation. *Appl. Phys. Lett.*, 96(6):063502, 2010.
- [46] Costello. An investigation of electronic passivation of silicon (100) surfaces and in solutions and of p-benzoquinone. Master's thesis, University of Delaware, 2013.

- [47] Rotem Har-Lavan, Omer Yaffe, Pranav Joshi, Roy Kazaz, Hagai Cohen, and David Cahen. Ambient organic molecular passivation of si yields near-ideal, Schottky-mott limited, junctions. *AIP Advances*, 2(1):012164, 2012.
- [48] Meixi Chen, James H. Hack, Abhishek Iyer, and Robert L. Opila. Minority carrier lifetime measurements: An electrical passivation study. 2015.
- [49] Bhushan Sopori; Srinivas Devayajanam; Prakash Basnyat; Helio Moutinho; Bill Nemeth; Vincenzo Lasalvia; Steve Johnston; Jeff Binns; Jesse Appee;. Some challenges in making accurate and reproducible measurements of minority carrier lifetime in high-quality si wafers, 2014.
- [50] P. Hacke Q. Wang B. Sopori R. Margolis T.L. James Woodhouse M. Goodrich, A. A wafer-based monocrystalline silicon photovoltaics road map: Utilizing known technology improvement opportunities for further reductions in manufacturing costs. *Solar Energy Materials and Solar Cells*, 2013.
- [51] Inc. Virginia Semiconductor. Wet-chemical etching and cleaning of silicon. Technical report, Virginia Semiconductor, Inc., 2003.
- [52] Joon Sung Lee Hee Jin Lim Sewang Yoon Donghwan Kim Hayoung Park, Soonwoo Kwon. Improvement on surface texturing of single crystalline silicon for solar cells by saw-damage etching using an acidic solution. *Solar Energy Materials and Solar Cells*, 2009.
- [53] Nick Grant et. al. Light enhanced hydrofluoric acid and passivation for evaluating silicon bulk and lifetimes and conference paper. 2013.
- [54] Keith R. McIntosh Nicholas E. Grant and Jason T. Tan. Evaluation of the bulk lifetime of silicon wafers by immersion in hydrofluoric acid and illumination. *ECS Journal of Solid State Science and Technology*, 2012.
- [55] Kirt R. Williams. Etch rates for micromachining processing - part ii. *Journal of Microelectromechanical Systems*, 2003.
- [56] H. J. Queisser. Slip patterns on boron-doped silicon surfaces. *J. Appl. Phys.*, 32(9):1776, 1961.
- [57] Martin A. Green. The path to 25% silicon solar cell efficiency: History of silicon cell evolution. *Prog. Photovolt: Res. Appl.*, 17(3):183–189, may 2009.
- [58] J.E. Cotter, J.H. Guo, P.J. Cousins, M.D. Abbott, F.W. Chen, and K.C. Fisher. P-type versus n-type silicon wafers: Prospects for high-efficiency commercial silicon solar cells. *IEEE Trans. Electron Devices*, 53(8):1893–1901, aug 2006.
- [59] Private communication. Private Communication.
- [60] Ulrich Jger, Sebastian Mack, Achim Kimmerle, Andreas Wolf, and Ralf Preu. Influence of doping profile of highly doped regions for selective emitter solar cells. IEEE, 2010.
- [61] G. Pignatell and G. Queirolo. Aes study of boron diffusion in silicon from a boron nitride

source with hydrogen injection. 1979.

- [62] Peter Griffin James Plummer, Michael Deal. *Silicon VLSI Technology: Fundamentals, Practice and Modeling*. Prentice Hall, 2000.
- [63] B. Singha and C.S. Solanki. Study of boron precipitates formed during front side emitter formation with boron spin on dopant (BSOD) diffusion in n-type c-si solar cells. *Energy Procedia*, 57:117–125, 2014.
- [64] D. M. Brown and P. R. Kennicott. Glass source b diffusion in si and sio<sub>2</sub>. 1971.
- [65] Kyungsun Ryu, Ajay Upadhyaya, Hyun-Jin Song, Chel-Jong Choi, Ajeet Rohatgi, and Young-Woo Ok. Chemical etching of boron-rich layer and its impact on high efficiency n-type silicon solar cells. *Appl. Phys. Lett.*, 101(7):073902, aug 2012.
- [66] Bettina Wlpensinger Michael Andreas Kessler, Tobias Ohrdes and Nils-Peter Harder. Charge carrier lifetime degradation in cz silicon through the formation of a boron-rich layer during bbr<sub>3</sub> diffusion processes. *Semiconductor Science and Technology*, 2010.
- [67] Saint-Gobain. *PDS Products P-Type Planar Diffusion Sources: Low Temperature Oxidation and Silicon-Boron (Si-B) Layer*, April 2013.
- [68] K. McIntosh et. al. An examination of three common assumptions used to simulate recombination in and heavily doped and silicon. In *28th European Photovoltaic Solar Energy Conference and Exhibition*, 2013.
- [69] Keith R. McIntosh, , Pietro, and P. Altermate. A freeware 1 d emitter model for silicon solar cells. IEEE, 2010.
- [70] D. A. Clugston and P.A. Basore. Pc1d version 5: 32-bit solar cell modeling on personal computers. In *Proceedings of the 26th IEEE Photovoltaic Specialists Conference*, 1997.
- [71] Synopsis. Online. <http://www.synopsys.com/Tools/TCAD/DeviceSimulation/Pages/default.aspx>.
- [72] N. M. Johnson and M. D. Moyer. Absence of oxygen diffusion during hydrogen passivation of shallow-acceptor impurities in single-crystal silicon. *Appl. Phys. Lett.*, 46(8):787, 1985.
- [73] J. I. Pankove. Temperature dependence of boron neutralization in silicon by atomic hydrogen. *J. Appl. Phys.*, 68(12):6532, 1990.
- [74] G. B. Anderson N. H. Nickel and J. Walker. Hydrogen-induced platelets in disordered silicon. *Solid State Communications*, 1996.
- [75] N. M. Johnson N. H. Nickel, G. B. Anderson and J. Walker. Nucleation of hydrogen-induced platelets in silicon. *Physical Review B*, 2000.
- [76] R. W. Collins H. V. Nguyen, Ilsin An, M. Wakagi Yiwei Lu, and C. R. Wronski. Preparation of ultrathin microcrystalline silicon layers by atomic hydrogen etching of amorphous silicon and end-point detection by real time spectroellipsometry. *Applied Physics Letters*, 1994.



- [77] N. M. Johnson. Mechanism for hydrogen compensation of shallow-acceptor impurities in single-crystal silicon. *Physical Review B*, 1985.
- [78] D. Mathiot. Modeling of hydrogen diffusion in n- and p-type silicon. *Physical Review B*, 1989.
- [79] Vivek Sharma, Clarence Tracy, Dieter Schroder, Stanislau Herasimenka, William Dauksher, and Stuart Bowden. Manipulation of k center charge states in silicon nitride films to achieve excellent surface passivation for silicon solar cells. *Appl. Phys. Lett.*, 104(5):053503, feb 2014.